Activation of H_2 and CO_2. Insights into biological homo- and bimetallic-based catalysis applying vibrational spectroscopy

vorgelegt von
M. Sc. Biochemie und Molekulare Biologie
Stefan Malte Wahlefeld
geb. in Bremen

von der Fakultät II – Mathematik und Naturwissenschaften
der Technischen Universität Berlin
zur Erlangung des akademischen Grades

Doktor der Naturwissenschaften
– Dr. rer. nat. –

genehmigte Dissertation

Promotionsausschuss:

Vorsitzender:	Prof. Dr. Nediljko Budisa
Gutachter:	Prof. Dr. Peter Hildebrandt
Gutachterin:	Prof. Dr. Ulla Wollenberger

Tag der wissenschaftlichen Aussprache: 19.07.2018

Berlin 2018

Contents

List of Figures

List of Tables

1. Abstract

The activation of small molecules, such as hydrogen or carbon dioxide, is an important part in a renewable, green chemistry in the future in our society. In this context, nature already shaped metalloenzymes, which are capable of catalyzing a wide variety of reactions. In order to exploit their biotechnological potential and provide an optimum performance, a fundamental understanding of their catalytic mechanisms is inevitable. This thesis presents an interdisciplinary approach providing detailed insights into the biochemical and spectroscopic properties of a soluble hydrogenase (SH) from *Hydrogenophilus thermoluteolus* TH-1^T (*Ht*). Additionally, a formate dehydrogenase (FDH) from *Rhodobacter capsulatus* (*Rc*) was investigated by means of vibrational spectroscopy.

The first part of this thesis discusses kinetic and activity assays of the *Ht*SH. Complementary, infrared (IR) absorption spectroscopy in combination with electron paramagnetic resonance (EPR) spectroscopy was carried out on the same enzyme samples in order to gain precise information about redox species of the catalytic center before and after activation as well as enzymatic integrity. The *Ht*SH exhibits catalytic H_2-mediated Nicotinamide adenine dinucleotide (NAD^+) reduction in the presence of O_2 at elevated temperatures displaying an optimum at 50 °C. The IR spectroscopic characterization reveals a rich set of different oxidized and reduced intermediates. Notably, in the oxidized state an unprecedented upshifted CO stretching mode is observed at 1993 cm^{-1}. Within the reduced species, the Ni_a-C signal in the EPR spectrum of H_2-treated sample was mainly found at temperatures below 10 K, which could presumably be a result of fast spin-lattice relaxation related to magnetic coupling with another cofactor that is paramagnetic under these reducing conditions. In conclusion, this might serve as an explanation why Ni_a-C and other paramagnetic active site species often are not detected.

Furthermore, to explain the molecular details of the O_2-tolerance origin in soluble [NiFe]-hydrogenases, a bioinspired heterobimetallic S-oxygenated [NiFe] complex was synthesized. This complex was fully analyzed by vibrational spectroscopy in comparison to the oxygen-free reference species. Using further experimental and computational techniques, the electronic structures were elucidated with emphasis on the bridging sulfenato moiety. Based on the obtained results, novel strategies of exploring S-oxygenated intermediates in hydrogenases are proposed.

The last part of this thesis is dedicated to the investigation of a FDH. Here, resonance Raman (RR) spectroscopy in combination with computational methods were applied. The research focuses primarily on the first coordination sphere of the Molybdenum ion of the active site in the oxidized and reduced state. Spectra of different structural models were calculated and compared with the experimental data. Based on this multidisci-

plinary approach, a mixture of reduced intermediate states were assigned and compared to the existing proposed catalytic cycles. Additionally, the binding mode of the inhibitor molecule azide was investigated by IR spectroscopy. The direct binding mechanism to the Molybdenum ion proposed so far cannot be verified by the obtained data. The presented results demonstrate that a binding in the proximity of the active site is rather likely.

2. Zusammenfassung

Die Aktivierung von kleinen Molekülen, wie beispielsweise Wasserstoff oder Kohlenstoffdioxid, ist ein entscheidener Faktor im Rahmen in einer zukünftigen, erneuerbaren und grünen Chemie. Die Natur hat dafür Metalloenzyme entwickelt, die in der Lage sind, eine große Anzahl verschiedener Reaktionen zu katalysieren. Um deren biotechnologischen Potentiale möglichst vollständig auszunutzen und eine optimale Leistungsfähigkeit zu entwickeln, ist ein fundamentales Verständnis der zugrundeliegenden katalytischen Mechanismen unumgänglich. Diese Doktorarbeit präsentiert einen interdisziplinären Ansatz, um umfassende Einblicke in die biochemischen und spektroskopischen Eigenschaften einer löslichen Hydrogenase (SH) aus *Hydrogenophilus thermoluteolus* TH-1^T(*Ht*) und einer Formiat Dehydrogenase (FDH) aus *Rhodobacter capsulatus* (*Rc*) zu gewinnen.

Im ersten Teil der vorliegenden Arbeit werden kinetische sowie Aktivitätsversuche zur *Ht*SH diskutiert. Zusätzlich, werden mittels Infrarot- (IR) sowie Elektronenspinresonanzspektroskopie (EPR) weitere wichtige Informationen zu unterschiedlichen Spezien des aktiven Zentrums und zur enzymatischen Integrität generiert. Die *Ht*SH zeigt katalytische, wasserstoffabhänige Nicotinamidadenindinukleotid- (NAD^+) Reduktion. Dies geschieht in der Gegenwart von O_2 bei erhöhten Temperaturen mit einem Optimum von 50 °C. Mittels IR Spektroskopie kann eine Reihe von oxidierten und reduzierten Intermediaten charakterisiert werden. Hierbei ist bemerkenswert, dass im oxidierten Zustand eine bisher noch nicht entdeckte, hochverschobene CO Streckschwingung beobachtet wird. In den reduzierten Zuständen wird im EPR Spektrum das Ni_a-C Signal, der mit Wasserstoff behandelten Probe, nur bei Temperaturen unterhalb von 10 K detektiert. Dies könnte das Resultat einer schnellen Spin-Gitter-Relaxierung mit einem benachbarten Kofaktor sein, der unter diesen Bedingungen ebenfalls reduziert vorliegt. Das wäre eine mögliche Erklärung, warum Ni_a-C und andere paramagnetische Zustände des aktiven Zentrums häufig nicht beobachtet werden.

Um das Verständnis der molekularen Details zur Sauerstofftoleranz von löslichen Hydrogenasen voranzutreiben, wurde ein bioinspirierter S-oxygenierter [NiFe] Komplex vollständig mittels Schwingungsspektroskopie charakterisiert. Durch die Anwendung von weiteren experimentellen und theoretischen Techniken konnten die elektronischen Strukturen des Komplexes und seiner sauerstofffreien Referenzstruktur aufgeklärt werden. Hierbei lag ein besonderer Schwerpunkt auf der verbrückenden Sulfenatoeinheit. Anhand der vorliegenden Ergebnisse können neuartige Strategien vorgeschlagen werden, um S-oxygenierte Intermediate in Hydrogenasen zu untersuchen.

Der letzte Teil der Arbeit beschäftigt sich mit der Untersuchung einer FDH. Hierbei wurde Resonanz-Raman-Spektroskopie (RR) in Kombination mit computergestütz-

ten Modellrechungen verwendet. Die Untersuchung fokusierte sich vor allem auf die erste Koordinationsspähre des Molybdenumions des aktiven Zentrums im oxidierten und reduzierten Zustand. Unterschiedliche, berechnete Spektren wurden mit den experimentellen Daten verglichen. Auf diesem Ansatz basierend konnten verschiedene reduzierte Intermediate zugeordnet und mit den bisher bestehenden katalytischen Zyklen verglichen werden. Zusätzlich wurde noch die Bindung des Inhibitors Azid mittels IR Spektroskopie überprüft. Die so gewonnenen Daten demonstrieren, dass ein direkter Bindungsmechanismus an das Molybdänion, wie es kürzlich vorgeschlagen wurde, eher unwahrscheinlich gegenüber einer möglichen Bindung in der Nähe des aktiven Zentrums ist.

3. Motivation and Concepts

With respect to the fast growing human population and rising consumption of goods, the higher energy demands result in an increasing environmental pollution and affect in particularly the global climate. Such climate changes require novel technologies to reduce the dependency on fossil fuels as dominating primary energy source and as basic component for chemical building blocks in synthetic industry. The vast CO_2 output by mankind further enhances the greenhouse effect. Consequentially, the transition to clean and renewable energy and the replacement of ethene from crude oil in large chemical processes are fundamental aims in sustainable, green chemistry. Dihydrogen (H_2) and carbon dioxide (CO_2) are promising candidates as substitutions. So far, the use of these molecules is hampered by the expensive rare earth metals used for the catalytic transformation. Over millions of years, nature has evolved sophisticated biomacromolecules which catalyze specific and complex chemical reactions. Some of such enzymes contain even one or more metals. These, so-called metalloenzymes, are involved in essential cellular functions including energy conversion, biosynthesis and the transfer of redox equivalents through the cell. Unlike most synthetic chemical processes, enzymes are capable of catalyzing reactions in a highly selective manner under ambient conditions.

The "Knallgas"reaction of molecular hydrogen and oxygen releases large amounts of energy. So far, precious metals, such as Platinum, have been widely applied as fuel cell catalysts. In biology, this task is carried out by so-called hydrogenase enzymes, which efficiently catalyze the reversible cleavage of H_2 into protons and electrons by utilizing earth-abundant transition metals, such as Ni and Fe.[144] As the demand for sustainable energy conversion is still increasing, hydrogenases became a focus of major research interests. These enzymes may accelerate the exploitation of H_2 as an energy carrier, also by serving as blueprints for the design of bio-inspired molecular catalysts. For this reason, this thesis focuses on exploring biophysical properties of such [NiFe]-hydrogenases.

In practical terms, an application of [NiFe]-hydrogenases often suffer from the sensitivity towards molecular oxygen and its reactive species, as they quickly inactivate the active metal center. Thus, the research on biological fuel cells concentrates on oxygen-tolerant enzymes from various organisms. Such enzymes are capable to convert H_2 even under ambient concentrations of oxygen, which make them promising candidates for biological large scale processes. In this thesis, the thermostable soluble [NiFe]-hydrogenase from *H. thermoluteolus* TH-1^T was investigated. With respect to its intrinsic temperature stability this enzyme appears suitable for biotechnological applications. However, even the reversible inactivation of such biocatalysts by oxygen is still investigated and recently a mechanism via mixed thiolato and sulfenato bridges was proposed.[104] Therefore,

a synthetic inorganic complex was designed and subsequent explored by various computational and experimental techniques in order to identify the underlying physicochemical parameters of the involved chemical groups.

The second part of this thesis is dedicated to the activation of CO_2. The conversion of carbon dioxide to a variety of value-added chemicals, such as carbon monoxide, formic acid or methanol using homogeneous/heterogeneous catalysts is a potential concept to overcome the dependency of fossil fuels in the future.[198] In recent years, (bio)-electrochemical catalysis attracted great attention. The advantages are that the reaction is controllable through defined electrode potentials and other reaction parameters. Furthermore, through the utilization of renewable energy sources, such as solar or wind, no further CO_2 is produced. Electrochemical reaction systems can be implemented in a compact and modular manner, so they are available on-demand and simple to scale-up. However, the challenge remains to find a catalyst which provides high turn-over rates at low costs and additionally would be suitable for commercial application. Designing new catalysts by a biomimetic approach or by using complete enzymes is particularly appealing. Regarding CO_2 reduction, the reaction requests the catalysts to be able to mediate multi-electron/multi-proton reaction steps. One way to achieve this is to reduce a metal center, which requires a ligand field capable of stabilizing different oxidation states. Another way could be the reduction of the ligands itself, where the metal acts as an mediator for electron shuttling.

In nature, the global carbon cycle relies upon the transformation of C_1 compounds including the reduction of CO_2 into organic molecules, such as formate. The oxidation of the latter is widely used by organisms, e. g. for the generation of reducing equivalents, as growth substrate or as product in fermentation cycles. The splitting of formate is catalyzed by formate dehydrogenases. These enzymes harbor a Molybdenum or Tungsten active site. So far, the properties of these large cofactors remained largely elusive. It is known, that the redox states of the metal changes upon formate splitting. However, much less knowledge was accumulated about the influence of the specific ligation sphere. Thus, the elucidation of the mechanistic details of this reaction may provide valuable insights required for the design of novel catalysts. In this thesis, RR spectroscopy was applied to study the inherent vibrational modes of the Mo-containing active site of a FDH from *Rc.* In combination with computational studies, individual redox intermediates could be assigned and differences in the ligation of the Molybdenum ion verified.

4. Theoretical Background

4.1. Vibrational spectroscopy

A fundamental chemical challenge is the determination of molecular structures. Analytical chemistry offers a wide range of techniques, such as mass spectrometry (MS), electron paramagnetic resonance spectroscopy, x-ray absorption spectroscopy (XAS) and vibrational spectroscopy.[7,14,95,253] Especially, the latter allows a non-invasive and non-destructible monitoring of samples even at room temperature. The two major relevant techniques of vibrational spectroscopy are infrared and Raman spectroscopy. In both techniques, the interaction of electromagnetic radiation with molecules is probed resulting in transitions between different states of vibrational modes. Raman spectroscopy relies on an inelastic scattering process of the incident photons, whereas in IR spectroscopy photons are absorbed.

In the latter case the sample is irradiated with polychromatic light. The incident electromagnetic radiation includes an energy $h\upsilon_k$ which equals an energy difference between an initial (i) and a final (f) vibrational state of the respective mode k, as stated in equation 4.1.

$$h\upsilon_k = h\upsilon_k^f - h\upsilon_k^i \tag{4.1}$$

In Raman spectroscopy the inelastic scattering of photons with a discrete energy $h\upsilon_k$ is detected. Regarding the law of energy conservation, the difference in energy between the incident electromagnetic radiation and the inelastically scattered photons $h\upsilon_k^{scat}$ matches the energy difference of the initial and final vibrational states of the normal mode k.

$$h\upsilon_k - h\upsilon_k^{scat} = h\upsilon_k^f - h\upsilon_k^i \tag{4.2}$$

4.1.1. Raman spectroscopy

The Raman effect is a process of inelastic light scattering in which two photons are involved. Here, the energy of the scattered light depends on the incident electromagnetic radiation. This physical principle was predicted theoretically in 1923 by A. Smekal and later proven independently by C.V. Raman as well as by Landsberg and Mandelstam.[128,201,239] A profound description of the Raman effect can be found in the book by D.A. Long.[142]

A classical view towards the Raman scattering is based on first order induced electric

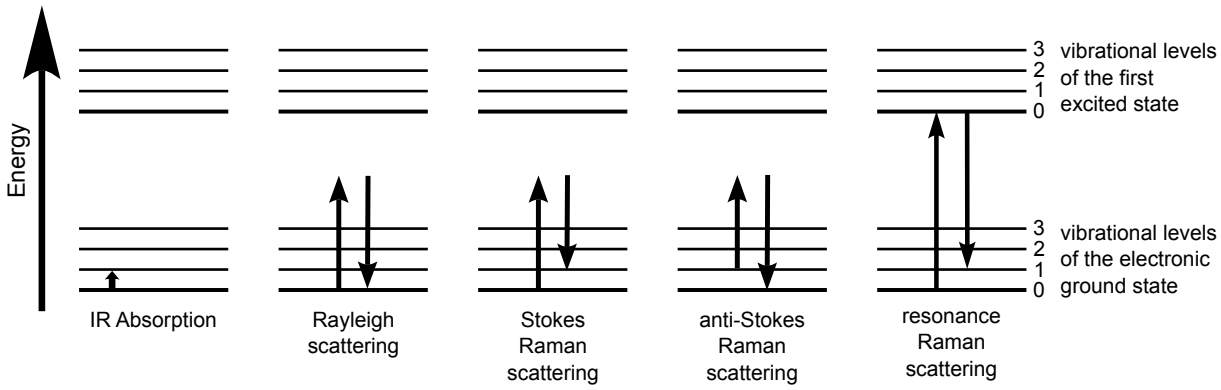

Figure 4.1. Energy diagram of vibrational absorption and scattering processes. Figure adapted for this current work with kind permission from Dr. M. Sezer.

dipoles. In this process the oscillating electric field vector E of the incoming light interacts with the electron cloud of the scattering core. As a result, the direction and magnitude of the induced dipole moment vectors p depend on the polarizability of the molecule which is displayed in 4.3

$$p = \alpha \cdot E \tag{4.3}$$

In this equation α describes the 3x3 polarizability tensor which involves the position of the nuclei with respect to the electron cloud. Therefore, it is sensitive to alterations of the moleculeâs internal coordinates. Every molecule with N atoms exhibit 3N-5 normal modes for linear and 3N-6 for non-linear, respectively. The normal mode Q_k describes the oscillations of each atom with the frequency ω_k and its time dependence is given by

$$Q_k(t) = Q_{k_0} cos(\omega_k t + \delta_k) \tag{4.4}$$

Q_{k_0} and δ_k represent the amplitude and the phase factor of the vibration. In order to determine changes in the tensor α coupled to the molecular vibration along Q_k a Taylor series is expanded

$$\alpha_{\rho\sigma} = (\alpha_{\rho\sigma})_0 + \sum_k \left(\frac{\delta \alpha_{\rho\sigma}}{\delta Q_k} \right)_0 Q_k + ... \tag{4.5}$$

ρ and σ denote the molecules fixed internal coordinates which replace the Cartesian variables x, y and z. Combining equation 4.4 and 4.5 a correlation for the time dependence of α is given

$$\alpha_k = \alpha_0 + \left(\frac{\delta \alpha_{\rho\sigma}}{\delta Q_k} \right)_0 Q_{k_0} cos(\omega_k t + \delta_k) \tag{4.6}$$

For an electromagnetic wave described by $E = E_0 cos(\omega_k t)$, in which the phase δ_k is neglected, the term for the induced dipole moment vector is changed to,

$$\begin{aligned} p_{ind} &= \alpha_0 E_0 cos(\omega t) + \sum_k \left(\frac{\delta\alpha_{\rho,\sigma}}{\delta Q_k}\right)_0 Q_{k_0} cos(\omega_k t) \cdot E_0 cos(\omega t) \\ &= \underbrace{\alpha_0 E_0 cos(\omega t)}_{Rayleigh\ Scattering} + \frac{1}{2}\sum_k \left(\frac{\delta\alpha_{\rho,\sigma}}{\delta Q_k}\right)_0 Q_{k_0} E_0 \left(\underbrace{cos(\omega - \omega_k)t}_{Stokes} + \underbrace{cos(\omega + \omega_k)t}_{Anti-Stokes} \right) \end{aligned} \tag{4.7}$$

The first term in equation 4.7 corresponds to the dominant Rayleigh scattering. Here, the energy of the elastic scattered photons equals the energy of the incident ones. Only the last two terms refer to Raman scattering and, hence, can be monitored by this spectroscopic technique (see Figure 4.1). The frequency of the scattered radiation shifts by ω_k. Accordingly, the polarizability tensor α has to change with the k^{th} vibration of the molecule, rendering the term $\left(\frac{\delta\alpha}{\delta Q_k}\right)_0$ non-zero. In principle, classical physics can determine the frequencies of scattered radiation. However, it fails in explaining the observed intensities as well as no information about the molecule's properties can be obtained. Thus, a quantum mechanical treatment of the Raman effect is necessary.

The quantum mechanical description was developed from 2^{nd} order perturbation theory by Placzek on the basis of Kramers and Heisenberg dispersion theory.[56,120,194] Here, quantum mechanics are used to define molecular properties, whereas classical physics describe the electromagnetic radiation. Consequently, the Raman scattering derives from a transition of the molecule from a vibrational quantum state $|i\rangle$ to another vibrational quantum state $|f\rangle$ with the respective energies of E_i and E_f. This transition passes through a virtual state $|r\rangle$ (see Fig. 4.1). Raman band intensities which derive from such a transition are calculated with following equation.

$$I_{fi} \approx I_1 exp\Big(- \frac{E_i}{k_b T}\Big)\big(\omega_1 \pm \omega_{fi}\big)^4 \sum_{\rho\sigma} |\alpha_{\rho\sigma}|^2_{fi} \tag{4.8}$$

The incident radiation is described by its intensity (I_1) and its frequency (ω_1). ω_{fi} illustrates the frequency of the energy difference between $|f\rangle$ and $|i\rangle$. Depending on the temperature all possible scattering centers of $|i\rangle$ are described by the Boltzmann distribution in the exponential term. Finally, the transition polarizability tensor $\alpha_{\rho\sigma_{fi}}$ represents the $\rho\sigma$ element. This tensor derives from the solution of $p_{fi} = \langle \Psi_f^1 | \hat{p} | \Psi_i^0 \rangle + \langle \Psi_i^1 | \hat{p} | \Psi_f^0 \rangle$. Compared to the classical case in eq. 4.3 the oscillating electric dipole as well as the polarizability are replaced by the quantum mechanical formula which also includes the transition dipole moment. According to Placzek, elements of the transition polarizability can generally be described as

$$\alpha_{\rho\sigma_{if}} = \frac{1}{\hbar} \sum_{r \neq i,f} \left(\frac{\langle f|\hat{p}_\rho|r\rangle\langle r|\hat{p}_\sigma|i\rangle}{\omega_{ri} - \omega_1 - i\Gamma_r} + \frac{\langle f|\hat{p}_\sigma|r\rangle\langle r|\hat{p}_\rho|i\rangle}{\omega_{rf} + \omega_1 + i\Gamma_r} \right) \tag{4.9}$$

Here, $\hat{p}_{\rho\sigma}$ characterizes the dipole operator in the corresponding ρ and σ direction. The decisive energy for a transition between $|r\rangle$ and $|i\rangle$ as well as $|r\rangle$ and $|f\rangle$ are denoted by the terms $\hbar\omega_{ri}$ and $\hbar\omega_{rf}$, respectively. The energy of the incident radiation is defined by ω_1. The last expression in the denominator ($i\Gamma_r$) depicts the life time of the state $|r\rangle$. Summation is carried out over all intermediate states of $|r\rangle$. The respective energy E_r is not bound by any restrictions and in principle, can be lower as E_i or above E_f. As a consequence, Raman scattering can be viewed as a transition from $|r\rangle \leftarrow |i\rangle$ (absorption of light) and $|f\rangle \leftarrow |r\rangle$ (emission of light) weighted by the sum over all virtual states of $|r\rangle$. However, no information about $|r\rangle$ can be gained since it is not a solution of the time-dependent Schrödinger equation. In Raman scattering the transition dipole moment between $|r\rangle$ and both $|i\rangle$ as well as $|f\rangle$ is non-zero. Therefore, the initial and final vibrational level are characterized by the properties of the electronic ground state.

4.1.2. Resonance Raman spectroscopy

If the frequency of the incident radiation (ω_1) is close to an electronic transition of the molecule (with $\hbar\omega_{ri}$), the resonance Raman effect occurs. In this case, the denominator $\omega_{ri} - \omega_1 - i\Gamma_r$ dominates the sum of eq. 4.9. This term is the so-called resonant term and correspondingly, eq. 4.9 is simplified to

$$\alpha_{\rho\sigma_{fi}} = \frac{1}{\hbar} \sum_{r=f} \left(\frac{\langle f|\hat{p}_\rho|r\rangle \langle r|\hat{p}_\sigma|i\rangle}{\omega_{ri} - \omega_1 - i\Gamma_r} \right). \tag{4.10}$$

Regarding the Born-Oppenheimer approximation the nuclear and electronic wave functions can be separated. This leads to $|i\rangle = |\upsilon_i\rangle|g\rangle$, $|f\rangle = |\upsilon_f\rangle|g\rangle$ and $|r\rangle = |n\rangle|e\rangle$ in which $|g\rangle$ and $|e\rangle$ describe the electronic ground and first excited state. The initial, final and virtual vibrational states are characterized by $|\upsilon_i\rangle$, $|\upsilon_f\rangle$ and $|n\rangle$, respectively. As a consequence, each integral can be split into two terms and the transition polarizability further reduces to

$$\alpha_{\rho\sigma_{fi}} = \frac{1}{\hbar} \sum_{r=f} \left(\frac{\langle \upsilon_i n\rangle p_{ge,\rho} \langle n\upsilon_f\rangle p_{ge,\sigma}}{\omega_{ri} - \omega_1 - i\Gamma_e} \right) \tag{4.11}$$

Accordingly, $p_{ge,\rho}$ and $p_{ge,\sigma}$ describe the electronic transition moments in the corresponding ρ and σ direction. Additionally, the $p_{\rho,\sigma}$ term depends upon the nuclear vibrations Q_k. Therefore, a Taylor series is generated accounting for the transition dipole moment around the displacement from the equilibrium position Q_0, which are displayed as follows.

$$
\begin{aligned}
p_{ge,\rho}(Q_k) = \; & p^0_{ge,\rho}(Q^0_k) + \sum \left(\frac{\delta p_{ge,\rho}}{\delta Q_k} \right)_k Q_k + ... \\
p_{ge,\sigma}(Q_k) = \; & p^0_{ge,\sigma}(Q^0_k) + \sum \left(\frac{\delta p_{ge,\sigma}}{\delta Q_k} \right)_k Q_k + ...
\end{aligned}
\tag{4.12}
$$

Here, $p^0_{ge,\rho(\sigma)}(Q^0_k)$ denote the transition dipole moment at nuclei equilibrium positions. A combination of 4.11 and 4.12 reveals that the transition polarizability can be separated in individual terms with different physical meanings

$$
\alpha_{\rho\sigma_{fi}} = A_{\rho\sigma} + B_{\rho\sigma} + ... \tag{4.13}
$$

with

$$
\begin{aligned}
A_{\rho\sigma} &= \frac{1}{\hbar} \; p^0_{ge,\rho} p^0_{ge,\sigma} \sum \frac{\Big\langle \upsilon_i n \Big\rangle \Big\langle n \upsilon_f \Big\rangle}{\omega_{ri} - \omega_1 - i\Gamma_{er}} \\
B_{\rho\sigma} &= \frac{1}{\hbar} \left(p^*_{ge,\rho} p_{ge,\sigma} \sum \frac{\Big\langle \upsilon_i | Q_k | n \Big\rangle \Big\langle n \upsilon_f \Big\rangle}{\omega_{ri} - \omega_1 - i\Gamma_{e\ r}} \right) \\
&\quad ... + p^*_{ge,\rho} p_{ge,\sigma} \sum \frac{\Big\langle \upsilon_i n \Big\rangle \Big\langle n | Q_k | \upsilon_f \Big\rangle}{\omega_{ri} - \omega_1 - i\Gamma_{e\ r}}
\end{aligned}
\tag{4.14}
$$

Classically, the A and B term exhibit the highest importance. Enhancement via the A term relies upon two Franck-Condon integrals $\left(\Big\langle \upsilon_i n \Big\rangle \Big\langle n \upsilon_f \Big\rangle \right)$ and is also refereed to as the Franck-Condon term. This mechanism is most prominent with decreasing orthogonality character of the wave functions in the ground and the excited state. Resonance enhancement is usually restricted to total symmetric vibrational modes which are coupled to strong electronic transitions such as $\sigma - \sigma^*$ or $\pi - \pi^*$.

The 'Herzberg-Teller' B term enhancement arises from vibronic coupling which is not limited to totally symmetric modes. It is expressed by $p^*_{\sigma,\rho}$ for small displacements of Q_k. This can be visualized by the vibronic coupling between the electronic ground and excited state though this normal coordinate. The corresponding transition dipole moment of a transition from $|g\rangle$ to $|e\rangle$ might "borrow"contributions from $|g\rangle$ to another nearby excited state $|h\rangle$. The coupling integral and the displacement Q_k are proportional to the amount of "borrowed"transition dipole moment. Additionally, the smaller the energy difference between the excited states is, the stronger the coupling becomes. The B term enhancement can involve total symmetric as well as non-total symmetric resonance Raman modes.

4.1.3. Infrared absorption spectroscopy

In Infrared spectroscopy the incident radiation $h\upsilon^{IR}$ is absorbed by the molecule resulting in a transition of $|\upsilon_k^i\rangle$ to $|\upsilon_k^f\rangle$ for all infrared active modes k. The observed intensities for IR spectroscopy are determined by the transition probability W_{if}

$$I^{IR} \sim W_{if} \sim \left|\langle \Psi_f|\hat{\Omega}|\Psi_i\rangle\right|^2 \tag{4.15}$$

The operator $\hat{\Omega}$ is different in IR and Raman spectroscopy as outlined in eq. 4.8. In IR spectroscopy, the perturbation of the system is determined by the electronic dipole moment operator $\hat{\Omega} = \hat{P}^e$ which is formulated as:

$$P^e = \sum_j e_j \cdot q_j \tag{4.16}$$

The effective charge of the molecule is denoted by e_j of the j^{th} atom. The distance of the nuclei to their corresponding center of gravity is illustrated by the internal coordinate q_j which is expressed in Cartesian coordinates (x_j, y_j, z_j). The mass-weighted internal coordinates for each vibrational mode k are converted into the normal coordinate Q_k. Finally, a Taylor series expands the electronic dipole moment along Q_k.

$$\tilde{P}^e \approx P_0^e + \sum_k \left(\frac{\delta P^e}{\delta Q_k}\right)_0 + Q_k + ... \tag{4.17}$$

Combining this equation with 4.15 yields

$$I^{IR} \sim \left|\langle \Psi_f|\tilde{P}^e|\Psi_i\rangle\right|^2 \approx \left|P_0^e\langle \Psi_f|\Psi_i\rangle \sum_k \left(\frac{\delta P^e}{\delta Q_k}\right)_0 \langle \Psi_f|\hat{Q}_k|\Psi_i\rangle\right|^2 \tag{4.18}$$

As a result, the infrared intensity depends only on the last expression of the equation because in the first term the wave functions Ψ_f and Ψ_i are by definition orthogonal and therefore always zero. Interaction between the incident radiation and the molecule leads to an active infrared mode k if the latter changes the electronic dipole moment P^e of the molecule. Based on the harmonic approximation the integral $\langle \Psi_f|\hat{Q}_k|\Psi_i\rangle$ is non-zero when the quantum numbers i and f vary by ± 1. In addition, symmetry-based selection rules are also described by the this term. Therefore, eq. 4.18 can be rewritten.

$$I_k^{IR} \sim \left|\left(\frac{\delta P^e}{\delta Q_k}\right)_0 \langle \Psi_f|\hat{Q}_k|\Psi_i\rangle\right|^2 \tag{4.19}$$

This quantity determines the portion of the absorbed incident light A in Lambert-Beerâs law:

$$A = -log\frac{I}{I_0} = \varepsilon \cdot c \cdot d \tag{4.20}$$

Here, the absorbance A is described by the intensity of the transmitted light (I) and the intensity of the light source (I_0) in the logarithmic term. Furthermore, the concentration c, the extinction coefficient ε as well as the path length d can additionally be used to derive the absorption of the sample.

4.2. Electron Paramagnetic Resonance Spectroscopy

EPR spectroscopy was performed either by Christian Lorent in case of the thermophilic [NiFe]-hydrogenase or by Benjamin Duffus for all Formate Dehydrogenase-related experiments. Measurements were supported by Christian Teutloff from the Freien Universität Berlin. In the following a brief review of the physical details will be given.[7,108]

Besides mass and charge, electrons exhibit another important physical parameter which determines their behavior. The intrinsic angular momentum, also spin, is a vector coupled to the magnetic dipole moment $\vec{\mu}$.

$$\vec{\mu} = -g\mu_B\vec{S} \tag{4.21}$$

Here, g is a dimensionless constant displaying a value of $g_e = 2,0023$ for the free electron. The so-called Bohr magneton μ_B includes the natural constants as quotient from the elementary charge e, the reduced Plank quantum of action $\hbar$ and the mass of the electrons m_e.

$$\mu_B = \frac{e\hbar}{2m_e} \tag{4.22}$$

Given that the electron is exposed to an external homogeneous magnetic field B_0 the spin orients itself parallel ($S = \frac{1}{2}$) or anti-parallel ($S = -\frac{1}{2}$) in the magnetic field. According to the Zeeman effect the electrons split into two separate discrete energy levels. Using electromagnetic radiation, transitions between the energy levels can be induced if the following equation is fulfilled.

$$\Delta E = h\upsilon = g\mu_B B_0 \tag{4.23}$$

For magnetic fields of 3300 Gauß a transition frequency of 9,3 GHz is gained which matches the frequency of micro waves. One reason for the higher sensitivity of EPR compared to Nuclear magnetic resonance (NMR) spectroscopy is the lower mass of the electron. As a result, the Bohr magneton is three orders of magnitude higher than the corresponding nuclear magneton μ_n

4.3. [NiFe]-hydrogenase

4.3.1. Hydrogen as an alternative energy carrier

The massive anthropogenic release of CO_2 and its concerning role in global warming has prompted the search for renewable and clean energy sources. Solar and wind energy are promising alternatives, however, storing the generated electricity is a great challenge in the 21^{st} century. The production of dihydrogen may be an effective way to circumvent this problem in the future. Its reaction with oxygen releases high amounts of energy.[186] One way to produce dihydrogen is the splitting of water. Currently, platinum has displayed the highest activity among inorganic catalysts, however, it is one of the most expensive metals with limited occurrence.[43] Finding or designing new production ways by using nature as a blueprint is particularly appealing. Hydrogenases are catalyzing the splitting as well as the generation of dihydrogen. In principal, these enzymes can be used in several approaches which are connected to their enzymatic function. For instance, hydrogen-based energy conversion remains their most important biotechnological application.[32] Biological hydrogen production can be realized by dark fermentation of cheap organic substrates or waste.[16] As an alternative, artificial *in vivo* or *in vitro* systems containing hydrogenases coupled to to photosensitizern or to the biological photosynthetic machinery could be applied.[121,122,145,230] Conceptually, these strategies excel current state of the art industrial processes which involve natural gas combustion over rare-earth metal catalysis.[252] Furthermore, bidirectional hydrogenases are able to regenerate cofactors, such as nicotine amide adenine dinucleotide (phosphate) (NAD(P)). No organic substrates are necessary and only protons are generated as side product making hydrogenases, compared to other enzymatic systems, a useful tool in biotechnology and the pharmaceutical industry.[130,202,206]

4.3.2. Enzymatic Structure and Function

Hydrogenases are metalloenzymes which can be categorized by the composition of their active sites into three seperate phylogenetic classes: the [Fe]-, the [FeFe]- and the [NiFe]-hydrogenases.[171,184,233,260] Their catalytic metal centers share a common low-spin Fe^{2+} coordinated by at least one thiolato group and two diatomic ligands. In this thesis only the [NiFe]-containing class was investigated and is further refereed to. These enzymes consists of at least two subunits which harbor either the [NiFe] site or three FeS clusters. Albeit, the subunit and cofactor composition can vary substantially between different [NiFe]-hydrogenases. Basic catalytic activity can already be achieved by only one additional FeS cluster and the active site.[131] Enzymes isolated from the anaerobic, sulfate-reducing bacteria of the group *Desulfovibrio* are well studied and in the following structural and catalytic relevant features will be discussed on the basis of these so-called "standard"[NiFe]-hydrogenases. This class are globular proteins which consists of a large ($\approx$ 60 kDa) and a small ($\approx$ 30 kDa) subunit. The latter harbors the FeS clusters, whereas

the bimetallic center is connected to the protein shell via two bridging and two terminal cysteine amino acids in the large subunit (see Fig. 4.2). Furthermore, the iron is bound by three unusual inorganic and isoelectronic ligands, one carbon monoxide and two cyanides. This unprecedented biological coordination keeps the Fe in its low spin (S = 0) ferrous form while the Ni is formal redox active.[86,186,210,261]

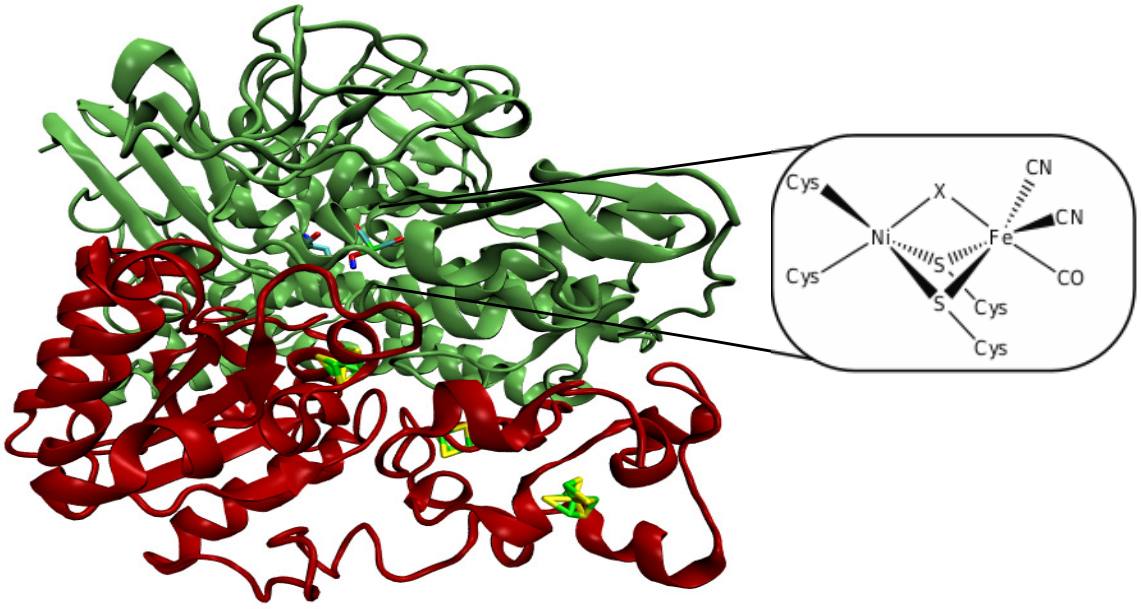

Figure 4.2. Crystallographic representation of the "standard"[NiFe]-hydrogenase from *Desulfovibrio vulgaris* Miyazaki F (pdb code: 1WUJ). The large and small subunit are colored in green and red, respectively. FeS clusters are shown in yellow and light green and the [NiFe] active site is enlarged schematically, the X represents variable ligands in the bridging position.

Finally, a third variable bridging ligand is observed in most redox intermediates (see Fig. 4.2).[144] With respect to the individual redox states, electron density is reorganized at the active site. These alterations lead to differences of the normal mode stretching frequencies of the inorganic Fe-bound ligands which exhibit intrinsic σ-donor and π-acceptor characteristics. These inorganic ligands are considerably sensitive probes and in combination with IR spectroscopy a powerful tool to monitor structural and electronic changes at the catalytic center.[50,53,62,100] Since the [NiFe] active site is deeply buried within the protein matrix, three enzymatic pathways are required, one for hydrogen gas supply and the other two for electron and proton transfer. During H_2 oxidation, dihydrogen access is suggested to occur via hydrophobic gas channels.[110,160,266] The released electrons are

shuttled via [FeS] clusters towards different cellular electron carrier, such as cytochromes or $NAD(P)^+$.[32,135] Additionally, proton transfer pathways have been proposed but are still under debate.[1,176,245]

The [NiFe]-hydrogenases are subdivided in five classes. Historically, conserved amino acid sequence patterns were the basis for this classification. Nevertheless, enzymes of the individual groups share common motifs regarding their structure, physiological function and location inside the cell.[258,259] Group 1 hydrogenases represent membrane-bound periplasmic proteins which couple hydrogen oxidation to the respiratory chain. The emerging protonmotive force is used to generate adenosine triphosphate (ATP). The 2^{nd} group includes both cyanobacterial uptake and hydrogen sensing [NiFe]-hydrogenases which may be engaged in energy conversion or regulation of hydrogen metabolism on the cellular level. Bidirectional heteromultimeric cytoplasmic [NiFe]-hydrogenases form group 3. These enzymes couple the reversible cleavage of H_2 to the reduction of an additional cofactor substrate, such as $NAD(P)^+$. Their catalytic bias operates reversibly and their physiological function relies upon the cellular metabolic conditions.[6,31] High sequence homologies are observed between bidirectional [NiFe]-hydrogenases and Complex 1 as well as other NADH oxidorecdutases.[2,3,182,187,218,219] A thermophilic group 3 hydrogenase was extensively characterized in this thesis in chapter 6.1. The forth group is composed of membrane-associated, energy-conserving [NiFe]-hydrogenases. These enzymes couple hydrogen generation by oxidation of organic compounds under strictly anaerobic conditions.[215,216,258]

4.3.3. Redox Intermediates

[NiFe]-hydrogenases are capable of working under aerobic and anaerobic conditions (see Fig. 4.3). Early EPR studies on these enzymes revealed two different inactive states: Ni_u-A and Ni_r-B.[61,256,262] Ni_u-A one is an unready species which comprises a slow kinetic reactivation, whereas Ni_r-B reactivates faster. Crystal structure analysis of Ni_u-A in different organisms report either an μ-OOH^- or μ-OH^- and a sulfenato ligand, respectively. A recently combined EPR and DFT study further supports the hydroxide ligation.[13,25,174,175,263] However, a final assignment is still missing. In the Ni_r-B state it was shown that the bridging position is occupied by a hydroxide species.[256,262] Reduction by one electron leads to the formation of the Ni_u-S and Ni_r-S states, respectively. These two Ni(II) species are still inactive and it has been suggested that they still bear their respective oxygen ligand. Two sub-forms of the Ni_r-S state were identified which proposed differences in protonation and a variety of structures were proposed.[20,44,52,144] Recently, the acid-base equilibrium between the Ni-SI_r and Ni-SI_a state was investigated. The photoactivation in combination with isotope exchange experiments revealed the formation of a water molecule at the active site rather than a protonation effect of a terminal cysteine.[247] If the water molecule is released from this species the first catalytically relevant state, Ni_a-S/Ni-SI_a, is formed. This EPR-silent species exhibit an unusual see-saw geometry and a vacant bridging position.[27,103,119] A second one-electron reduction produces the

third paramagnetic Ni_a-C state.[51,63,64,255] Spectroscopic investigations revealed a hydride in the μ-position between the Ni and the Fe.[24,181] Photolysis transforms Ni_a-C into Ni-L which is trapped at low temperatures, but can be reversed at elevated temperatures. Ni-L exists in up to three different sub-forms.[235,246] As a result of this (photo)-conversion, the hydrido ligand dissociates as a proton possibly to a nearby base. Ni_a-C and Ni-L are clearly separated in EPR spectroscopy by their corresponding g-values. This finding has promoted the assumption of a Ni(I) species. However, for a Ni(I) compared to Ni(III) state higher K-edge shifts would be expected but were not detected in XAS.[51] Therefore, the two hydride-derived electrons could create a metal-metal bond. In this regard, Ni-L might be rather described as a prototropic form of Ni_a-C.[112] Alternatively, Ni-L might be a further putative redox intermediate, since it was observed for Hyd1 from *Escherichia. coli* (*E. coli*) at ambient temperatures as well as in a recent ultra fast IR study.[80,81,93,164] Interconversion of Ni_a-C by one further electron leads to the most reduced state termed Ni_a-SR. This EPR-silent species carries a μ-H^- and a protonated terminal cysteine.[111,176,177] Using IR spectroscopy three sub-forms of this species could be identified. How they differ particularly from each other regarding their electronic structure and/or protonation state is yet not assigned.[100]

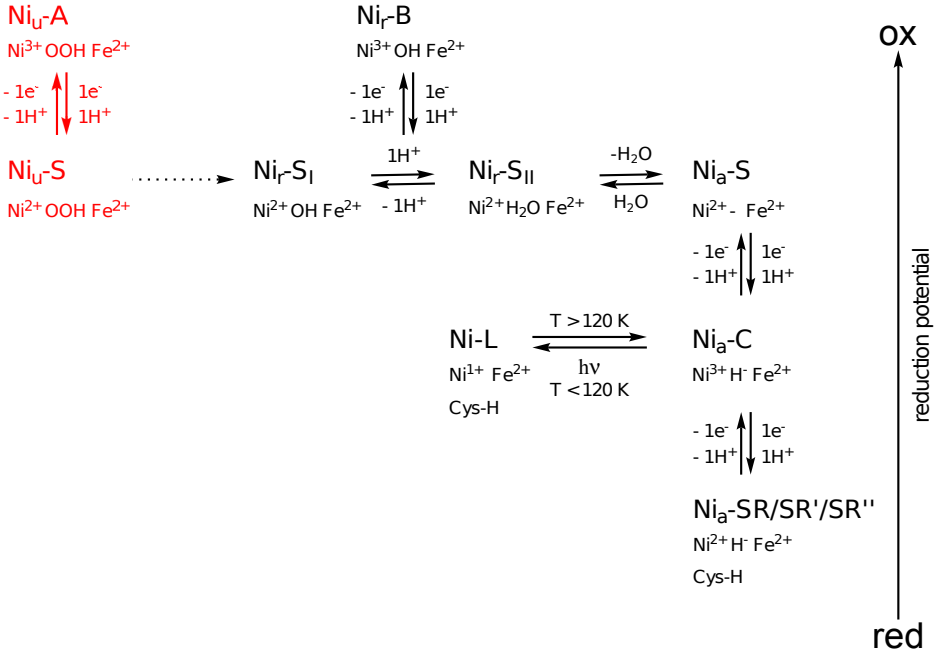

Figure 4.3. Schematic representation of redox states of [NiFe]-hydrogenases. The red-labelled species are only found in O_2-sensitive enzymes. The formal [NiFe] oxidation state is described for each individual intermediate. The presumable third bridging ligand is listed as stated below the species. The subscript nomenclatures are correlated to the catalytic behavior of the individual redox state: a = active, r = ready, u = unready. This schema represents the minimum set of redox intermediates found in [NiFe]-hydrogenases. Especially, soluble hydrogenases, e.g. from *Ralstonia eutropha*, exhibit significant differences. For further reading see chapter 4.3.5.

4.3.4. Catalytic cycle

Hydrogenases catalyze the reversible conversion of H_2 into protons and electrons. However, the activation of the dihydrogen bond is a chemical challenge. Since the molecule is nonpolar and a very weak acid, the H-H bond is very strong and substantially inert. Consequently, breaking the H-H bond demands prior activation which could, in principle, be achieved by two different mechanisms.[237] In the following section fundamental physicochemical properties of this reaction are outlined and discussed. It should be noted that the correct reaction mechanism is still not completely understood. In general, there are two possibilities for dihydrogen activation, oxidative addition and heterolytic cleavage. The latter one requires a polarization of the H-H bond by a frustrated Lewis pair. This term refers to a Lewis acid as well as a Lewis base which are, due to steric hindrance, unable to react with each other. In this case, the Lewis base could be an unprotonated amino acid residue and the Lewis acid an electrophilic transition metal (see 4.4 **A**). On the other hand, oxidative addition would occur through populating the antibonding σ^* orbital of the H_2 molecule. This would create a dihydro complex (see 4.4 **B** and **C**).[27,138,140]

Essentially, the catalytic reaction follows a certain sequence. First, the H_2 molecule binds to the active site, secondly the H-H bond is broken and finally, the resulting protons and electrons are removed towards the cellular electron acceptor(s). The Ni_a-S state is suggested to be the first catalytically relevant intermediate which adopts an unusual see-saw geometry.[27,103] During this process it is proposed that a side on H_2 σ-bond complex is formed. While previous studies implied dihydrogen complex formation at the Fe more recent experimental analysis of possible gas channels and theoretical studies indicate H_2 binding at the Ni.[26,27,123,138,160,237] In Fig 4.4, **A** the heterolytic splitting reaction is displayed. Starting from the Ni_a-S state, binding of dihydrogen would yield the Ni_a-SR state, which is the most reduced active species. In general, either one or both of the metals act as the Lewis acid and the terminal cysteines are the proposed Lewis base or putatively, the arginine located close to the active site.[26,138,237] Formal abstraction of one proton and one electron leads to the paramagnetic Ni_a-C state. Form this point a secondary proton and electron transfer to the protein would end up with Ni_a-S and a new redox cycle could start (indicated by the dashed line). However, Lill *et al.* introduced another possible intermediate, Ni_a-R*, which differs from Ni_a-C by the position of the proton and the electronic structure of the Ni. This proposed species is similar to the observed Ni-L state and may represent an isomer to Ni_a-C in the catalytic cycle.[138] In a recent ultra fast IR study, the presence of two new Ni(I)-I states, comparable to Ni-L, were confirmed. As a result, transient Ni(I/III) states my be further involved in catalysis.[81] Alternatively, a reaction schema for homolytic cleavage was published by Bruschi and coworkers where a transient dihydro complex at a Ni(IV) core is formed (Fig 4.4, **B**). Afterwards, the generally observed reduced states are generated.[27] This interesting proposition of a dihydro species would also account for the two vacant coordination sites at the Ni, regardless, whether the splitting reaction occurs via homolytic or heterolytic cleavage. Finally, another suggested reaction mechanism (Fig 4.4, **C**) for oxidative ad-

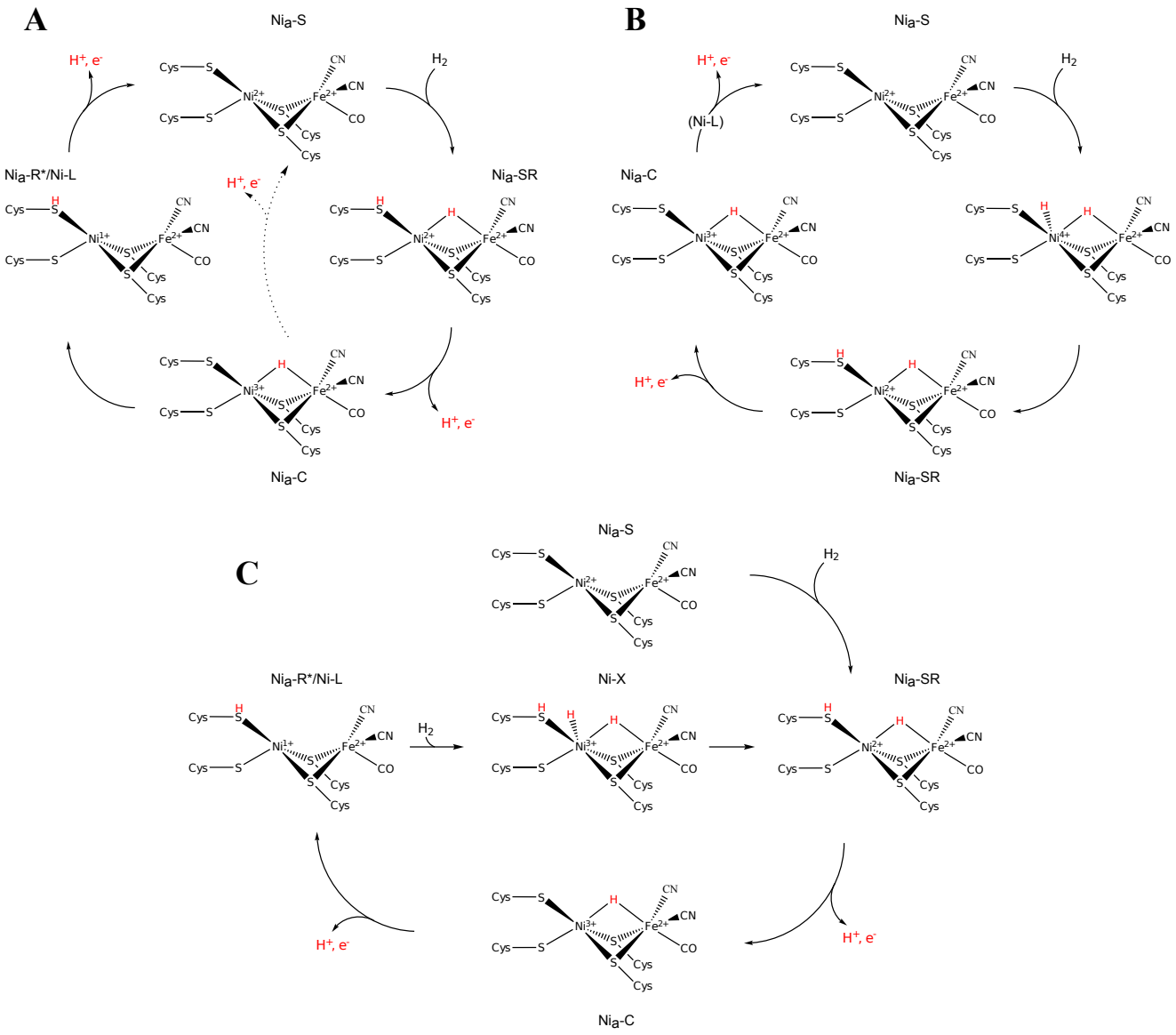

Figure 4.4. Suggested heterolytic (**A**) and homolytic (**B**, **C**) cleavage mechanisms for dihydrogen.

dition involves the Ni_a-R* state as starting point. The addition of a H_2 molecule would create the Ni-X state which contains a Ni(III) ion bound by a bridging and a terminal hydrido ligand. Removal of one proton and one electron yields again the Ni_a-SR state. This proposal excludes the Ni_a-S state from catalysis except for the first cycle. The authors claim that the oxidative addition is energetically favored over heterolytic cleavage. However, both mechanisms include transient and so far unidentified Ni(III/IV) dihydro species. Nevertheless, the experimentally detected species do not favor one mechanism and thus, hydrogen activation may occur one way or the other.

The above outlined details are still insufficient in illustrating the underlying principles in hydrogen cleavage. Especially, considering the biological unusual inorganic ligation sphere of the Fe. This unprecedented coordination seems to be a common and catalytic relevant feature in nature. The understanding of the involvement of the CO and CN^- ligands prevail largely evasive.[27,123] While this moiety was demonstrated to be necessary for H_2 binding at the Fe, their functional role is less coherent for the suggested hydrogen binding and cleavage at the Ni atom.[5,27,34,123,138] Both, the CO and the CN^- molecules are strong field ligands which may alter the metal-metal interactions by tuning the active site's Lewis acid properties or influence the metal substrate chemistry. Notably, the CO ligand has an amphoteric character and is defined by its σ-donor as well as π-acceptor capabilities. The latter may support the catalytically important reversible binding of hydrido ligands, especially in the bridging position. As a result, the metal center and its interactions with the protein environment require further analysis.

4.3.5. Soluble Hydrogenase

Compared to standard hydrogenases illustrated in section 4.3.3 bidirectional [NiFe]-hydrogenases show differences in their redox behavior. The observed states are displayed in 4.3 on the right panel. In case of the O_2-tolerant or soluble hydrogenase (SH) the Ni_u-A state is missing. Furthermore, an IR stretching frequency similar to the Ni_r-B species from standard hydrogenases is experimentally observed, however it is not EPR active and was therefore termed Ni_r-B-like. In addition, a second reduced state, $Ni(II)_a$-SR2, was detected. The underlying physicochemical properties are still a matter of debate. Regardless of those shortcomings, hydrogenases inherit a huge potential in the production of H_2.

The best studied SH model so far is obtained from the organism *Ralstonia eutropha* (*Re*) which consists of six subunits. It directly couples dihydrogen oxidation to NAD^+ reduction and *vice versa*. The two moieties HoxH and HoxY form the hydrogenase and HoxF and HoxU the diaphorese module.[220,251] In particular, HoxH harbors the deeply buried [NiFe] active site. HoxY contains one flavin mononucleotide (FMN-a) which function is still unknown as well as one [4Fe4S] cluster. In HoxU one [2Fe2S] and two [4Fe4S] are found. Finally, the last [4Fe4S] cluster is located in HoxF together with the second FMN-b where NAD(H) production or consumption takes place.[100,132] Two further subunits, HoxI which are supposedly bound to HoxF, complete the enzyme.[32] The re-

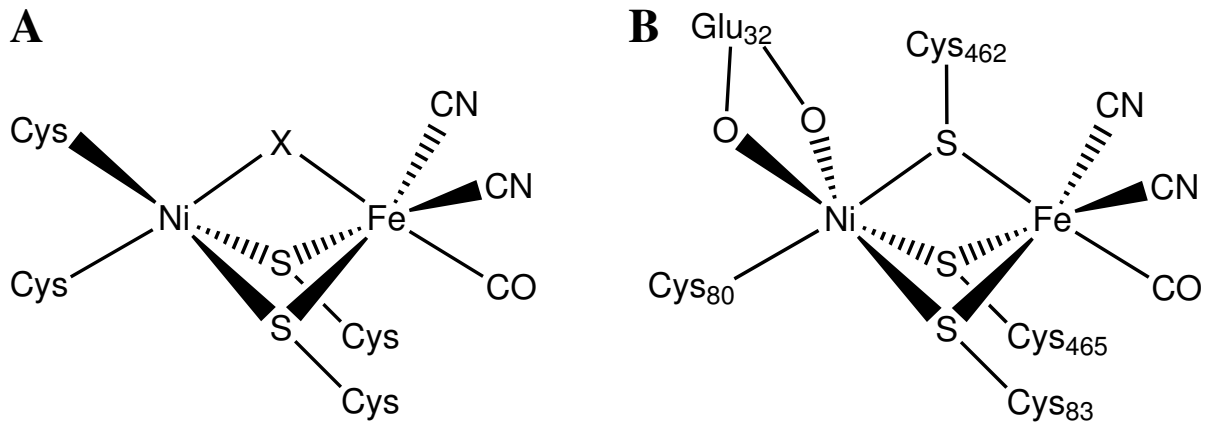

Figure 4.5. **A)** the structure of standard [NiFe]-hydrogenases and **B)** proposed structure of the as-isolated SH from *Hydrogenophilus thermoluteolus*[234]

markable O_2 tolerance and the high turnover rates of the *Re*SH is very attractive to be used in both *in vitro* and *in vivo* studies for H_2-driven NAD(P)H cofactor regeneration in biotechnologically relevant applications.[129,206,207] Regardless of its very efficient NADH recycling, the *Re*SH lacks temperature stability.[202] In this work, a thermostable SH version from *Hydrogenophilus thermoluteolus* TH-1^T (*Ht*) was characterized (see 6.1). This organism been described as an aerobic, facultatively chemolithoautotrophic, hydrogen-oxidizing microorganism, which - like *Ralstonia eutropha* - belongs to the phylogenetic class of β-proteobacteria.[92] It shows optimal chemolithoautotrophic growth with a H_2:O_2:CO_2 gas mixture of 7:2:1 at a temperature of 52 °C.[76] This suggests the presence of at least one O_2-tolerant [NiFe]-hydrogenase. Indeed, a recent study confirmed the presence of an SH-like enzyme in the moderate thermophile.[248] However, neither the corresponding genetic information nor a physiological or spectroscopic characterization of the *Ht*SH is so far available.[248] As outlined in chapter 6.1 DNA sequence of the structural genes of the four *Ht*SH subunits in addition to the gene encoding the *Ht*SH-specific endopeptidase are presented. The *Ht*SH was recombinantly overproduced in *R. eutropha* and - upon purification - characterized by means of bio-chemical and spectroscopic methods. It turned out to be the first characterized [NiFe]-hydrogenase that performs H_2-driven NAD^+ reduction at elevated temperatures and in the presence of O_2. In a recent work, the first crystal structure of a soluble [NiFe]-hydrogenase from *Hydrogenophilus thermoluteolus* was solved.[234] Compared to the proposed structure of the active site of the *Re*SH (Fig 4.5, **A**) the authors describe the shift of one terminal cysteine in the bridging position (Fig 4.5, **B**). In addition, the Ni atom is further coordinated by the carboxylate group of Glu32. This unusual ligation may be the reason for its unprecedented spectroscopic properties described in 6.1. and remains a vivid pool for investigations.

4.4. [NiFe] model complex

Oxygen tolerance of [NiFe]-hydrogenases is an emerging field within the research community. While many model complexes aimed in reproducing reduced catalytic intermediates, less attempts were done for the oxygenated active site.[217]

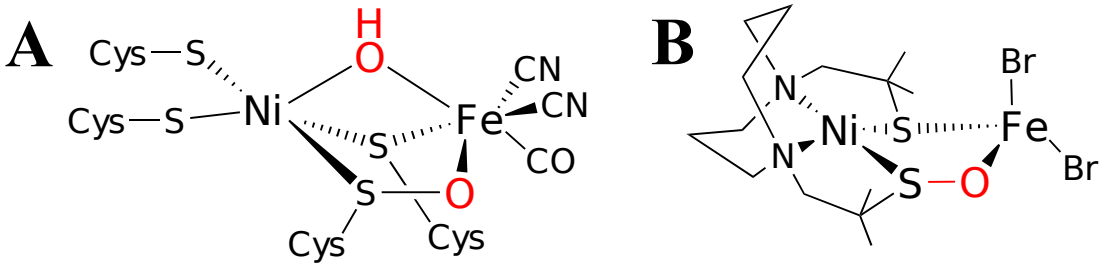

Figure 4.6. Proposed model of the oxygenated active site (**A**) and crystal structure of the synthetic [NiFe] complex (**B**)[140]

The "Knallgas" bacterium *Ralstonia eutropha* (Re) harbors four different hydrogenases. So far, the oxygen tolerance remains unclear for the actinobacterial [NiFe]-hydrogenase, whereas for the other three enzymes different strategies were suggested.[29,47,67,105,129] In particular, the oxygen tolerance of the membrane-bound hydrogenase from this organism is very well studied. Here, the proximal [4Fe3S] cluster plays a crucial role.[67,75] For the bidirectional NAD^+-dependent soluble hydrogenase such as mechanism was ruled out by a combination of mutagenesis, IR and EPR studies.[113] Recently, a (per)oxidase-like activity was detected.[103,105,129] It is proposed that by tautomerization of a hydroperoxido species a bridging cysteine residue is reversibly oxygenated (see Fig. 4.6, **A**). Depending on the position of this μ-oxo ligand the vibrational frequencies of the inorganic ligands are changed, especially, more pronounced for the CN^-. This indirect finding promoted the assumption of a sulfenate moiety. Nevertheless, a direct experimental evidence is still missing. In order to further elucidate structure-function relationships a novel oxygenated, heterobimetallic [NiFe] complex was synthesized (see Fig. 4.6, **B**). This model provides a better understanding whether such a mixed thiolato and sulfenato bridging structure is stable as well as as a reference for (vibrational) spectroscopic studies of the corresponding enzymes. As mentioned above, modeling of [NiFe] active sites has so far concentrated on catalytic relevant reduced states and their inherent reactivity. Molecular mimics of the interaction of O_2 with the heterobimetallic [NiFe] active site are rare. Ogo and coworkers recently monitored the activation of oxygen at [NiFe] complex at low temperatures. However, this attempt led to a Fe(IV) side-on peroxido species which exhibits no biological counterpart.[117] Other S-oxygenated models of mononuclear and homobimetallic [FeFe] thiolato complexes were published by the groups of Darensborough and Weigand.[49,77,269,275] However, up to date, heterobimetallic S-oxygenated [NiFe] complexes with mixed thiolato and sulfenato bridging moieties have not been reported to date and are further outlined in chapter 6.2.

4.5. Molybdenum cofactor

4.5.1. Importance of carbon dioxide reduction (in life)

The extensive use of fossil fuels has dramatically increased the atmospheric concentration of carbon dioxide. The resulting green-house effect is of mayor concern in global warming. Therefore, providing efficient solutions to overcome this problem is an urgent research challenge. The low cost and its abundance makes CO_2 an interesting synthetic compound for the chemical industry. However, carbon dioxide exhibits a high thermodynamic and kinetic stability which hampers its activation in laboratory and large-scale processes. Therefore, catalysis has to be implemented to solve these challenges by using renewable and cheap materials in a sustainable fashion.[41] In this context, the aim of decreasing CO_2 emissions through chemical conversion represents an inspiring approach. It is evident that CO_2 transformation by biological and/or bio-inspired synthetic catalysts into a variety of chemicals would be a beneficial solution. However, in order to apply novel catalysts in an industrial scale, it is necessary to fully understand their physico-chemical properties and the underlying reaction mechanisms. In biology, CO_2 fixation occurs widely and several pathways have been established, such as the reduction to carbon monoxide, the addition to ribulose and/or the reduction to formate.[4,73] Especially, the latter reaction is of particular interest with respect to large scale industrial production because it would provide an alternative fabrication route. Nature has evolved molybdenum- (Mo) and tungsten- (W) cofactor containing enzymes. These so-called formate dehydrogenases (FDHs) are widely spread in archea and bacteria.[96] Here, the formate molecule is a key intermediate in the microbial fermentation cycle. It further serves as an energy metabolite as well as an electron donor during anaerobic respiration.[136] The fundamental goal is to investigate how these enzymes fine-tune the electronic structure of their cofactor and how individual transitions states are generated within the catalytic cycle. The elucidation of these information will help to optimize synthetic molecular catalysts for future CO_2 transformation approaches.

4.5.2. Maturation

Molybdenum- or Tungsten-containing enzymes can be divided into different phylogentic groups depending on the catalyzed reaction, such as **i**) the Xanthine Oxidase Family, **ii**) the Sulfite Oxidase Family and **iii**) the Dimethyl Sulfoxide (DMSO) Reductase Family.[96] In this work, only a FDH from the latter group has been investigated. Therefore, further information given in this thesis will focus just on this particular cofactor.

The DMSO Reductase family is exclusively found in prokaryotes. The active site contains a Molybdenum or Tungsten cofactor, within this thesis referred to as Moco, which comprises a bis-molybdopterin guanine dinucleotide (MGD). The fifth ligand is either a sulfur or an oxygen. Hexa-coordination is achieved by binding of a hydroxo or an amino acid. So far, serine, cysteine, selenocysteine and asparagine were depicted as possible can-

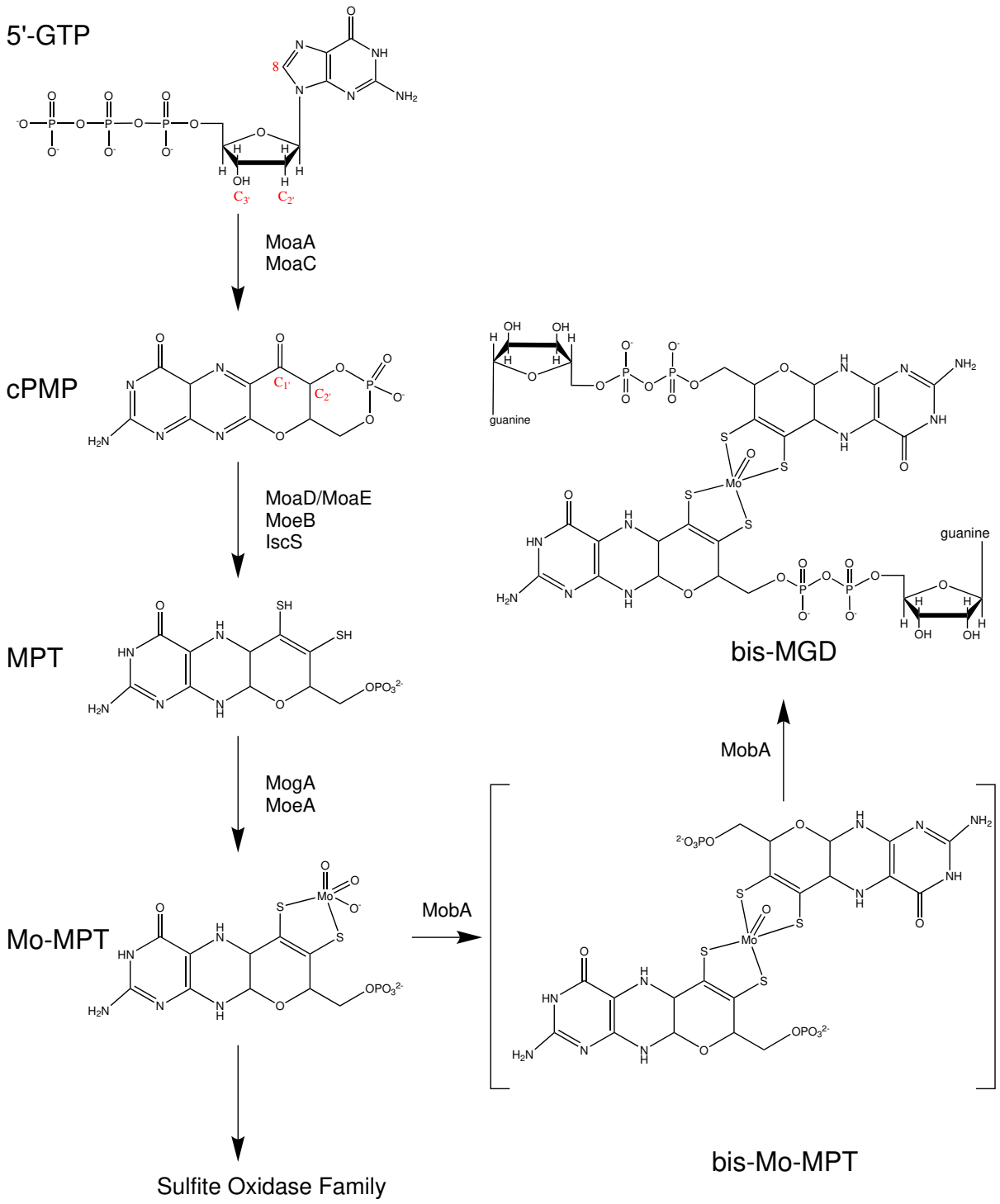

Figure 4.7. Moco biosynthesis pathway for the DMSO Reductase family.

didates. The maturation process is highly conserved in bacteria and archea and can be divided into four steps (see Fig. 4.7 .[89,96] The first substrate in the biosynthesis of Moco is 5'-guanosine triphosphate (GTP) which is transformed by the accessory proteins MoaA and MoaC to cyclic pyranopterin monophosphate (cPMP).[214,277] Within this cascade of reactions the C_8 of GTP is inserted between the $C_{2'}$ and $C_{3'}$ of the ribose.[106,157] The second step involves the molybdopterin (MPT) synthase. This is a heterotetrameric $(\alpha\beta)_2$ complex which consists of two MoaD and MoaE proteins.[213] Their function is to bind two sulfur moieties to the $C_{1'}$ and $C_{2'}$ atoms of the cPMP.[48,189–193] The first sulfuration occurs at the $C_{2'}$ position by one MoaD-SH enzyme resulting in a hemisulfurated molecule. This particular reaction is coupled to the hydrolysis of the phosphate group of the cPMP.[48,278] After this ring opening it is proposed that that the hemisulfurated intermediate shift its location within the MoaE protein. As a consequence the $C_{1'}$ position becomes accessible for the second sulfuration attack. The remaining thioester is hydrolyzed and MoaD and , as products, are released. In the third step the molybdenum atom is inserted to the MPT. This process is catalyzed by the MoeA and MogA proteins.[169,170] Here, MoeA uses adenosine triphosphate (ATP) to produce a MPT-AMP (Adenosine monophosphate) intermediate and MogA transfers the Molybdenum.[124,170] At this stage, the Moco posses a tri-oxo ligation which is its basic form. Now, it can either be directly incorporated into enzymes of the Sulfite Oxidase Family or further modified by nucleotide addition and exchange of oxo ligands.[208] In the forth step the bis-MGD is assembled which is catalyzed by the MobA protein. This two-step reaction requires GTP and the Mo-MPT as substrates. First, the bis-Mo-MPT is synthesized and then two guanosine monophosphate (GMP) molecules are added to the phosphates resulting in the bis-MGD.[127,180] This bis-MGD can now be used as active site by members of the DMSO Reductase family. However, for the FDH of *Rhodobacter capsulatus* (Rc) a further modification of the Mo ligation sphere is necessary. The oxo ligand has to be substituted by a sulfido moiety.[225] The importance of the active site ligation sphere was thoroughly investigated in this thesis and is outlined in chapter 6.3 showed that the accessory assembling proteins FdsC and FdsD are essential for enzymatic activity. Surface plasmon resonance measurements exhibited an interaction between FdsC, FdsD and MobA. FdsD might play a role in oxygen protection of the Moco, since it is only discovered in organisms which obtain an oxygen-tolerant FDH (see Fig. 4.8).[21]

4.5.3. Enzymatic Structure and Function

The NAD-dependent and Molybedenum-containing FDH from *R. capsulatus* is the first discovered oxygen-tolerant enzyme. It harbors a Moco as active site, five [4Fe4S], two [2Fe2S] clusters, a flavin mononucleotide (FMN) (see Fig. 4.8) and catalyzes the oxidation of formate to CO_2 by subsequent reduction of NAD^+ to NADH, which provides its electrons to the respiratory chain.[65] The *R. capsulatus* FDH forms a $(\alpha,\beta,\gamma)_2$ heterotrimer (see Fig. 4.8). The complete characterization of this complex by Hartmann *et al.* showed that the α-subunit binds the bis-MGD cofactor.[88] So far, the redox chemistry is purely

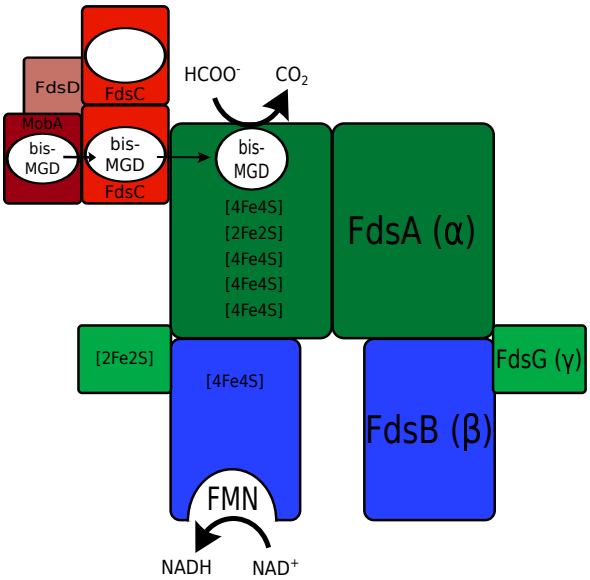

Figure 4.8. Schematic overview of the FDH and its accessory assembling proteins. The three subunits FdsA, FdsB and FdsG form the FDH which dimerizes.

discussed on different oxidation states of the Mo atom and less attention has been paid to the ligation of the entire cofactor. In particular, as the MPT is highly versatile in adopting different redox states, as well. It is proposed that the dithiolene moiety modulates the electronic structure of the Mo atom and therefore, controls its redox properties.[109,257,273] For instance, the dithiolene chelate is capable of forming three redox conformations. It can either be obtained in its dithiolene form (dianion, **1**), radical anion (**2**) or dithione (fully oxidized, **3**) as displayed in Fig 4.9.[153,163,166,183]

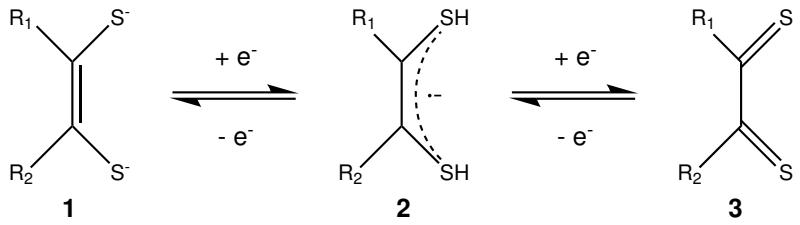

Figure 4.9. Different redox states of the dithiolene unit

These redox tuning effects are mediated by the conjugation of the covalent system between the sulfur, the carbon backbone of the pyrano ring and the heterocyclic pterin.[154] Furthermore, the dithiolone is able to adopt strong structural distortions. Higher Mo oxidation states generate stronger fold angles which are observed in crystal structures of various Moco enzymes.These structural variations also influences the electron donation and accepting properties.[109,257] Using these two types of modulation the dithiolene moiety is commonly referred to as an "electronic buffer".[273] The second redox active part of

the MPT is the pterin heterocycle. As displayed in Fig 4.10 the pterin can undergo two proton-coupled one electron reductions to 5,6,7,8-tetrahydropterin. In general, nitrogen-rich molecules are considered as electron-poor compounds. This deficiency will remove electron density from the dithiolene group. Multiple tautomers of the pterin such as the semi-reduced form could additionally fine-tune the electronic environment. Especially, considering that, these structures often differ strongly from ideal octahedral and trigonal prismatic orientations.[212] Since, the organic part of the bis-MGD cofactor is not covalently bound to the enzyme, H-bonding is critical to ensure an appropriate conformation. Many functional groups are located at the pyranopterin moiety. Modulation in these H-bonding interactions might be a possibility of how the protein scaffold communicates with the active site. Finally, the pyran ring can undergo ring opening and cyclization reactions.[70,188] Currently, there are many X-ray structures of Moco-containing enzymes available, which exhibit a fully reduced MPT cofactor bound to Mo. However, in a few bacterial examples the dithiolene ligands emerge as a mixture of closed-cyclic as well an open pyrano ring conformation.[212,240,274] It is not understood whether these open ring formations are a result of radiation damage or naturally occurring.

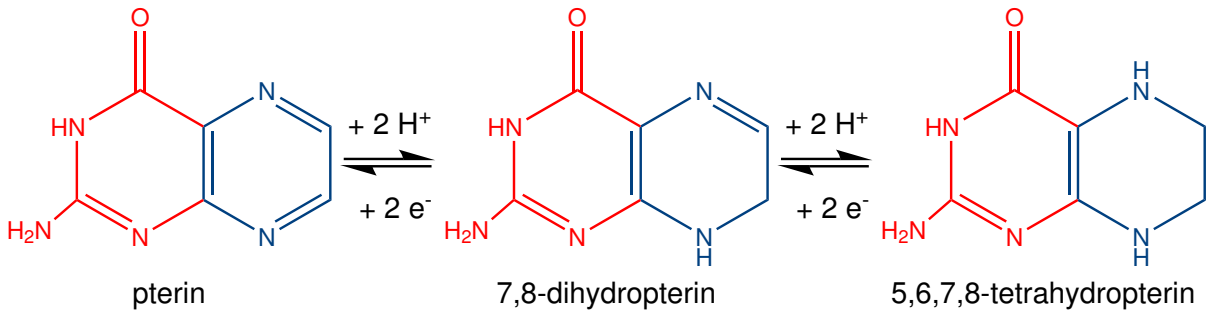

Figure 4.10. Different redox states of the pterin heterocycle

In a recent publication the crystal structure of the formyl-methanofuran dehydrogenase was solved which catalyzes the reduction of CO_2 to formyl-methanofuran. Its W-containing metal center comprise high homology with solved FDH structures.[97–99,265] It is striking how highly conserved peptide residues around the active site of FDHs are despite their differences in subunit composition and cofactor binding. For instance, one histidine and one arginine are found close to the active site in all Mo and W-containing FDHs. Single point mutations of these two residues lead to dramatically increased K_M values and underline their importance for a proper catalytic function.[10,90]

4.5.4. Catalytic cycle

Since the first crystal structure of the *E. coli* FDH-H was reported in 1997 several catalytic mechanisms had been proposed.[22] Based on the FDH-H structure a hexacoordinated Molybdenum atom was suggested. Its ligation sphere was interpreted to consist of two bis-MGD cofactors, a selenocysteine (SeCys) and a OH^- (see Fig. 4.11, A). The authors

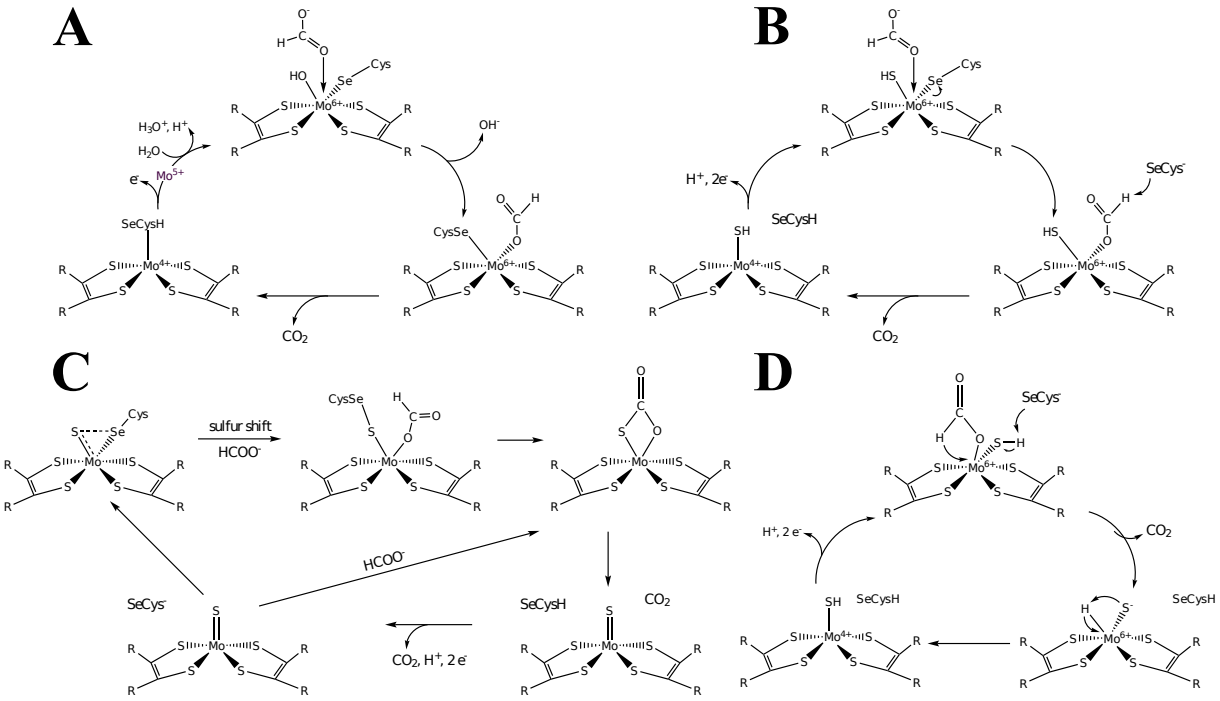

Figure 4.11. **A** Catalytic mechanism proposed by Boyington *et al.*[22] and **B** catalytic mechanism suggested by Raaijmakers[200] and **C** sulfur shift mechanism introduced by Mota[162] and **D** hydride abstraction presented by Tiberti[249]

deduced that the formate coordinates directly to the Mo(VI) and replaces the hydroxide ligand. After cleavage of the formate C-H bond, the two electrons are transferred to the Mo and CO_2 is released. The OH^- ligand is newly generated from water thereby restoring the active site.[8,22,116] In a second refinement of the structure by Raaijmakers *et al.* the hydroxide group was replaced by an sulfur atom which was hypothesized to be either a sulfido or a thiol group (see Fig. 4.11, B). Additionally, a peptide loop was reinterpreted to be closer to the active site. This remodeling led to a different mechanism where the formate replaces the SeCys followed by proton transfer to the subsequently free selenol group. Leopoldini and coworkers investigated the thermodynamics of the formate oxidation reaction pathway at a Mo-cluster using DFT. In their study the activation energies support the assumption that the proton is abstracted by the selenol moiety.[137,199,200] A more extensive computational study including peptide residues around the active site with a predicted involvement in formate oxidation was published by Mota *et al.*[162] They propose a (partial) bond between the sulfido group and the SeCys which is a consequence of the aerobic purification of the enzyme. Therefore, an activation step is required involving the so-called "sulfur-shift"(see Fig. 4.11, C). Here, the Selenium shifts out of the first coordination sphere of the Mo while forming a bond with the sulfido group and remaining in the second coordination sphere. This interpretation is based on the carboxylate shift observed for other systems.[36,57,72] After this activation a vacant coordination site at

the Mo is exposed and leads to the binding of the substrate. Formate oxidation occurs via a two step reaction. First, the proton is abstracted by the SeCys and second CO_2 and two electrons are released thereby leaving a pentacoordinated Mo atom which can directly undergo the next catalytic cycle. However, this model is unable to confirm the Mo^{5+} oxidation state which is observed in EPR studies.[36,162] The last mechanisms based on DFT studies was reported by Tiberti and coworkers.[249] Here, a hydride attack at the Mo ion is suggested (see Fig. 4.11, D). Nevertheless, all the computed structures of the Moco are only coordinated by five sulfur atoms which is clearly disproven by recent X-ray absorption spectroscopy (XAS) and resonance Raman data described in this thesis in chapter 6.3.[225]

In the past years two mechanisms have been published which are based not only on crystallographic and DFT studies but also on spectroscopic investigations. These two catalytic cycles are shown in Fig 4.12. Based on EPR spectroscopic data of the Mo^{5+} oxidation state, Niks *et al.* propose a hydride attack at the sulfido group of the Moco (see Fig. 4.12, **A**).[172] This assumption is based on the fact that a proton hyperfine coupling is detected upon reduction of the enzyme. The authors relate this to one strongly coupled proton near the active site. Similar couplings have been monitored in DMSO reductase, where hydride binding is also involved.[17] In incubation experiments with [^{2}H]-formate this proton hyperfine splitting disappears but is regained if the sample is thawed, then incubated shortly at room temperature and afterwards refrozen. In consequence, the deuteron/proton is considered to be solvent exchangeable. Interestingly, a hyperfine coupling is also found in the dithionite reduced sample in which the proton has to be generated elsewhere. If the potential of the reductant is negative enough, this foster for Mo^{5+} generation with unknown proton position. It is obvious, that a magnetic coupling is present upon reductive treatment of the FDH. Albeit, its origin is not fully understood, yet. The mechanism proposed by Niks confirms certain features in the recorded EPR spectra. However, the Mo^{6+} as well as the Mo^{4+} states are EPR silent and were not made accessible by other spectroscopic techniques.[150] A recent kinetic study by Maia *et al.* carried out on the FDH of *Desulfovibrio desulfuricans*. Thereby, the FDH was also treated with cyanide overnight, resulting in an inactive enzyme. In Xanthine dehydrogenases it is knwon that incubation with CN^- leads to a desulfurization (Mo=S to Mo=O conversion) of the active center. The released product SCN^- was subsequently measured by the SÖRBO assay, which is reversible under suitable reaction conditions.[167] Regardless, no SÖRBO assay was performed by Maia. Albeit, no reversibility test was carried out, the authors assume the *Dd*FDH reacts in the same way as the Xanthine dehydrogenase. Thus, they suggest the enzyme inactivation results from the SCN^- formation, thereby designating the sulfido group essential for catalysis. But, the authors do not perform any further (vibrational) spectroscopy in order to prove their interpretation of the desulfurization. In conclusion, they support, based on the necessity of the sulfido group at the Mo ion, the hydride attack mechanism proposed by Niks. Contrarily, such a prolonged incubation with CN^- may also lead to a coordination of the corresponding cofactor metals. As shown recently in an IR spectroscopic study of the Carbon monox-

ide dehydrogenase from *Carboxydothermus hydrogenoformans*, that revealed a leaching of cofactor metals to $[M(CN^-)_x]$.[42] Therefore, such an alternative metal coordination might be a more sophisticated explanation for the enzyme's inactivation.

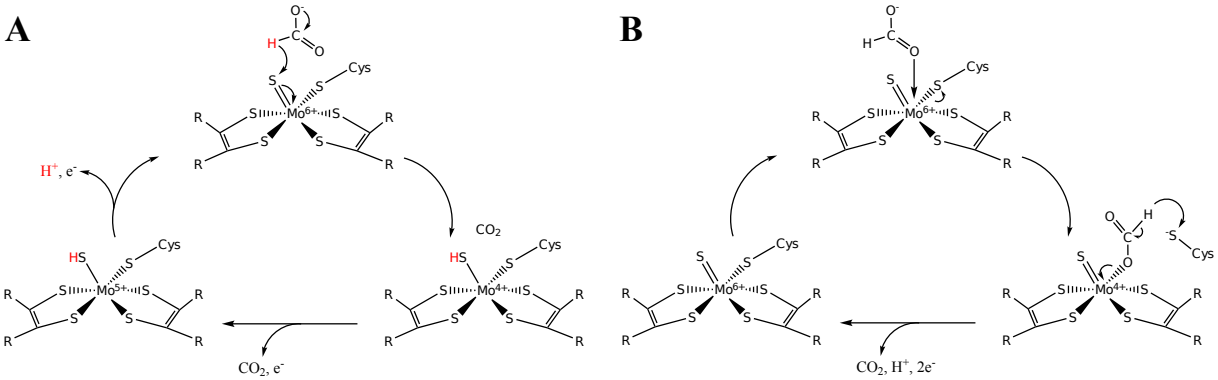

Figure 4.12. **A** hydride attack mechanism proposed by Niks *et al.*[172] and **B** direct formate binding at the Molybdenum suggested by Hartmann *et al.*[88]

A different catalytic cycle is established by Hartmann and coworkers (see Fig. 4.12, **B**).[88,90,225] Here, a direct formate binding at the Mo ion was suggested. As mentioned above, a prerequisite is for this reaction is a vacant coordination site which is provided by the dissociation of the Cys386. The latter abstracts then the proton, while the electrons are transferred to the Moco and CO_2 is subsequently released. Additionally, the work included the investigation of the reduction of nitrate to nitrite as alternative reaction of the *Rc*FDH. Such oxo transfer reactions have been reported for several Mo-containing enzymes.[96] The *Rc*FDH nitrate reduction activity is 4 orders of magnitude lower than its formate oxidation. Thus, it has no physiological purpose. Nevertheless, such a reaction type would only be feasible if the Mo displays a vacant coordination position. In addition, an iodacetamide assay coupled to a mass spectrometric investigation was performed. The mass analysis shows explicitly that this chemical reacts with the free sulfur group of Cys386, thereby inactivating the enzyme.[90] Replacement of this residue by single point mutation leads to an inactivity regarding formate oxidation but not nitrate reduction. Thus, these experiments underline the importance of the Cys386 during catalysis. Furthermore, our theoretical calculations exhibit stronger binding energies to the Mo^{6+} redox state for formate binding compared to cysteine (see chapter 6.3). The proposed mechanism highlights the necessity of Cys386 but cannot explain the observed paramagnetic phenomena upon reduction. As shown by earlier XAS studies the active site of the WT is a hexa-coordinated Molybdenum ion in oxidation state 6+, which is ligated to two dithiolene moieties, a cysteine and an inorganic sulfido ligand.[225] However, the data displayed a 50/50 mixture between an oxo and a sulfido species. Furthermore, the authors observed noninteger numbers of Mo-O bonds which indicate heterogeneity at the active site. So far, this is the only work describing a reduced Mo^{4+} species, which coordinates to the oxygen of a putative formate molecule. If this metal-oxo bond truly derives from formate

binding or represents in parts the mixed oxidation states and/or differences in the ligation sphere of the Moco awaits further analysis. Contrary to other experimental findings, no structural interpretation for an EPR-active intermediate is provided by the XAS data. Notably, a recent electrochemical study the direct binding mechanism is supported. Here, the inhibition of the Moco by azide and several small molecules was investigated. The authors show that the inhibition was stronger in the Mo^{6+} than in the Mo^{4+} state.[211] However, no spectroscopic evidence was supplied, which could prove the Mo^{x+}-N_3 binding. An IR spectroscopic approach to verify this argumentation was experimentally and theoretically performed in chapter 6.3 of this thesis.

In conclusion, both spectroscopically derived catalytic cycles cover specific aspects of the experimental observations but also have inherent shortcomings to explain the entity of recorded (spectroscopic) data. Therefore, more work is necessary in the future to solve open questions.

5. Methods and Materials

5.1. Gene sequence and cloning

5.1.1. [NiFe]-hydrogenase

Sequence alignment, gene cloning, cell growth, protein purification and biochemical analysis were carried out by Janina Preissler and supported by Dr. Lars Lauterbach from the group of Dr. Oliver Lenz at the Technischen Universität Berlin.

The *Ht*SH-derived gene cluster containing *hoxFUYHW* was amplified by PCR using the primers

5'-agaacctgtacttccagggcgcaacacgaggaggaggaac-3'

and

5'-ctcggtacccggggatccatacctcctcttcgtgggtgaaaaaac-3'

and genomic DNA from *Hydrogenophilus thermoluteolus* TH-1^T as template. The underlined bases of the primers are complementary to plasmid pGE837, which is a pCM66[151] derivative carrying a XbaI-BamHI-cut fragment from plasmid pGE770[129] with $P_{SH-Strep}$ *hoxF* from *Ralstonia eutropha* H16 followed by a sequence encoding a GGGENLYFQG linker with a TEV cleavage site (underlined residues). Plasmid pGE837 was linearized by inverted PCR using primers 5'-atggatccccgggtaccga-3' and 5'-gccctggaagtacaggttctcg-3', and the 7.9-kb product served as recipient of the *Ht hoxFUYHW* PCR amplicon, which was inserted according to the Gibson Assembly® manual (New England BioLabs). The resulting plasmid carries the *Ht hoxFUYHW* genes under control of the SH promoter of *R. eutropha*[229], whereby the 5' end of the *hoxF* gene was equipped with a linker sequence and a *Strep*-taq II encoding sequence. A $P_{SH} - hox_{Strep}FUHYW$ fragment was cut out with Eco53KI and XbaI and the resulting 5.7 kb fragment was inserted into the ScaI-XbaI-cut vector pEDY309.[118] This yielded plasmid pJP09, which was subsequently transferred by conjugation to *R. eutropha* HF1054, which is a HF424[152] derivative carrying an additional inframe deletion in the *hoxI* gene.

5.1.2. Formate dehydrogenase

Sequence alignment, gene cloning, cell growth, protein purification and the entire biochemical analysis were performed by Dr. Tobias Hartmann and PhD. Benjamin Duffus

from the group of Prof. Dr. Silke Leimkühler at the Universität Potsdam. In the following a brief review is given as published elsewhere.[88]

The construct for expression of the *Rhodobacter capsulatus fdsGBACD* operon was cloned after PCR amplification of the gene with respective primers using chromosomal *R. capsulatus* DNA as template. The *fdsGBACD* DNA fragment was ligated into the pTrcHis vector with NheI-SalI restriction sites, and the resulting plasmid was designated pTHfds05. The *fdsG*, *fdsB* and *fdsA* genes were introduced into the pTrcHis vector after PCR amplification with the NheI-SalI restriction sites, and the resulting plasmid was designated pTHfds04. For coexpression, *fdsC*, *fdsD* and *fdsCD* were cloned into the NdeI-XhoI sites of the pACYCduet-1 vector, and the resulting plasmids were designated pTHfds03, pTHfds12, and pTHfds07, respectively. The *fdsG* and *fdsB* genes encoding the diaphorase subunit of *Rc*FDH were cloned into the pTrcHis vector by use of the NheI-SalI sites.

5.2. Protein expression and purification

5.2.1. [NiFe]-hydrogenase

Strain *R. eutropha* HF1054 (pJP09) was grown heterotrophically in a mineral salts medium containing a mixture of 0.05% (w/v) fructose and 0.4% (v/v) glycerol (FGN medium) at 30 °C as described previously.[75] Upon reaching an optical density at 436 nm of 9-11, the culture was collected, and the cells were harvested by centrifugation at 8850 × g for 15 min at 4 °C. The cell pellet was resuspended in 50 mM KPO_4, pH 7.2, containing 15-20% (v/v) glycerol, 5 mM $MgCl_2$, 0.5 mM $NiCl_2$, and protease-inhibitor cocktail (EDTA-free Protease Inhibitor, Roche). The extract was furthermore supplemented with 5 mM NAD^+ in order to keep the *Ht*SH in the oxidized state, which is thought to prevent extensive oxidative damage through reactive oxygen species.[129] After two passages through a chilled French press cell at a pressure of 125 MPa, the soluble extract was separated from solid cell constituents by centrifugation at 72500 × g for 45 min. The supernatant was loaded onto a 2 mL *Strep*-Tactin Superflow column (IBA), which was previously equilibrated with resuspension buffer. After washing with at least 6 column volumes of resuspension buffer, the protein was eluted in resuspension buffer containing 5 mM desthiobiotin. A final concentration of 20-30 mg mL^{-1} of purified protein was achieved after concentration with Ultra Centrifugal Filter Units (Amicon).

In order to obtain *Ht*SH protein with homogeneous subunit stoichiometry, size exclusion chromatography was conducted after affinity chromatography. An amount of 200 μL of the concentrated *Ht*SH eluate was loaded onto a Superdex 200 10/300 GL column which was previously equilibrated with the same buffer used for affinity chromatography. Using an ÄKTA pure system, the flow rate was held at 0.2 $mL \cdot min^{-1}$, and protein elution occurred at approximately 0.3 column volumes as observed by UV/vis absorption at 280 nm and 420 nm. Protein fractions of 0.4 mL were collected, and the *Ht*SH subunit composition was checked by SDS-PAGE according to Laemmli *et al.*[126] After determining

the H_2-dependent reduction of NAD^+ activity, fractions with highest specific activities and homogeneity were pooled and again concentrated using Ultra Centrifugal Filter Units (molecular weight cut-off of 100 kDa).

5.2.2. Formate dehydrogenase

*Rc*FDH was expressed in *E. coli* MC1061 cells transformed with pTHfds05. Cells were grown at 30 °C and shaking. in LB medium containing 1 mM molybdate, 20 μM isopropyl thio-β-*D*-galactoside, and 150 $\mu g \cdot mL^{-1}$ ampicillin, beginning with a 1 : 500 dilution of a preculture (same supplements, 12 h, 37 °C, no shaking), for 24 h. The apo-form of *Rc*FDH lacking the bis-MGD cofactor was obtained after expression in *E. coli* RK5200 $\Delta moaA$ cells[241] without supplementation with molybdate. After growth, cells were harvested, resuspended in 50 mM NaH_2PO_4 and 300 mM NaCl (pH 8.0), and used directly for purification or stored at -20 °C.

All purification steps were performed at 4 °C on ice or inside a cold chamber. *E. coli* cells were lysed either by sonication (HTU Soni130; G. Heinemann Ultraschall und Labortechnik, Schwaebisch Gmuend, Germany, total time, 5 min; amplitude, 70%; bursts every 3 s for 2 s) or with a cell disruptor system (Constant Systems LTD, Northants, UK, two loadings, 135 MPa pressure), depending on the amount of cells. Cell debris was spun down at 21000 × g for 1 h, and loaded twice onto a self-packed Ni^{2+}-nitrilotriacetic acid column (0.3 mL of matrix per liter of culture). After washing with 20 column volumes of 10 mM and 20 mM imidazole in 50 mM NaH_2PO_4 (pH 8.0) and 300 mM NaCl buffer, *Rc*FDH was eluted with the same buffer containing 250 mM imidazole. With PD-10 columns (Sephadex G-25 M; Amersham Biosciences, Uppsala, Sweden), the buffer was changed to 75 mM potassium phosphate (pH 9) and 10 mM azide: These small anions stabilize the Moco. Samples were concentrated to 2 mL with ultracentrifugation devices (VIVASPIN 20, 50-kDa cut-off; Sartorius AG, Goettingen, Germany). Size-exclusion chromatography was carried out at 4 °C on a Superose 12 column (GE Healthcare, Uppsala, Sweden) equilibrated in 75 mM potassium phosphate (pH 9) and 10 mM KNO_3 or 10 mM azide. Fractions containing *Rc*FDH were identified by SDS/PAGE,[126] combined, frozen in liquid nitrogen, and stored at -80 °C until use. Protein concentrations were determined by measuring the absorption at 280 nm, with ε = 169 500 $M^{-1} \cdot cm^{-1}$ for *Rc*FDH samples.

5.3. Enzymatic assays of the [NiFe]-hydrogenase

All enzyme measurements were performed in the presence of defined gas mixtures unless stated otherwise. Prior to use in enzyme assays, the buffers were saturated with the respective gases. Buffers with 100% gas-saturation (1 bar, 50 °C) contained 720 μM H_2, 940 μM O_2 or 483 μM N_2. Buffers containing gas mixtures were prepared by mixing individual buffers with 100% gas saturation. The head space of the reaction vessels was kept as small as possible to avoid degassing of solutions. H_2-driven NAD^+ reduction

of purified *Ht*SH in soluble extracts was determined at 50 °C in a buffer-filled, rubber-sealed cuvette. The reactions were started by the addition of enzyme, and the absorbance increase at 365 nm due to NADH accumulation was monitored spectrophotometrically using a Cary 50 (Varian). The pH-dependent *Ht*SH activity was measured by using two different strategies: First, to minimize the influence of different buffer components on SH activity, a broad-range buffer system (pH 4.5-9) composed of 16 mM citrate, 16 mM Tris, and 16 mM glycine was used. The buffer system was adjusted at 50 °C with appropriate acids or bases to the desired pH values. Second, SH activity was also tested in the individual buffers mentioned above. Temperature-dependent activity measurements were performed in 50 mM bis-Tris, pH 6.5, containing 0.75 mM TCEP (replacing Dithiothreitol (DTT)), 0.5 mM $NiCl_2$, 5 mM $MgCl_2$ and 2 μM FMN. This owes to the fact that DTT precipitates in $NiCl_2$- and $MgCl_2$-containing 50 mM KPO_i buffer at temperatures above 40 °C.

NADH-driven H_2 production was measured with a modified Clarktype electrode[267] at 50 °C in 50 mM bis-Tris, pH 6.5, containing 5 mM $MgCl_2$, 0.5 mM $NiCl_2$, 0.75 mM TCEP, 2 μM FMN and 1 mM NADH. The buffers as well as the additives were saturated with N_2 before mixing, and the reaction was started by the addition of enzyme. Diaphorase activity of the SH was recorded spectrophotometrically as NADH-dependent benzyl viologen reduction at 50 °C in buffers with different pH values (composition see above), containing 5 mM benzyl viologen (BV), 1 mM NADH, and 90 μM dithionite. H_2-dependent reduction of BV (5 mM) was tested at 50 °C in buffers with different pH values (composition see above). Prior to use, the buffers were saturated with H_2.

In order to determine affinity constants for NAD^+ or NADH, the initial reaction velocities for H_2-dependent NAD^+ and NADH-dependent BV reduction, respectively, were measured at 50 °C and varying substrate concentrations. The recorded slopes were plotted against the substrate concentration and fitted to the Michaelis-Menten kinetic using the program Origin 2016 Version 94 E.

Determination of affinity towards H_2 was performed amperometrically by mixing different volumes of H_2- and N_2-saturated buffers (50 mM bis-Tris, pH 6.5, 5 mM $MgCl_2$, 0.5 mM $NiCl_2$) to a total volume of 1.3 mL in the reaction chamber of a modified Clark electrode. The assay contained further the natural electron acceptor, NAD^+ (1 mM), in addition to 0.75 mM TCEP, and 2 μM FMN. The reaction was started by enzyme addition, and the resulting current change was recorded. The derived reaction velocities were plotted against the H_2 concentration and fitted to the Hill equation using Origin 2016 Version 94 E.

5.4. Protein, metal, and FMN determination

5.4.1. [NiFe]-hydrogenase

The protein concentration was determined with the Pierce™ BCA Protein Assay Reagent Kit (Pierce, USA) using bovine serum albumin as the standard. The flavin mononu-

cleotide concentration in protein samples was analyzed fluorometrically as described previously.[130,220] Iron and nickel contents of purified *Ht*SH samples were analyzed by inductively coupled plasma optical emission spectroscopy (ICP-OES) as published previously.[168] Final numbers were derived from two biological replicates, while each sample was measured three times (three technical replicates).

5.4.2. Formate dehydrogenase

The metal content (Mo, Fe) was measured with ICP-OES. Samples of 500 μL (10-30 μM) were mixed with the same volume of 65% HNO_3, and wet ashed at 100 °C overnight. Samples were diluted with 4 mL of Millipore water, and applied to an Optima 2100 DV instrument (PerkinElmer Life and Analytical Sciences, Waltham, MA, USA). The multielement Standard XVI (Merck, Darmstadt, Germany, for Mo and Fe) were used for calibration and quantification. The resulting mass concentrations were related to percentage saturation of molybdenum according to complete saturation of FeS clusters (five $[Fe_4S_4]$ clusters; two $[Fe_2S_2]$ clusters).

5.5. Sample preparation

IR and EPR sample preparation of [NiFe]-hydrogenase

For the characterization of as-isolated *Ht*SH, protein fractions were concentrated to approx. 0.3 mM using Amicon Ultra 0.5 mL Centrifugal Filters (Merck KGaA) and measured without further treatment. Samples of reduced *Ht*SH were prepared using different procedures. Prior to all reductive treatments, buffers were purged with Ar for 30 min, and O_2 was removed from protein samples by ten consecutive cycles of Ar purging and vacuum exertion. Partial reduction of the enzyme was achieved by 30 min incubation of 0.03 mM *Ht*SH with 2 mM TCEP and 5 mM NADH at 50 °C in an anaerobic, N_2-filled glovebox. After these treatments, the samples were concentrated to approx. 0.3 mM, and IR transmission cells and EPR tubes were purged with N_2 prior to loading. To further reduce *Ht*SH, solutions containing 0.03 mM of protein were incubated with 2 mM TCEP, 5 mM NADH, and 1 bar O_2-free H_2 (O_2 was removed using a Varian Gas Clean Oxygen Filter PIN CP17970) in H_2-saturated buffer at 50 °C for 30 min in an anaerobic chamber (95% N_2, 5% H_2). The H_2 stream was enriched with H_2O to avoid sample drying. Prior to measurements, samples were concentrated to 0.3 mM, and IR transmission cells and EPR tubes were purged with H_2. Aliquots of all samples were directly injected into an IR transmission cell for subsequent characterization, while the remainder was transferred to EPR tubes, quenched in cold ethanol (ca. 210 K) and stored in liquid nitrogen for further analysis.

IR, RR and EPR sample preparation of formate dehydrogenase

EPR samples were prepared by PhD. Benjamin Duffus. For the characterization of as-isolated *Rc*FDH, protein fractions were concentrated to approx. 1 mM - 1.5 mM using Amicon Ultra 0.5 mL Centrifugal Filters (Merck KGaA) and measured without further treatment. A different procedure was applied for the reduced *Rc*FDH samples. Prior to all reductive treatments, buffers were purged with Ar for 30 min. O_2 was removed from protein samples by 3 times anion-free buffer exchange inside an anaerobic, N_2-filled glove box using the above mentioned centrifugal filters and centrifugation was performed at 11000 × g. *Rc*FDH samples of approx. 1 mM - 1.5 mM were incubated either with 10 mM formate, [^{2}H]-formate or NADH and mixed thoroughly for 5 s. For RR samples, 2 μL enzymatic sample was pipetted on a quartz holder and subsequently frozen in liquid nitrogen. Samples for EPR measurements were diluted to approx. 0.3 mM, quenched in cold ethanol and stored in liquid nitrogen for further analysis.

In case of IR samples, buffer exchange regarding removal of O_2 was performed in the presence of the spectroscopic marker azide (10 mM). Reductive treatment followed the above mentioned procedure. As-isolated and reduced protein samples were subsequently injected into the transmission cell as stated for [NiFe]-hydrogenase.

5.6. [NiFe] model complex

5.6.1. Synthesis

The synthetic design and work was performed by Dr. Nils Lindenmaier from the group of Prof. Dr. Matthias Driess from the Technische Universität Berlin.[140]

Unless otherwise stated, all experiments were carried out under dry oxygen-free nitrogen using standard Schlenk techniques. Solvents were dried by standard methods and freshly distilled prior to use. Ni(bmmp-daco) and Ni(bmmp-daco)*SO* (bmmp-daco = *N,N'*-bis(dimethyl)-mercaptopropyldiazacyclooctane) were prepared according to procedures reported in the literature.[30] Iron(II) dibromide was purchased and used as received from Sigma-Aldrich. The ^{18}O-labelled H_2O_2 solution (2-3% in H_2O, 90 atom % labelled) was purchased and used as received from Icon Isotopes. Elemental analyses and electrospray ionization mass spectrometry (ESI-MS) were performed by the analytical laboratory and MS-service in the Institute of Chemistry, Technische Universität of Berlin, Germany.

[Ni(bmmp-daco)SO]$FeBr_2$ 1: To a suspension of 61 mg (280 μmol) iron(II) bromide in 15 mL acetonitrile a solution of 100 mg (280 μmol) Ni(bmmp-daco)SO in 10 mL acetonitrile was added while stirring. The reaction mixture was kept stirring at ambient temperature for two hours and subsequently filtered. After evaporating the solvent, the product was obtained as a red-brown solid (120 mg, 200 μmol, 72% yield). Crystals suitable for single crystal X-ray diffraction were obtained by diffusion of diethyl ether vapor into the filtrated reaction mixture at room temperature. The title compound is soluble in polar organic solvents like dichloromethane or acetonitrile and, to a lesser extent,

in tetrahydrofuran. It is very well soluble in alcohols like methanol or ethanol; however, slow degradation over time is observed. **^{1}H NMR (200.13 MHz, methanol-d_4)**: δ = 1.29 (s, br), 1.44 (s, br), 2.54 (s, br), 3.30 (s,br) ppm. **Evans-NMR (methanol-d_4)**: μ_{eff} = 4.6 μ_B. **Elemental analysis, exp (calc)**: C: 29.57 (29.05), H: 4.84 (4.88), N: 4.50 (4.84), S: 10.81 (11.08) %. **IR (ATR-Diamond)**: υ(SO) = 882 cm^{-1}. **SQUID**: μ_{eff} = 4.9 μ_B (S = 2). **^{57}Fe-Mößbauer**: δ = 0.85 mm·s^{-1} ΔE_Q = 2.95 mm·s^{-1}. **UV-vis**: λ_{max} = 259 nm (sh; ε = 3.78 × 10^3 M^{-1}·cm^{-1}), 355 nm (ε = 3.43 × 10^3 M^{-1}·cm^{-1}). **Melting point**: T$_{smp}$ < 200 °C (decomposition).

[Ni(bmmp-daco)]FeBr$_2$ 2: To a suspension of 120 mg (560 μmol) iron(II) bromide in 20 mL acetonitrile a solution of 200 mg (570 μmol) Ni(bmmp-daco) in 15 mL acetonitrile was added while stirring. The reaction mixture was kept stirring at ambient temperature for two hours and subsequently filtered. After evaporating the solvent, the product was obtained as a red solid (240 mg, 430 μmol, 77% yield). Crystals suitable for single crystal X-ray diffraction were obtained by diffusion of diethyl ether vapor into the filtrated reaction mixture at room temperature. The title compound is soluble in polar organic solvents like dichloromethane or acetonitrile, to a lesser extent, in tetrahydrofuran. It is very well soluble in alcohols like methanol or ethanol; however, slow degradation over time is observed. **^{1}H NMR (200.13 MHz, methanol-d_4)**: δ = 0.95 (s, br), 1.93 (s, br), 2.61 (s, br), 3.33 (s,br) ppm. **Evans-NMR (methanol-d_4)**: μ_{eff} = 4.9 μ_B. **Elemental analysis, exp (calc)**: C: 31.64 (29.86), H: 5.00 (5.01), N: 5.07 (4.98), S:10.90 (11.39) %. **SQUID**: μ_{eff} = 4.9 μ_B (S = 2). **^{57}Fe-Mößbauer**: δ = 0.91 mm·s^{-1} ΔE_Q = 3.10 mm·s^{-1}. **UV-vis**: λ_{max} = 276 nm (ε = 3.86 × 10^3 M^{-1} ·cm^{-1}), 372 nm (ε = 3.43 × 10^3 M^{-1}·cm^{-1}). T$_{smp}$ < 200 °C (decomposition).

Ni(bmmp-daco)$S^{18}O$: The reaction was conducted according to the published procedure for the ^{16}O-compound by Darensbourg *et al*[30] using ^{18}O-labelled H_2O_2 solution (2-3 % in H_2O, 90 atom % labelled) and yielding 200 mg (548 μmol) of ^{18}O-labelled compound (35 % yield). **IR (ATR-Diamond)**: υ(SO) = 897 cm^{-1}. **HR-ESI-MS**: m/z (%) = 365.1120 [Ni$S^{18}O$+H]$^+$ (100); 365.1112 calc. f. [$C_{14}H_{29}N_2Ni^{18}OS_2$]$^+$.

[Ni(bmmp-daco)]$S^{18}O$FeBr$_2$ 3: The reaction was carried out by following the procedure for the ^{16}O-compound. Employing 25 mg (68 μmol) Ni(bmmp-daco)$S^{18}O$ and 15 mg (70 μmol) iron(II) bromide yielded the desired product as a red brown solid (31 mg, 200 μmol, 72 % yield). IR (ATR-Diamond): **IR (ATR-Diamond)**: υ(SO) = 847 cm^{-1}.

5.6.2. ^{1}H-NMR spectroscopy

The ^{1}H NMR spectra were recorded with a Bruker ARX200 spectrometer and referenced using residual solvent signals as internal standards.

5.6.3. UV-vis spectroscopy

UV-vis spectra were recorded using an Analytik Jena Specord S600 spectrometer and the WinAspect 2.3.1.0 software package. Samples for UV-vis spectroscopy were prepared in

a nitrogen filled MBraun glovebox and measured in air-tight sealed cuvettes outside the glovebox.

5.6.4. Single-crystal X-ray structure determination

Crystals were each mounted on a glass capillary in per-fluorinated oil and measured in a cold N_2 flow. The data of **1** and **2** were collected on an Oxford Diffraction Supernova, Single source at offset, Atlas at 150 K (Cu-Kα-radiation, $\lambda = 1.5418$ Å). The structures were solved by direct methods and refined on F^2 with the SHELX-97 software package.[232] The positions of the H atoms were calculated and considered isotropically according to a riding model. CCDC 1515404 (**1**), 1515403 (**2**) contain the supplementary crystallographic data for this paper. These data can be obtained free of charge by contacting The Cambridge Crystallographic Data Centre, 12, Union Road, Cambridge CB2 1EZ, UK; fax: +44 1223336033.

5.6.5. SQUID and ^{57}Mößbauer spectroscopy

Superconducting quantum interference device (SQUID) and ^{57}Mößbauer spectroscopy were performed in the lab of Dr. Eckhard Bill from the Max-Planck Institute for Chemical Energy Conversion in Mühlheim (Ruhr).[140]

Magnetic susceptibility data were measured either from powder samples of solid material or from solution in eicosane (melting point 310 K) in the temperature range 2 - 270 K by using a SQUID susceptometer with a magnetic field strength of 1.0 T (MPMS-7, Quantum Design, calibrated with a standard palladium reference sample, error <2%). Multiple-field variable-temperature magnetization measurements were carried out at 1 T, 4 T, and 7 T in the range 2 - 260 K with the magnetization equidistantly sampled on a 1/T temperature scale. Sample holders of quartz with O-ring sealing were used and the SQUID response curves (raw data) were corrected for holder and solvent contributions by subtracting the corresponding response curves obtained from separate measurements without sample material. The experimental magnetization data obtained from independent simulations of the corrected SQUID response curves were corrected for underlying diamagnetism[12] by use of tabulated Pascal's constants,[173,268] as well as for temperature-independent paramagnetism. Handling and simulation of the SQUID raw data as well as spin-Hamiltonian simulations of the susceptibility and magnetization data were performed using our own package julX for exchange-coupled systems (available from Eckhard Bill by mail to ebill@gwdg.de). The simulations were based on the usual spin-Hamiltonian operator for mononuclear complexes with spin S = 2:

$$\hat{H}_S = D\Big[\hat{S}_z^2 - \frac{1}{3}S(S+1) + \frac{E}{D}(\hat{S}_x^2 - \hat{S}_y^2)\Big] + \mu_B \overrightarrow{B} \cdot g \cdot \overrightarrow{\hat{S}} \tag{5.1}$$

where g is the average electronic g value, while D and E/D are the axial zero-field splitting and rhombicity parameters, respectively.

Diagonalization of the total Hamiltonian was performed with the routine ZHEEV from the LAPACK Library (available from Eckhard Bill), and magnetic moments were calculated from the eigenfunctions by using the Hellman-Feynman theorem:

$$\overrightarrow{\mu_i}(\overrightarrow{B}) = -\langle\Psi_i|\frac{d\hat{H}}{d\overrightarrow{B}}|\Psi_i\rangle \tag{5.2}$$

The powder summations were performed by using a 16-point Lebedev grid (a Fortran code to generate Lebedev grids up to order L=131 is available from: http://server.ccl.net /cca/software/SOURCES/FORTRAN/Lebedev-Laikov-Grids/).[133]

Mößbauer spectra were recorded on a conventional spectrometer with alternating constant acceleration of the γ-source (^{57}Co/Rh, 1.8 GBq), which was kept at room temperature. The minimum experimental line width was 0.24 mm·s^{-1} (full width at half-height). The sample temperature was maintained constant at 80 K in an Oxford Instruments Variox cryostat. Isomer shifts are quoted relative to iron metal at 300 K.

5.7. Molybdenum model complex

The synthetic design and work was performed by Ricardo Nowack from the group of Carola Schulzke from the Universität Greifswald.

Unless otherwise stated, all experiments were carried out under dry oxygen-free nitrogen using standard Schlenk techniques. Solvents were dried by standard methods and freshly distilled prior to use. Synthesis of 4,5-dimethyl-1,3-dithiol-2-one (dmdt) were prepared according to procedures reported in the literature.[18,38] Synthetic fabrication of metal and molybdenum precursors were performed as stated elsewhere.[74,139,149,226–228]

MoS(dmdt)$_2$: 60 mg (154,48 μmol) of the Mo(CO)$_2$(dmdt)$_2$ precursor are solved in 20 mL acetonitrile applying Schlenk techniques. While stirring, 33,8 mg (433,08 μmol) of pestled Na_2S was added and further stirred for 3 h at room temperature. Afterwards, the suspension is filtered using a syringe and an injection filter ($\varnothing$ = 0.2 μm). The remaining brown mother liquor is anaerobically transferred into a Schlenk flask, followed by a recrystallization in ether. The product crystallizes as black-blue needles.[39] **IR (KBR)**: υ: = 2904 cm^{-1}, 1627 cm^{-1}, 1523 cm^{-1}, 1438 cm^{-1}, 933 cm^{-1}.

5.8. Vibrational methods

5.8.1. Infrared spectroscopy

Transmission

IR spectra of 0.3 mM solutions of as-isolated and chemically reduced *Ht*SH and of FDH from *Rhodobacter capsulatus* recorded with a spectral resolution of 2 cm^{-1} using a Bruker Tensor 27 FTIR spectrometer, equipped with a liquid nitrogen-cooled MCT detector. The

sample compartment was purged with dry air, and the sample was held in a temperature-controlled (10 °C) gastight IR transmission cell for liquid samples (volume: 10 μL, optical path length: 50 μm), equipped with CaF_2 windows. 200 scans were accumulated per single channel spectrum, and absorbance spectra were calculated by the Beer-Lambert law, usually, from an average of each 20 sample- and background single channel spectra. Spectra analysis were performed using the Bruker OPUS software 5.5 or higher and baseline correction, if necessary, was carried out using Qpipsi (self-written).

IR spectra for all synthetic [NiFe] complexes were measured from powder samples inside a nitrogen filled glovebox using a Thermofisher Nicolet iS5 IR Spectrometer (ATR-Diamond) and the OMNIC software (Version 9.3.30) for data acquisition.

IR spectro-electrochemical measurements

IR spectro-electrochemical experiments were performed on ca. 0.3 mM solutions of *Ht*SH, activated anaerobically with 2 mM TCEP, using an Optically Transparent Thin Layer Electrochemical (OTTLE) cell with an optical path length below 10 μm.[161] In order to avoid protein adsorption, the gold mesh working electrode was incubated anaerobically with a mixed self-assembling monolayer of 1 mM cysteamine and 1 mM mercaptopropionic acid, solved in ethanol, for 30 min. Preparation of the OTTLE cell was performed anaerobically in an Ar-filled box. The following redox mediators were added to the protein solution in order to ensure fast equilibration at the applied potentials (0.5 mM each, potential vs. SHE): TMPPO (+262 mV), 1,2-naphthoquinone (+145 mV), 1,4-naphthoquinone (+60 mV), methylene blue (+11 mV), indigo trisulfate (-80 mV), indigo disulfate (-130 mV), 2-hydroxy-1,2-naphthoquinone (-139 mV), resorufin (-195 mV), anthraquinone-2-sulfonate (-225 mV), safranin T (-290 mV), benzyl viologen (-358 mV), methyl viologen (-446 mV).[52,62,161] Potential-dependent IR spectra with a resolution of 2 cm^{-1} were recorded at 30 Â°C using a Bruker IFS 66 v/s FTIR spectrometer equipped with a liquid nitrogen-cooled MCT detector. The Bruker OPUS software, version 5.5 or higher, was used for data acquisition and evaluation. Potential control was accomplished using a Model 263A Potentiostat (Princteon Applied Science) and the PARControl 1.05 software. Samples were equilibrated at all potentials for at least 3 min until the corresponding IR spectrum remained unchanged.

5.8.2. Resonance Raman spectroscopy

Resonance Raman spectra were recorded using the 514 nm emission of an Argon ion laser (Innova 70, Coherent) for excitation and a confocal Raman spectrometer (Lab Ram HR-800 Jobin Yvon) equipped with a liquid-nitrogen cooled charge coupled device (CCD) camera for data acquisition. The typical laser power at the sample ranged between 0.2-0.5 mW for synthethic complexes and between 1-5 mW for proteinogenic samples. The inorganic complexes were measured as dry powders and enzymes in frozen liquid solution using a Linkam Cryostage THMS600 cryostat. The temperature of the samples was kept

at 80 K throughout the measurements. The spectrometer was calibrated before each experiment using toluene as external standard.

5.9. Electron paramagnetic resonance spectroscopy

EPR spectroscopy was carried out by Christian Lorrent from the group of Prof. Dr. Peter Hildebrandt of the Technische Universität Berlin. A Bruker EMXplus spectrometer equipped with an ER 4122 SHQE resonators and an Oxford EPR 900 helium flow cryostat with temperature control (Oxford ITC4) between 5 and 310 K was used in the experiments. Spectra were baseline-corrected by subtracting a background spectrum obtained from buffer solution using the same experimental parameters. Experimental conditions: 1 mW microwave power, microwave frequency: 9.29 GHz, 1 mT modulation amplitude, 100 kHz modulation frequency. Spectra simulations were performed using the MATLAB toolbox EasySpin (version 5.1.7).[242]

5.10. Nuclear resonance vibrational spectroscopy

Nuclear resonance vibrational spectroscopy (NRVS) were peformed by Dr. Lars Lauterbach from the group of Dr. Oliver Lenz of the Technische Universität Berlin. Therefore, *R. eutropha* HF1054 (pJP09) was cultured as described above, with the exception that 18 μM $^{57}FeCl_2$ instead of $^{56}FeCl_2$ was used as the iron source. The resulting ^{57}Fe-labelled *Ht*SH was purified via *Strep*-Tactin affinity chromatography. NRVS was performed at SPring-8 BL09XU with a 0.8 meV (6.5 cm^{-1}) energy resolution at 14.4125 keV as described previously.[132] The beam size at BL09XU was 1.1 mm (horizontal) × 0.6 mm (vertical). A 4-element avalanche photo diode detector array was used to measure delayed K shell fluorescence and nuclear fluorescence by ^{57}Fe atoms. All measurements were performed in the cryostat base that was cooled to 10 K. The real sample temperature was 30-60 K, as obtained from the spectral analysis. The raw NRVS data was converted to a ^{57}Fe partial vibrational density of states (PVDOS) by the PHOENIX software, while the energy scale was calibrated with an external reference ($[NEt_4][FeCl_4]$).[244] For the *Ht*SH protein sample (22 μL, 0.8 mM), the accumulation time was 21 h.

5.11. DFT

5.11.1. DFT calculations of [NiFe]-hydrogenase model complexes

In case of the synthetic [NiFe] model complexes calculations were performed by Dr. Tibor Szilvási from the Department of Chemical and Biological Engineering of the University of Wisconsin. Computational analysis was carried out using the B3LYP functional.[15,134,264] The Def2-TZVP basis set was employed for all atoms, with the corresponding pseudopotential for heavy elements, except for C and H, for which the Def2-SVP basis set was

applied.[270] Analysis of the electronic structure occurred at same level of theory. Optimized minimum structures were confirmed by frequency calculations, not yielding any imaginary frequencies. All calculations were performed with Gaussian 09 Revision B.01.[66]

5.11.2. DFT calculations of different Molybdenum cofactors

The DFT claculations described in chapter 6.3 were performed by Dennis Belger and Prof. Dr. Maria Andrea Mroginski from the Technische Universität Berlin.

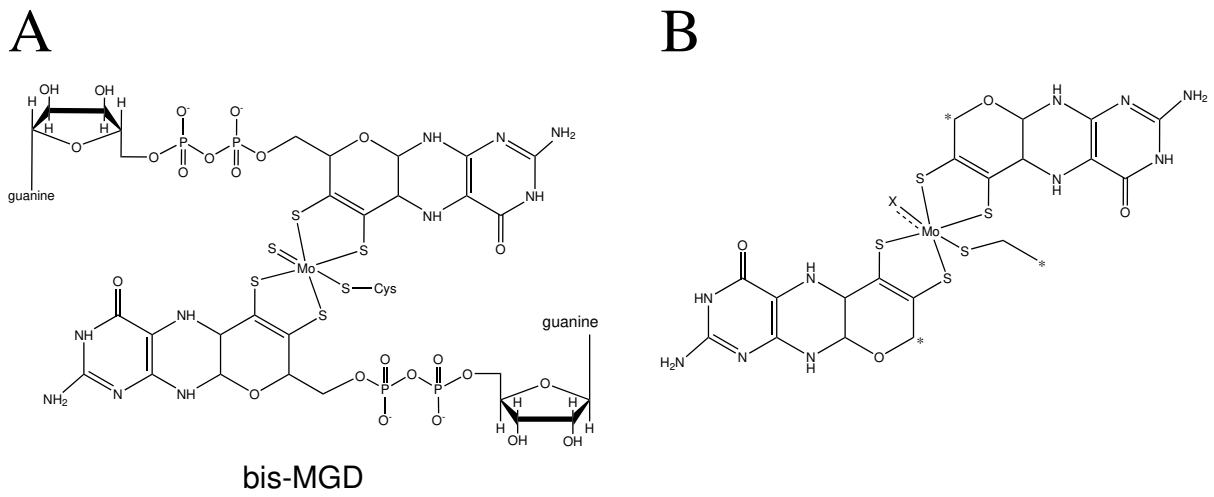

Figure 5.1. **A** The Molybdenum cofactor as reported for *Rhodobacter capsulatus* and **B** the Moco model strucuture used in the DFT calculations. The asterisks display a replacement of the organic side chains by hydrogen atoms. The X describes either a S, SH, OH or O ligand. For the sake of clarity, Molybdenum oxidation numbers are omitted.

Since the complete Moco is very large and demands high computational resources, not the entire Moco was applied in the model calculations. If not stated otherwise all models were built computed in the following: Mo^{6+}: Cysteine coordinated to the metal and O, OH, S or SH as last ligand. In the $Mo^{4+;5+}$ models either no cysteine or a protonated cysteine was present and O, OH, S or SH ligated. The models are named $Mo^{6+;5+;4+}$-X, were X represents OH or SH and $Mo^{6+;5+;4+}$=X were X symbolizes O or S, respectively. The 5'-guanosine-diphospahte units were omitted due to named computational reasons. Dithiolene ligands, as well as the opterine parts were included. All atoms were treated explicitly, while the Cys386 was mimicked by a truncated version. Here, the terminal C_β is saturated by protons and was fixed (to simulate the lesser degrees of freedom of the amino acid in the protein matrix). Additionally, every other truncation spot was selected as fixed to assign sterical hindrance according to the realistic situation in the enzymatic binding pocket. The charges were selected as follows: the Mo ion either (+VI), (+V) or (+IV), deprotonated Cys (-I), O/S (-II), OH/SH (-I) and the individual dithiolene moieties (-II). Multiplicity of the complex was always singlet (doubly occupied molecular

orbitals). The protein environment was mimicked by application of a dielectric field constant of $\varepsilon = 4$ by means of the polarizable continuum model.[250] The optimizations followed the standard self-consisting field procedures from Gaussian[66], using DFT with the BP86 functional and a 6-31G* basis set for C, H, N atoms[185] and def2-TVPP basis sets for S and Mo.[270] Furthermore, effective core potentials[91] at the same level were applied to the metal atom. Subsequently, the frequencies and Raman intensities were computed using the normal mode analysis approach as described elsewhere[235] and was carried out in internal coordinates as provided by the Gaussian program.

Based on the same model as mentioned above, the calculations of the azide inhibition were performed. Here, the latter replaces the cysteine in the computation of a direct bond between the N_3^- molecule with the Mo ion. In case of a non-covalent binding, the Mo ion is hexa-coordinated by two dithiolene units, a cysteine as well as the sulfido ligand. The azide is located in close proximity to the metal center by means of electrostatic interactions.

6. Results and Discussion

6.1. [NiFe]-hydrogenase

Following passages are published with kind permission from Elsevier.[197]

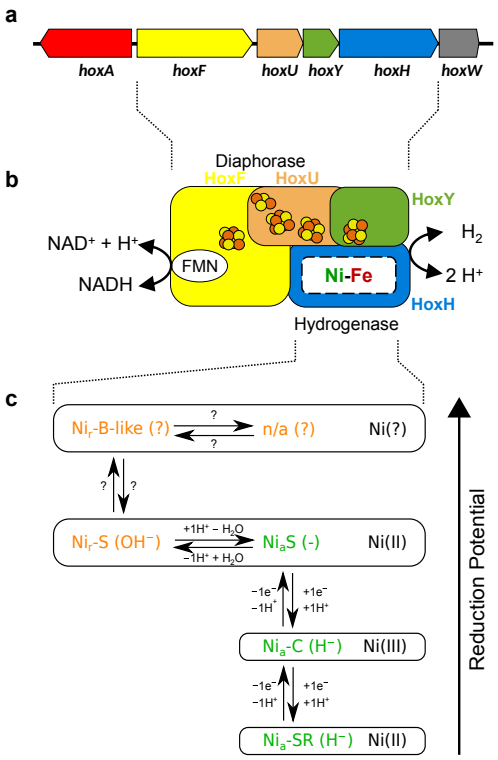

Figure 6.1. Arrangement of the *Ht*SH-related genes (**a**), proposed subunit/cofactor composition (**b**), and observed active site redox states of *Ht*SH (**c**). Genes *hoxF*, *U*, *Y*, and *H* encode the subunits of the SH protein, while *hoxA* has presumably a regulatory function. Upon insertion of the [NiFe] active site, the *hoxW* gene product mediates cleavage of a C-terminal extension of the HoxH subunit. The proposed cofactor composition in **b** is derived from amino acid sequence comparisons with the corresponding subunits of *Re*SH and Complex I from *Thermus thermophilus* (see Appendix, Fig. A.1-A.5) and analogies to the well-characterized *Re*SH. The assignment of active site species and their interconversions shown in **c** is based on IR and EPR spectroscopic analyses (see below). Redox states highlighted in green belong to the catalytic conversion of H_2, while the orange ones represent inactive states that except for Ni_r-S require reductive treatment to be converted into the Ni_a-S state. The unassigned oxidized state labelled with n/a is unprecedented (see below).

As stated earlier the biochemical analysis was carried out by Dr. Janina Preissler from the group of Dr. Oliver Lenz. For biotechnological applications oxygen-tolerant [NiFe]-hydrogenases are of particular interest due to their ability to convert hydrogen under aerobic conditions. This study aimed to gain insights into a thermostable version of a soluble hydrogenase. Therefore, the draft sequence of the *H. thermoluteolus* TH-1^T genome was analyzed and revealed the *Ht*SH-related genes, *hoxF*, *hoxU*, *hoxY*, *hoxH*, and *hoxW*, which are apparently arranged as an operon (see Fig. 6.1 **a**).

Pairwise alignments of *Ht*SH and *Re*SH proteins revealed 40%, 37%, 44%, 46%, and 26% identical residues for HoxF, HoxU, HoxY, HoxH, and HoxW, respectively. Notably, the *H. thermoluteolus* TH-1^T genome does not contain a copy of the gene encoding the HoxI protein, which is a constituent of the *Re*SH.[32]

6.1.1. Heterologous overproduction and purification of functional *Ht*SH

For heterologous overproduction of the *Ht*SH in *R. eutropha* and subsequent purification, the *hoxFUYHW* genes were amplified by PCR and put under the control of the native SH promoter of *R. eutropha* as described in chapter 5.1. Furthermore, a sequence encoding the *Strep*-tag II peptide was attached to the 5' end of the *hoxF* gene. The resulting synthetic $hox_{strep}FUYHW$ operon was inserted into the broadhost range vector pEDY309 resulting in plasmid pJP09, encoding *Strep*-tagged *Ht*SH.

Table 6.1. Purification of *Ht*SH protein enzyme by affinity chromatography.

Fraction[a]	Volume (mL)	Protein concentration (mg/mL)	Total protein (mg)	Specific activity (U·mg^{-1})[b]	Total activity (U)	Yield (%)	Enrichment factor
SE	40	29.2	1168	2.5 ± 0.1	2920	100	1
AC	1.4	29.7	41.6	12.1 ± 0.1	502	17	4.8
SEC	2.4	4.9	11.7	33.4 ± 0.6	391	13	13.4

[a] The *Ht*SH protein was purified from soluble cell extracts (SE) by *Strep*-Tactin affinity chromatography (AC) and subsequent size exclusion chromatography (SEC) as described in chapter 5.1.

[b] Activity was determined by H_2-dependent NAD^+ reduction in 50 mM bis-Tris, pH 6.5, supplemented with 1 mM NAD^+, 0.5 mM $NiCl_2$, 5 mM $MgSO_4$, 2 μM FMN, and 0.75 mM TCEP at a temperature of 50 °C. One Unit (U) corresponds to the amount of converted substrate (in μmol) in 1 min. Values of a representative purification are shown.

For enzyme purification, plasmid pJP09 was transferred into strain *R. eutropha* HF1054, in which the native *hoxFUYHWI* genes as well as *hoxG* encoding the large subunit of the membrane-bound [NiFe]-hydrogenases were eliminated by isogenic in-frame deletions. This prevented any "subunit mixing" between *Ht*SH and *Re*SH proteins. The transconjugant strain *R. eutropha* HF1054 (pJP09) was cultivated heterotrophically under oxygen-limited conditions as described previously.[75,129] In a first experiment, the H_2-driven NAD^+ reduction activity was measured in soluble extract of the recombinant cells. The activity was 2.50 ± 0.12 U·mg^{-1} of protein (Table 6.1), suggesting the presence of functional *Ht*SH proteins. This result also demonstrates that the general [NiFe]-hydrogenase maturation

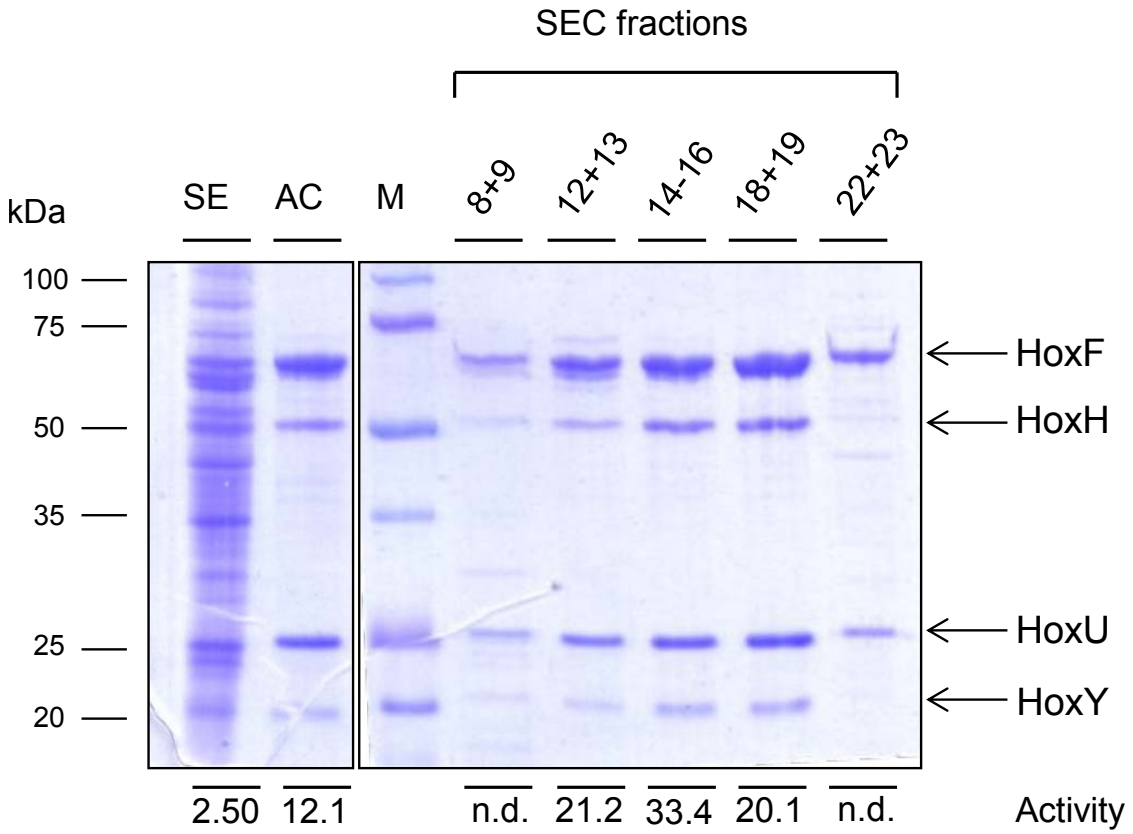

Figure 6.2. Purification of the *Ht*SH protein. A protein amount of 30 μg of soluble extract (SE) and 5 μg of *Ht*SH purified by affinity chromatography (AC) and selected fractions (from the subsequent size exclusion chromatography (SEC) were electrophoretically separated on a 12% SDS-polyacrylamide gel and subsequently stained with Coomassie brilliant blue. The specific H_2-driven NAD^+ reduction activity ($U \cdot mg^{-1}$ of protein) of each fraction is specified below. Lane M contains marker proteins and their corresponding molecular weights are given on the left hand side.

machinery of *R. eutropha* is able to synthesize and to deliver the active site constituents for the HoxH subunit of *Ht*SH.[33,54,276] The *Ht*SH protein was then purified to homogeneity by *Strep*-Tactin affinity and size exclusion chromatography as described in chapter 5.1. From 10 g (wet weight) of cells, we routinely obtained 10-12 mg of protein with a specific H_2-driven NAD^+ reduction activity of 33.4 $U \cdot mg^{-1}$ of protein (measured at 50 °C, Table 6.1). Please note, the enzymatic hydrogenase activity (in $U \cdot mg^{-1}$) varied between individual protein batches between 16 and 36 $U \cdot mg^{-1}$ (see Fig. 6.5 and Tab. 6.3). The reverse reaction, namely NADH-driven H_2 production, was catalyzed with an activity of 1.0 ± 0.3 $U \cdot mg^{-1}$ of protein. Using dithionite-reduced methyl viologen (MV) as artificial, low-potential electron donor, the H_2 production activity increased to 30 ± 5 $\cdot mg^{-1}$ of protein. SDS-PAGE performed with the *Ht*SH preparation revealed four protein bands assigned to the subunits HoxFUHY (Fig. 6.2).

6.1.2. Biochemical characterization of purified *Ht*SH

Based on visual inspection of the protein bands after electrophoretic separation (Fig. 6.2), a ratio of approximately 1:1 of the two SH modules, HoxFU and HoxYH, was obtained only when Ni^{2+} (0.5 mM) and Mg^{2+} (5 mM) ions were present during the whole purification process. A similar observation has been made previously for the NAD^+-reducing [NiFe]-hydrogenase from *Rhodococcus opacus*.[224] Consequently, the following activity assays were conducted in the presence of Ni^{2+} and Mg^{2+} ions in addition to 2 μM FMN, the latter of which led to a shortened lag phase but did not change the maximal H_2 oxidation activity (Fig. A.6). This suggests that FMN serves as an electron acceptor, and reduced FMN can reactivate those inactive *Ht*SH species which cannot be activated by H_2 alone. This mechanism is similar to the NADH-based reactivation of as-isolated *Re*SH.[32,220]

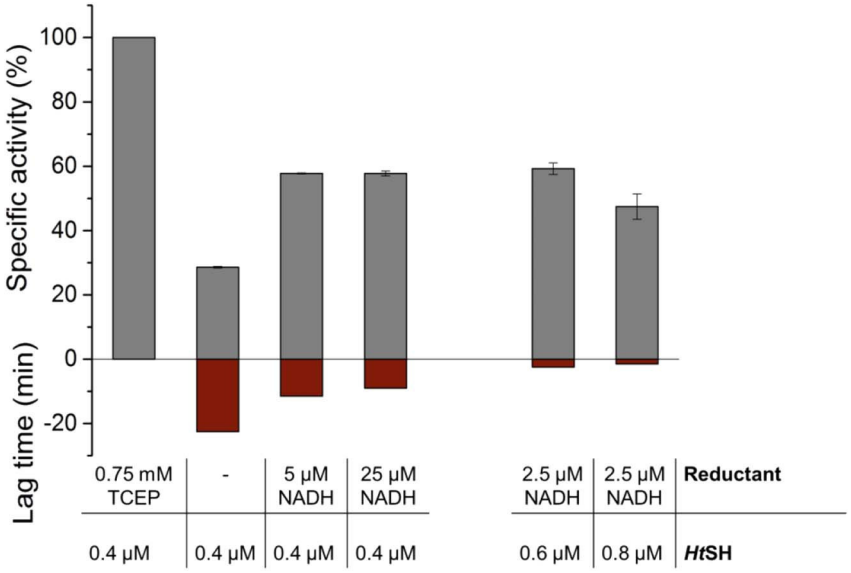

Figure 6.3. Dependence of H_2-dependent NAD^+ reduction activity of purified *Ht*SH protein on the addition of reductants TCEP and NADH. The assay was performed at 50 °C in 50 mM bis-Tris, pH 6.5, supplemented with 1 mM NAD^+, 0.5 mM $NiCl_2$, 5 mM $MgSO_4$, 2 μM FMN, and varying amounts of TCEP, NADH and *Ht*SH. The lag time refers to the time elapsed from assay start until full activity was achieved. 100% activity refers to 19 $U \cdot mg^{-1}$ of protein.

Highest H_2-driven NAD^+ reduction activity for purified *Ht*SH (Fig. 6.3), however, was observed when the reductant TCEP (0.75 mM) was added in addition to FMN. Activity was maximal after a lag period of ca. 2.5 min. The removal of just TCEP led to a dramatic increase of the lag time (ca. 25 min), and the activity dropped to 25% of the value measured in the presence of TCEP (Fig. 6.3). The negative effect of the missing TCEP could be partly compensated through addition of catalytic amounts of NADH (5 μM), which led to the recovery of approx. 50% of the maximal activity and a halved lag phase (Fig. 6.3). This indicates that NADH supports reductive reactivation of aerobically

purified *Ht*SH as previously observed for SH from *R. eutropha*.[32,220] A considerable further shortening of the lag phase was accomplished by increasing the protein concentration in the assay. In the presence of 0.8 μM *Ht*SH and only 2.5 μM NADH, it took only 4 min until full activity was developed (Fig. 6.3). This suggests that the rate of reductive reactivation can also be accelerated by intermolecular electron transfer between individual *Ht*SH enzymes. The likelihood of electron exchange between *Ht*SH enzymes is of course greater at higher protein concentration.

Based on the knowledge derived from the experiments described above, $NiCl_2$, $MgSO_4$, FMN, and TCEP were added to the following activity assays, unless stated otherwise. Using this standard protocol at a fixed temperature of 50 °C, we first determined the H_2-dependent NAD^+ reduction activity of purified *Ht*SH at different pH values. This was accomplished with a universal buffer that spanned the entire pH range from pH 4.5-9 (Fig. 6.4) as well as with three buffers with different pH ranges (Fig. A.7).

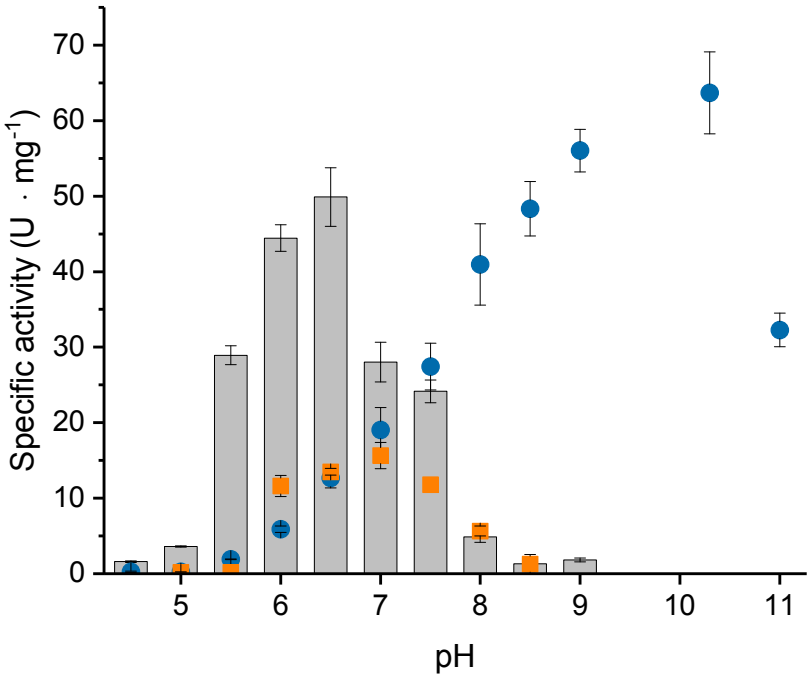

Figure 6.4. Activity of purified *Ht*SH protein at different pH values. The graph depicts the H_2-dependent NAD^+ reduction activities of *Ht*SH (grey bars) as well as the H_2:benzyl viologen (orange symbols) and NADH:benzyl viologen (blue symbols) oxidoreductase activities of the individual *Ht*SH modules. The measurements were performed as described in chapter 5.1 with 45 nM of *Ht*SH in an universal buffer composed of 16 mM citrate, 16 mM Tris, and 16 mM glycine. Activities were measured at a temperature of 50 °C in the presence of either of 1 mM NAD^+, 1 mM NADH, or 5 mM benzyl viologen, additionally to 0.5 mM $NiCl_2$, 5 mM $MgSO_4$, 2 μM FMN, and 0.75 mM TCEP.

From both experiments, an optimum pH of 6.5 was derived. This is in marked contrast to *Re*SH that performs best at pH 8.0[202,220] (Table 6.2), where the *H. thermoluteolus* enzyme showed only about 10% of the maximal H_2-driven NAD^+ reduction activity of 50 ± 4 U mg^{-1} of protein (measured at pH 6.5, Fig. 6.4). In order to elucidate the origin of the unusual pH optimum, the enzymatic reactions of the two SH modules were tested separately in a pH-dependent manner (Fig. 6.4). First, the HoxFU-catalyzed NADH:-benzyl viologen oxidoreductase activity was measured as described in chapter 5.1. Maximum activity of 64 ± 5 U mg^{-1} of protein was reached at approximately pH 10, which is qualitatively consistent with the observations made previously for the HoxFU module of the *Re*SH.[130] The H_2:benzyl viologen oxidoreductase activity of the HoxHY module, however, was found to be optimal at approximately pH 7.0. These results indicate that the pH optimum of the *Ht*SH is primarily dictated by the intrinsic bias of the H_2/H^+-cycling module of the holoenzyme.

Table 6.2. Comparison of soluble, $NAD(P)^+$-reducing [NiFe]-hydrogenases.[a]

Organism	*H. thermoluteolus* TH-1^T	*R. eutropha* H16	*Synechocystis* sp. PCC 6803	*Pyrococcus furiosus*
Designation	SH	SH	Bidirectional hydrogenase	SH1
Subunit composition	HoxHYFU	$HoxHYFUI_2$[32]	HoxHYFUE[219]	$\alpha\delta\beta\gamma$[148]
Molecular weight (kDa)	168	207[32]	180[219]	153[148]
K_M H_2 (μM)	42	37[220]	11.3[231b]	140[148]
Physiological electron acceptors/donors	NAD^+	NAD^+	NAD(P)+/NAD(P)H, $ferredoxin_{red}$, $flavodoxin_{red}$[45,46]	$NAD(P)^+$
K_M $NAD(P)^+$ (μM)	469 (NAD^+)	560 (NAD^+)[220]	n.p.	40 ($NADP^+$)[148]
k_{cat} for H_2-driven $NAD(P)^+$ reduction (s^{-1})	150 s^{-1}	485 s^{-1}[254]	n.p.	99 s^{-1} (NAD^+)[148] 38-89 s^{-1} ($NADP^+$)[40]
v_{max} for NAD(P)H-driven H_2 production	0.9 U mg^{-1}	1.2 U mg^{-1}	2.81 U mg^{-1}[219]	1.5-2 U mg^{-1} (NADPH)
T_{opt}	80 °C	35 °C[202]	60 °C[219]	80 °C[28,147]
pH_{opt}	6.5	8[202,220]	6.3[219]	8.4[147]
Behavior towards O_2	Moderately O_2-tolerant ~50% H_2-dependent NAD^+ reduction activity[c] in the presence of 19 μM O_2	O_2-tolerant, ~85% H_2-dependent NAD^+ reduction activity[c] in the presence of 470 μM O_2[129]	O_2-sensitive, no catalytic activity in the presence of O_2; can be rapidly reactivated under reducing conditions[71]	Moderately O_2-tolerant, ~25% of H_2 oxidation activity[d] in the presence of 14 μM O_2[125]

n.p. not published.
[a] Note that values are only limitedly comparable since the assay conditions were not identical.
[b] Value has been determined for the bidirectional hydrogenase from the *Synechocystis* sp. relative, *Anabaena variabilis*.
[c] Compared to the activity measured in the absence of O_2. Activities were measured spectrophotometrically in solution.
[d] Compared to the activity measured in the absence of O_2. Activities were measured electrochemically with immobilized enzyme at oxidizing potential.

Measurements of the H_2-dependent NAD^+ reduction activity of purified *Ht*SH at different temperatures were performed in bis-Tris buffer at pH 6.5 and revealed a maximal activity of 71.0 ± 0.3 U mg^{-1} of protein at a temperature of 80 °C (Fig. 6.5). This is in sharp contrast to *Re*SH, which quickly loses activity at temperatures higher than

35 °C (Table 6.2).[202] At 33 °C, which is the temperature optimum of *Re*SH activity, *Ht*SH showed less than 20% of the maximal activity.[220]

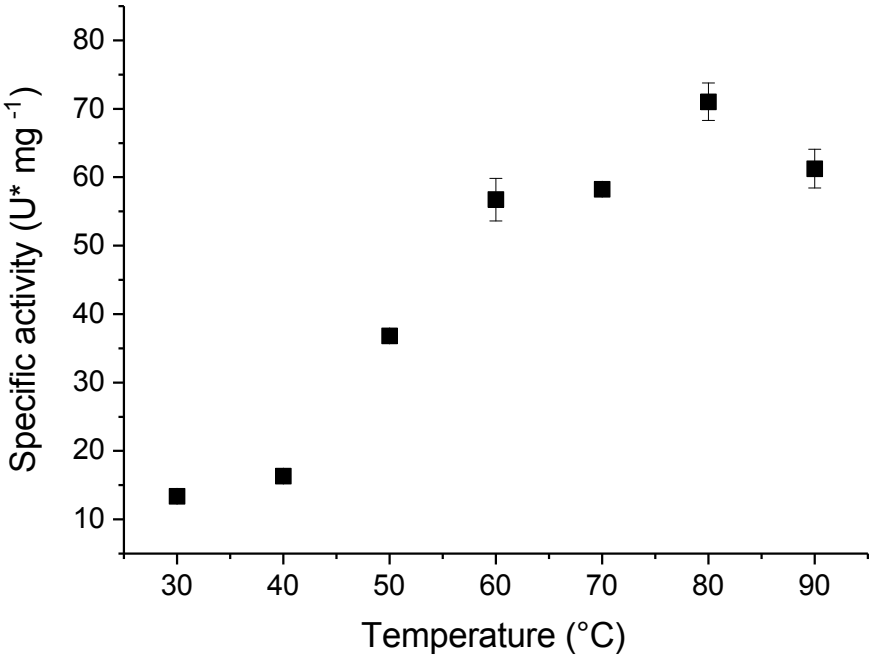

Figure 6.5. Temperature dependence of the H_2-dependent NAD^+ reduction activity of purified *Ht*SH protein. The measurements were performed as described in chapter 5.1 with 45 nM of *Ht*SH in 50 mM bis-Tris buffer, pH 6.5, containing 1 mM NAD^+, 0.5 mM $NiCl_2$, 5 mM $MgSO_4$, 2 μM FMN, and 0.75 mM TCEP. If the error bars are not visible, they are equal or smaller than the symbol size.

In a next series of experiments, we determined the Michaelis-Menten constants (K_M) for the natural substrates of the *Ht*SH. The K_M value for NAD^+ was evaluated based on the H_2-driven NAD^+ reduction activity of the enzyme and revealed to lie at 469 μM (Fig. A.8) which is close to 560 μM, the value determined for *Re*SH.[220] Activity measurements of the *Ht*SH-mediated benzyl viologen reduction activity in the presence of various NADH concentrations resulted in a ${K_M}^{NADH}$ of 1.2 mM (Fig. A.9), which is surprisingly high when compared to the corresponding value of 80 μM determined for the *Re*SH.[220] This suggests that the main physiological role of *Ht*SH enzyme is H_2-driven NAD^+ reduction.

A value of 42 $\pm$ 3 μM was determined for the apparent Michaelis-Menten constant, ${K_M}^{app}$, for H_2 during H_2-driven NAD^+ reduction of the enzyme (Fig. A.10), which is comparable to that measured for *Re*SH (37 μM,[220] Table 6.2).

6.1.3. Cofactor content and oxygen tolerance of *Ht*SH

Fluorescence determination revealed 1.07 FMN per SH tetramer. Using inductively coupled plasma optical emission spectrometry, 14.2 ± 0.2 Fe and 2.4 ± 0.1 Ni per SH molecule were detected. On the basis of conserved amino acid residues that are involved in Fe-S cluster coordination in Complex I, 19 iron atoms are expected in addition to one nickel in the catalytic center of the hydrogenase module (Fig. 6.1, A.1-A.5). Additional information on the type of iron-sulfur clusters present in *Ht*SH was obtained by nuclear resonance vibrational spectroscopy (NRVS). NRVS is a synchrotron-based vibrational spectroscopic technique that selectively probes iron-specific normal modes and has been shown to provide details on [NiFe]-hydrogenase cofactor structure and composition.[132,176] The partial vibrational density of states (PVDOS) for oxidized *Ht*SH is presented in Fig. A.12. The band at 414 cm^{-1} is characteristic for the presence of a [2Fe2S] cluster, which is supposed to be coordinated by the HoxU subunit.[279] Of the 19 irons in *Ht*SH, 16 are expected to be constituents of [4Fe4S] clusters. Indeed, also the spectral pattern between 0 and 400 cm^{-1} is very similar to that of *Re*SH and a [4Fe4S] cluster-containing ferredoxin (Fig. A.12), which indicates dominant contributions of [4Fe4S] cluster species.[132,159] Thus, these results support the presence of four [4Fe4S] clusters and one [2Fe2S] species in *Ht*SH.

Table 6.3. H_2-driven NAD^+ reduction activity of the *Ht*SH protein[a] in the presence of various O_2 concentrations.

$O_2/H_2/N_2$ fractions[b] (% v/v)	$[O_2]$ (μM)	Hydrogenase activity in the presence of O_2 (U mg^{-1} of protein)[c]	k_{cat} (s^{-1})	Hydrogenase activity (%)
0/33.33/66.66	0.00	16 ± 2	45.9	100
0.2/33.33/66.46	1,9	15 ± 4	43.0	94.2
2/33.33/64.66	18,8	7.7 ± 0.3	21.5	49.8
10/33.33/56.66	94,0	1.3 ± 0.5	3.6	8

[a] *Ht*SH was purified by affinity chromatography as described in chapter 5.1.
[b] For each O_2 concentration, a fixed volume of H_2-saturated buffer was mixed with various proportions of O_2- and N_2-saturated buffers. The gas phase contained the corresponding gas mixtures.
[c] H_2-mediated NAD^+ reduction activity was measured at 50 °C and pH 6.5.

Consistent with the chemolithoautotrophic growth capacity of the host organism under aerobic conditions, the isolated *Ht*SH showed sustained H_2-driven NAD^+ reduction activity in the presence of O_2 (Table 6.3). However, its O_2 tolerance revealed to be lower than that of the *Re*SH (Table 6.2, Table 6.3). While the *Re*SH preserves approximately 100% activity observed at 20% O_2 (measured at 30 °C in Tris/HCl buffer, pH 8)[129,221],

the *Ht* enzyme showed at 10% O_2 less than 20% of the activity measured in the absence of O_2. At 2% O_2, it displayed only 50% of the activity observed under anaerobic conditions. However, at low O_2 pressure (0.2%), *Ht*SH activity remained at almost 100% (Table 6.3). In this respect, it is noteworthy that the intracellular O_2 concentration in living cells is generally much lower than the external one. This explains why *H. thermoluteolus* cells grow well with H_2 and CO_2 even at ambient O_2 concentrations, although the isolated enzyme is more O_2 sensitive than the SH from *R. eutropha*.

6.1.4. Spectroscopic characterization of *Ht*SH

To gain insight into structure and function of the metal cofactors, in particular of the [NiFe] active site, *Ht*SH samples treated with different redox agents were characterized by IR and EPR spectroscopy. For both types of spectroscopic measurements, samples were prepared under identical conditions to guarantee comparability of the results. In addition, IR spectro-electrochemical experiments were performed to provide insight into equilibria between the individual redox states of the [NiFe] active site with characteristic band positions for the two cyanide and one CO ligands coordinated to the Fe ion. All IR data are displayed as second derivative spectra where the maximum of an absorption band appears as a sharp negative peak. Peak positions derived from IR and EPR spectroscopy as well as their assignment to individual cofactors and redox states are summarized in Table 6.4. In the following the focus will emphasize on a redox state allocation via the band positions of the CO ligand. The corresponding CN stretchings will be assigned latter on.

Table 6.4. CO and CN stretching frequencies (cm^{-1}) of IR-spectroscopically observed *Ht*SH [NiFe] active site species and corresponding g-values of cofactor species detected by EPR spectroscopy.

Assignment	υ(CO)	υ(CN)		g_1	g_2	g_3
n/a[a]	1993	2081	2090	2.260	2.127	2.034
Ni_r-B-like	1964	2087	2098			
Ni_r-S	1936	2058	2071			
Ni_a-S	1951	2076	2089			
Ni_a-C	1971	2076	2089	2.210	2.139	2.013
Ni_a-SR	1958	2062	2076			
Ni_a-SR'	1943	2048	2062			
Ni_a-SR"	1934	2048	2062			
[3Fe4S]				2.004	1.982	
[2Fe2S]				2.026	1.935	
FMN				2.003		

[a] Not assigned. Oxidized active site species of unknown structure.

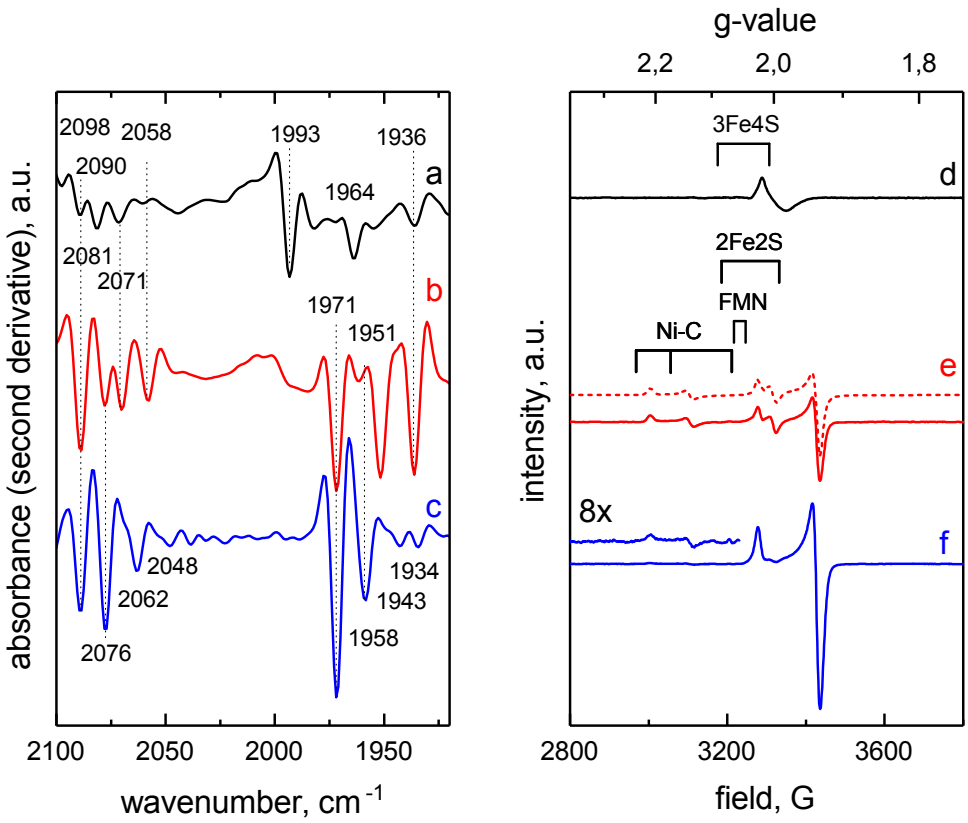

Figure 6.6. IR (left) and EPR (right) spectra of *Ht*SH recorded under different redox conditions. Samples were prepared as described in chapter 5.1 and measured in the as-isolated, oxidized state (black spectra) or in their reduced states (red spectra: samples reduced with TCEP and NADH; blue spectra: samples reduced with TCEP, NADH, and H_2). IR spectra were acquired at 10 °C, while EPR spectra were recorded at either 10 K (d) or 35 K (e, f).

IR spectra of as-isolated *Ht*SH exhibit up to three distinct bands at 1993, 1964, and 1936 cm^{-1} (Fig. 6.6, trace a). Signals in this spectral region are generally associated with the stretching vibration of the intrinsic CO ligand of the [NiFe] active site, and different vibrational frequencies reflect distinct redox/structural states of this cofactor.[11,50,86,144,261] The three individual CO stretching vibrations of oxidized *Ht*SH are separated by approximately 30 cm^{-1}, which is exceptional for active site species of oxidized [NiFe]-hydrogenases. This observation suggests that the active site of as-isolated *Ht*SH can adopt three configurations that strongly differ in terms of structural and/or electronic properties. The signal at 1964 cm^{-1} may reflect the apparently EPR silent "Ni_r-B-like" state (Fig. 6.1), which was previously detected for *Re*SH and other NAD(P)$^+$-reducing [NiFe]-hydrogenases, while the band at 1936 cm^{-1} is assigned to the Ni_r-S state (see below).[79,100,105,125,254] The signal at 1993 cm^{-1}, however, is unprecedented and absent in as-isolated *Re*SH and related species, *vide infra*.[71,87,105,130,254] According to relative intensities of the CO stretching bands, the contributions of the three different states varied

across different as-isolated *Ht*SH preparations. The unusual signal at 1993 cm^{-1}, however, generally represented the dominant species. As stated in literature, such a high CO stretching frequency has not been observed for any [NiFe]-hydrogenase to date. This suggests unusually high oxidation states of the metal ions, e.g. formation of ferric iron, or unusual structural features at or in close vicinity of the [NiFe] active site.[243] In general, such observations and the appearance of multiple oxidized states may result from the contact with O_2 during and after protein isolation.[105] Importantly, all IR-spectroscopically detected oxidized species of the *Ht*SH active site can be activated under reducing conditions (Fig. 6.6, traces b and c), as observed previously for, e.g., *Re*SH.[105] This indicates that the modifications reflected by the uncommon signal at 1993 cm^{-1} are reversible and not related to oxidative damage. In a recent published crystallographic analysis, an unusual coordination geometry was suggested for the *Ht*SH (see Fig. 4.5).[234] Here, the Glu32 coordinates the Ni and the terminal Cys462 is shifted into a bridging position. However, in a preliminary DFT study this unexpected structure did not induce such a strong shift in the CO stretching frequency (Marius Horch, personal communication), which might be i.a. related to the missing protein environment.

The EPR spectrum of as-isolated *Ht*SH was measured at 10 K (Fig. 6.6, trace d) and exhibits a minor signal, presumably related to a [3Fe4S] cluster. Since no such cofactor is expected for native *Ht*SH, this feature likely reflects the (partial) oxidative damage of one or more [4Fe4S] clusters, which is in line with preparation-dependent variations of the signal intensity. This situation is reminiscent of *Re*SH and the related NAD^+-reducing hydrogenase from *Rhodococcus opacus* (*Ro*), both of which exhibit similar signals related to (non-native) [3Fe4S] species.[58,87,113,222,223,254,281] Furthermore, a weak rhombic signal, detected at 35 K, (Fig. A.11, trace a) is presumably related to a paramagnetic [NiFe] active site state of as-isolated *Ht*SH. Signals related to typical active site species of oxidized "standard" [NiFe]-hydrogenases, however, were not detected, which is consistent with previous findings for $NAD(P)^+$-reducing hydrogenases from other organisms.[58,71,100,113,130,223,254,281]

Upon addition of the mild reducing agents TCEP and NADH to as-isolated *Ht*SH, bands at 1993 and 1964 cm^{-1} disappeared from the IR spectrum in favor of two new absorption features at 1971 and 1951 cm^{-1} (Fig. 6.6, trace b). The former is ascribed to the Ni_a-C state of the enzyme, which is in line with previous studies showing that Ni_a-C exhibits the highest CO stretching frequency among all catalytically active [NiFe] species.[144] The second band, observed at 1951 cm^{-1}, is assigned to the one-electron more oxidized Ni_a-S state, consistent with an intensity decrease upon hydrogen incubation of the enzyme (see below and Fig. 6.6, trace c). In *Re*SH and soluble hydrogenase I (SH1) from the hyperthermophilic organism *Pyrococcus furiosus* (*Pf*), this state corresponds to signals at 1946 cm^{-1} [105] and 1950 cm^{-1} [79], respectively (note that *Pf*SH1 differs from *Ht*SH and *Re*SH in terms of its subunit and cofactor composition).[101] The band at 1936 cm^{-1} gains intensity upon incubation of as-isolated *Ht*SH with TCEP and NADH (Fig. 6.6, traces a and b) indicating that it reflects a partially reduced [NiFe] species with a formal Ni^{2+} oxidation state. Since this CO stretching frequency is clearly lower than those observed

for most other *Ht*SH [NiFe] active site species, we tentatively assign this intermediate to the deprotonated Ni_r-S subspecies, which features a bridging OH-ligand.

The corresponding EPR spectrum of TCEP/NADH-reduced *Ht*SH was recorded at 35K and clearly shows the hydride-containing Ni_a-C state (Ni^{3+}, S= 1/2), consistent with the corresponding assignment of the strong IR absorbance at 1971 cm^{-1}. Moreover, signals attributed to a [2Fe2S] cluster (consistent with the results obtained by NRVS, Fig. A.12) and a flavin radical species were detected (Fig. 6.6, trace e). These assignments are supported by simulation and subsequent summation of the individual EPR-active components (Fig. 6.6, trace e, dashed line) and consonant with previous assignments for *Re*SH and *Ro*SH.[58,71,87,100,113,143,223,254,281] Measurements performed at 10 K (Fig. A.11, trace b) revealed an additional broad signal at g = 1.85, possibly reflecting a [4Fe4S] cluster.

Upon incubation of *Ht*SH with H_2 (in the presence of TCEP and NADH), the 1971 cm^{-1} band, assigned to the Ni_a-C state, becomes the most intense signal of the IR spectrum, and corresponding CN stretching vibrations of this catalytic intermediate can be identified at 2076 and 2089 cm^{-1} (Fig. 6.6, trace c). Moreover, a new redox species is formed as indicated by the appearance of an absorption band at 1958 cm^{-1} (Fig. 6.6, trace c). According to spectro-electrochemical measurements (Fig. 6.7, traces b and c), an enrichment of this species requires lower potentials than that of the Ni_a-C state. Therefore, we attribute this signal to the fully reduced Ni_a-SR species with corresponding CN stretching bands at 2076 and 2062 cm^{-1}, which is in line with band assignments for *Pf*SH1.[79] In case of *Re*SH, a similar set of signals, including an identical CO stretching band at 1958 cm^{-1}, has been assigned to the Ni_a-SR2 state.[100,101,105] In the current case, however, this assignment is less plausible since CO stretching bands of *Ht*SH active site redox states appear to be generally higher in frequency than their counterparts in *Re*SH. Two further weak bands at 1943 and 1934 cm^{-1} (Fig. 6.6, trace c; Fig. 6.8, trace a) might reflect Ni_a-SR' and Ni_a-SR" subspecies of the reduced state.[100,105] Consistently, these states were observed as bands at 1940 (Ni_a-SR') and 1931 cm^{-1} (Ni_a-SR") for *Pf*SH1, which also exhibits generally higher CO stretching frequencies than *Re*SH.[79] Observation of these two subspecies provides further support for the assignment of the 1958 cm^{-1} band to Ni_a-SR as there is no other signal in the IR spectrum of *Ht*SH that could be attributed to the main component of this species.

The EPR spectrum of H_2-incubated *Ht*SH, recorded at 35 K, is dominated by the signal of the [2Fe2S] cluster (Fig. 6.6, trace f) confirming further enzyme reduction. In contrast to the IR data, this EPR spectrum exhibits only trace amounts of the Ni_a-C state. However, in addition to broad features at positions typical for reduced [4Fe4S] cofactors (g = 1.83), an EPR spectrum recorded at 6.5 K (see Fig. A.11, trace c) reveals pronounced broadened signals in the field range characteristic for the Ni_a-C state, indicating strong magnetic coupling of the active site with another paramagnetic species. This temperature dependence of the Ni_a-C signal pattern can be explained by fast spin-lattice relaxation of an Fe-S cluster near the [NiFe] site, leading to enhanced relaxation and broadening of the Ni_a-C signal until its disappearance at higher temperatures. Similar magnetic interactions

have been described in detail for "standard" [NiFe]-hydrogenases,[35,82] and particularly pronounced coupling effects were also reported for *Pf*SH1,[28] *Pyrococcus furiosus* ferredoxin,[115] and individual clusters of homologous respiratory Complex I.[165,179,203] For the Ni_a-C state of *Ht*SH, this effect appears to be most pronounced for the NADH/TCEP/H_2-treated sample. Assuming that unspecific, preparation-dependent effects can be excluded, this observation suggests that spin-lattice relaxation is accelerated by coupling to a paramagnetic cofactor ([4Fe4S] species) that is barely reduced by TCEP/NADH alone.

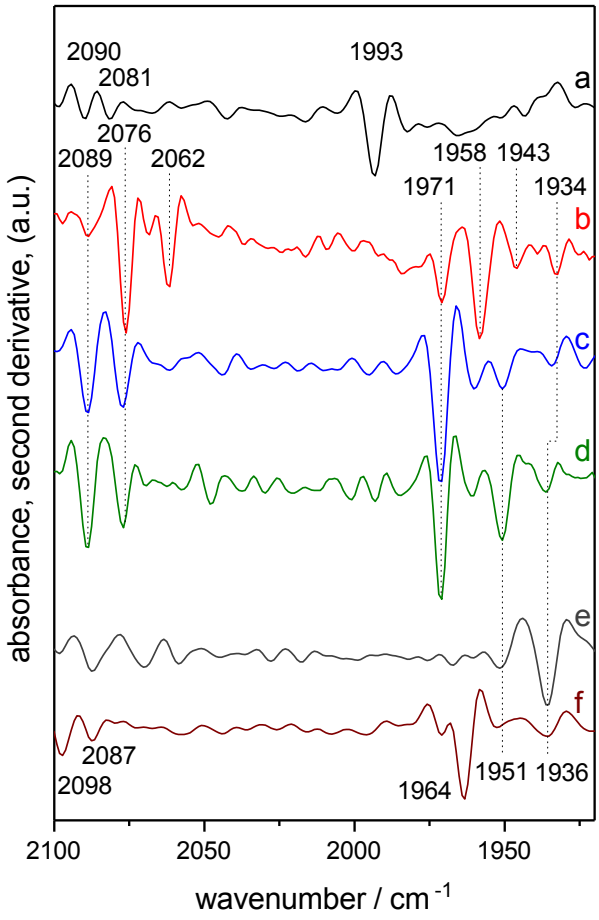

Figure 6.7. IR spectra of *Ht*SH from spectro-electrochemical measurements. Spectra were recorded at a) open circuit potential (+270 mV), b) -440 mV, c) -350 mV, d) -310 mV, e) -190 mV, and f) +460 mV vs. SHE.

To support band assignments and gain insight into the reversibility of redox reactions at the [NiFe] active site of *Ht*SH, initial IR spectro-electrochemical measurements and gas-exchange experiments were performed (Fig. 6.7 and Fig.6.8). As summarized in Table 6.4, these studies allowed a preliminary assignment of the CN stretching bands for all detected [NiFe] active site states. In Fig. 6.7 the spectro-electrochemical data essentially confirm the band assignments. As observed, the enrichment of Ni_r-S is found to require higher potentials than the formation of Ni_a-S (Fig. 6.7, traces d and e).

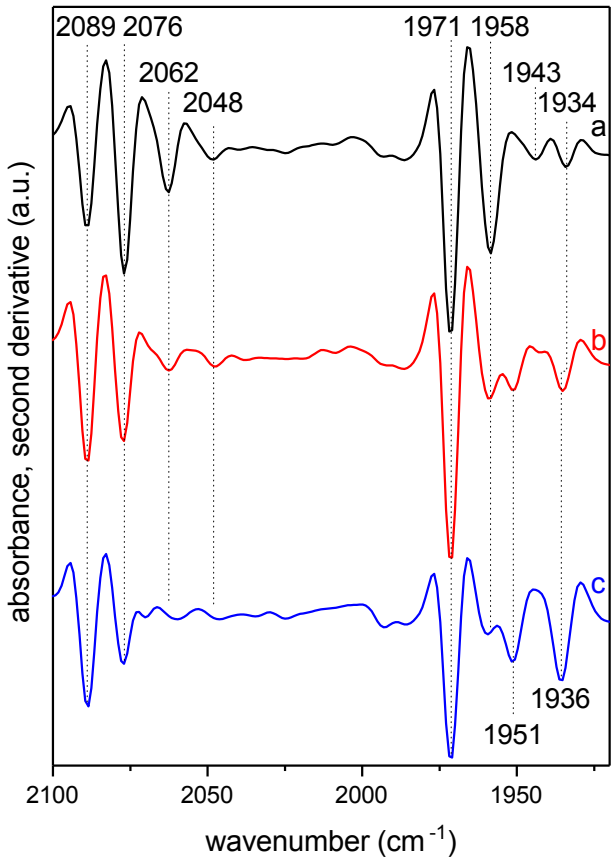

Figure 6.8. IR spectra of TCEP/NADH/H_2-treated *Ht*SH, recorded at 10 °C after slow re-oxidation of the enzyme, achieved by diffusion of air into the IR cell for 0.5 h (a), 5 h (b), and 8 h (c). Trace a represents the spectrum of *Ht*SH recorded directly after H_2 incubation (analogous to Fig. 6.6, trace c).

Moreover, CN stretching frequencies of Ni_a-S, Ni_r-B-like, and the 1993 cm^{-1} species can be tentatively assigned to signals at 2089/2076, 2098/2087, and 2090/2081 cm^{-1},

respectively (Fig. 6.7, traces a, d, and f). While CN stretching bands of Ni_r-S cannot be clearly identified in the spectro-electrochemical data (Fig. 6.7, trace e), the entirety of all previous assignments leaves the two bands at 2071 and 2058 cm^{-1} (Fig. 6.6, traces a and b) as the most plausible candidates. For further validation re-oxidation experiments, where O_2 diffuses slowly into the IR transmission cell, were carried out (Fig. 6.8). After approximately 5 h, intensities of the bands at 1934, 1943, and especially 1958 cm^{-1} decreased in favor of the signals at 1971 and 1951 cm^{-1} (Fig. 6.8, trace b), which indicates conversion of the fully reduced states to Ni_a-C (and Ni_a-S). Consistently, the intensity of CN stretching bands assigned to Ni_a-SR (2076 and 2062 cm^{-1}) decreased as well, revealing a faint doublet at ca. 2062 and 2048 cm^{-1}, which may reflect residual amounts of the Ni_a-SR' and/or Ni_a-SR" subspecies.[79,100] Upon further re-oxidation (8 h of air diffusion into the IR cell, Fig. 6.8, trace c), the band at 1936 cm^{-1} re-appeared, and the signal at 1951 cm^{-1} increased in intensity. The obtained spectrum resembles the one recorded from the TCEP/NADH-reduced sample, reflecting conversion of Ni_a-C into Ni_r-S and Ni_a-S (Fig. 6.6 trace c). Thus, findings from slow re-oxidation experiments support the IR assignment of typical [NiFe] species detected for *Ht*SH and their interrelations. The monitored interconversions also confirmed the above-made assignments of the individual [NiFe] active site species, and the corresponding redox equilibria could be established (Fig. 6.1 c). Remarkably, after reduction of as-isolated *Ht*SH and subsequent re-oxidation, the [NiFe] active site species reflected by the unusual 1993 cm^{-1} band did not re-appear (Fig. 6.7 and 6.8). Thus, we propose that the reaction resulting in this particular species is kinetically hindered, suggesting a pronounced structural reorganization. In line with the unusually high CO stretching frequency, this observation supports the idea that this oxidized state differs considerably from other typical [NiFe] active site intermediates, which might be reflected by the unusual coordination geometry found by Shomura *et al.*[234]

6.1.5. Conclusion

In this study, the first combined biochemical and spectroscopic characterization of a NAD^+-reducing [NiFe]-hydrogenase that is both thermostable and O_2-tolerant is provided. The enzyme originates from the thermophile *Hydrogenophilus thermoluteolus* TH-1^T, and its corresponding structural genes were heterologously overexpressed in the mesophilic host *Ralstonia eutropha* H16.[92] This procedure resulted in the formation of catalytically active *Ht*SH protein, which clearly shows that the hydrogenase-specific maturation machinery from *R. eutropha* is capable of synthesizing and inserting the $NiFe(CN)_2CO$ cofactor into the large hydrogenase subunit of *Ht*SH. Taking into account the successful heterologous overproduction of SH from *Rhodococcus opacus*, *R. eutropha* seems to be an excellent host for synthesis and isolation of catalytically active SH proteins from bacterial species that are so far unamenable to genetic engineering.[196]

Table 6.2 shows biochemical and structural properties of the *Ht*SH in comparison with those of other soluble $NAD(P)^+$-reducing [NiFe]-hydrogenases. The isolated *Ht*SH is a

heterotetrameric enzyme with a turnover frequency of ca. 150 s^{-1} for H_2-driven reduction of NAD^+ at pH 6.5 and 50 °C. In terms of biotechnologically relevant cofactor regeneration, the *Ht*SH is complementary to *Pf*SH1, which preferably reduces $NADP^+$ in a H_2-dependent manner at high temperature.[148,207] Although to a lesser extent when compared to *Re*SH, *Ht*SH shows catalytic H_2-mediated NAD^+ reduction in the presence of O_2 in solution assays. For *Pf*SH1, O_2-tolerant H_2 oxidation (but not $NAD(P)^+$ reduction) has so far only be shown electrochemically with immobilized enzyme.[125] Though phylogenetically closely related to *Ht*SH and *Re*SH, the purified bidirectional [NiFe]-hydrogenase from *Synechocystis* sp. seems to be rather unstable and is rapidly inactivated by O_2. The well-characterized and extraordinary O_2-tolerant *Re*SH, in contrast, shows good stability and highest activity at moderate temperatures and pH 8, but quickly loses activity at temperatures above 35 °C.[202] In summary, the *Ht*SH represents an attractive candidate for biotechnological applications, e.g., as an NADH regeneration catalyst in enzymatic cascades that rely on high temperatures and O_2 as a co-substrate.

EPR, IR and NRV spectroscopic analyses of the *Ht*SH protein revealed the occurrence of FMN, [2Fe2S], and [4Fe4S] cluster species as well as typical active site states that have been observed for other soluble $NAD(P)^+$-reducing [NiFe]-hydrogenases.[71,79,101] These include the Ni_r-B-like state that is not directly involved in H_2/H^+ cycling as well as the Ni_a-S, Ni_a-C, and Ni_a-SR states which are generally accepted to be intermediates of the catalytic cycle. While the Ni_a-C state was identified both by IR and EPR spectroscopy, all other states are EPR silent and were assigned based on IR spectroscopic analyses only. Interestingly, the Ni_a-C signal in the EPR spectrum of H_2-treated *Ht*SH was mainly observed at temperatures below 10 K, presumably due to fast spin-lattice relaxation related to magnetic coupling with another cofactor that is paramagnetic under these reducing conditions. This observation represents an important finding that could explain why Ni_a-C and other paramagnetic active site species have often not been observed for $NAD(P)^+$-reducing [NiFe]-hydrogenases.[71,101] Furthermore, the as-isolated, oxidized *Ht*SH exhibits a CO stretching vibration at 1993 cm^{-1}, which is extremely high in frequency and so far unprecedented for [NiFe]-hydrogenases. This unusual vibrational band most likely reflects an alternative geometry and/or coordination environment of the hetero bimetallic active site. Regarding the now available crystallographic data, also further spectroscopic investigations are currently in progress to gain detailed insight into the structure of this unprecedented species.[234]

6.2. An S-Oxygenated [NiFe] Complex Modelling Sulfenate Intermediates

The following passages were already published and are discussed with kind permission of Wiley.[140] As stated in chapter 5.6 the synthetic design and work was performed by Dr. Nils Lindenmaier from the group of Prof. Dr. Matthias Driess.

Oxygen is known to reversibly inhibt most [NiFe]-hydrogenases. As displayed in chapter

4.3.3 two paramagnetic redox states (Ni^{3+}, S = 1/2) are described, Ni_u-A and Ni_r-B, which differ in the time necessary for their reductive reactivation.[144] These observations are rationalized by the presence of different oxygen species in the bridging position between the two metals, i.e., a hydroxo species in case of Ni_r-B and, possibly, a (hydro)peroxide in Ni_u-A.[174,256,262] The formation of the later is acknowledged to be a key-determinant for O_2 sensitivity of standard [NiFe]-hydrogenases. However, the molecular details are still not fully understood.[263]. The Ni_u-A state is not observed in the soluble hydrogenase (see also 4.3.5).[100] Previous IR studies revealed an unusual spectrum for the active site of purified SH. Generally, the diatomic ligands of the [NiFe] metal center generate one CO and two CN stretching bands in oxygen-sensitive [NiFe]-hydrogenases. In contrast to these findings, one CO and four CN stretching modes were detected for the as-isolated, oxygen-tolerant SH.[87,100,254] Since the SH is also equipped with a standard set of diatomic ligands, the reliable interpretation for the unusual IR spectroscopic signature of the as-isolated enzyme remain to be clarified.[102,210] Horch *et al.* proposed a reversible sulfoxygenation of the active site (see also Fig. 4.2, left).[105] Thereby, one of the two bridging cysteines is the reactant which could involve the detoxification of an intermediary peroxo species (putatively Ni_u-A) by means of a sulfur-based peroxidase reaction. This suggestion might be a feasible approach for the SH which has access to low-potential electrons from NAD(P)H.[31,32,130,220] Notably, the NADH peroxidase uses such a mechanism.[280] Moreover, such reversible oxygenations of metal-bound sulfur were also detected for Ni model complexes.[49] As a result, the understanding of the fundamental principles and intermediary species are of great significance and may stimulate the design of bioinspired catalysts which are able to generate dihydrogen in the presence of atmospheric oxygen.

In view of the proposed structure and the underlying mechanism of O_2-tolerant H_2 cycling by this bidirectional, NAD^+ reducing [NiFe]-hydrogenases, synthetic S-oxygenated heterobimetallic [NiFe] model complexes are important systems for a) gaining a better understanding of the proposed bridging sulfenate moiety and b) providing a reference for (vibrational) spectroscopic studies of the biological system. So far, however, extensive modelling of the [NiFe]-hydrogenase active site mainly focused on proposed intermediates of catalytic H_2 cycling and the reactivity of the derived molecular mimics.[23,37,55,144,238] In contrast, biomimetic models for the interaction of the [NiFe] active site with O_2 are scarce. O_2-inhibited states of prototypical [NiFe]-hydrogenases served as inspiration to the modelling community, but synthetic analogues reflecting their structural properties were not reported thus far. More recently, Ogo *et al.* observed the activation of O_2 by a heterobimetallic [NiFe] complex at low temperatures, which, however, led to an Fe^{4+} side-on peroxido species with no biological analogue.[117] To gain insight into the O_2 tolerance of [NiFe]-hydrogenases, the (reversible) S-oxygenation of mononuclear Ni and homobimetallic [FeFe] thiolato complexes was investigated in pioneering studies by Darensbourg and co-workers.[49,77] However, heterobimetallic S-oxygenated [NiFe] complexes with mixed thiolato and sulfenato bridging moieties were not reported.

In this interdisciplinary approach, the first heterobimetallic S-oxygenated [NiFe] com-

plex **1** is presented and characterized, which bears one bridging thiolato S atom and one bridging sulfenato moiety, as proposed for *Re*SH (see Fig. 4.6 and 6.9). Experimental and theoretical results are analyzed with respect to selected electronic, structural, and spectroscopic properties that are relevant for the mechanistic understanding of this O_2-tolerant enzyme.[100,105]

Following the synthetic procedure for a related functional [NiFe]-hydrogenase model, the reaction of the cis-dithiolato nickel precursor Ni(bmmp-daco) (bmmp-daco = *N,N'*-bis(dimethyl)-mercaptopropyldiazacyclooctane) and $FeBr_2$ yielded compound **2**, which was isolated as a red-brown powder in 77% yield.[158,178] Its S-oxygenated congener was obtained by an analogous procedure employing the mixed thiolato/sulfenato nickel complex Ni(bmmp-daco)SO.[30] This approach led to the first heterobimetallic S-oxygenated [NiFe] complex **1**, which was isolated as a brown powder in 72% yield. The elemental compositions of **1** and **2** were confirmed by elemental analysis (see Appendix, section B).

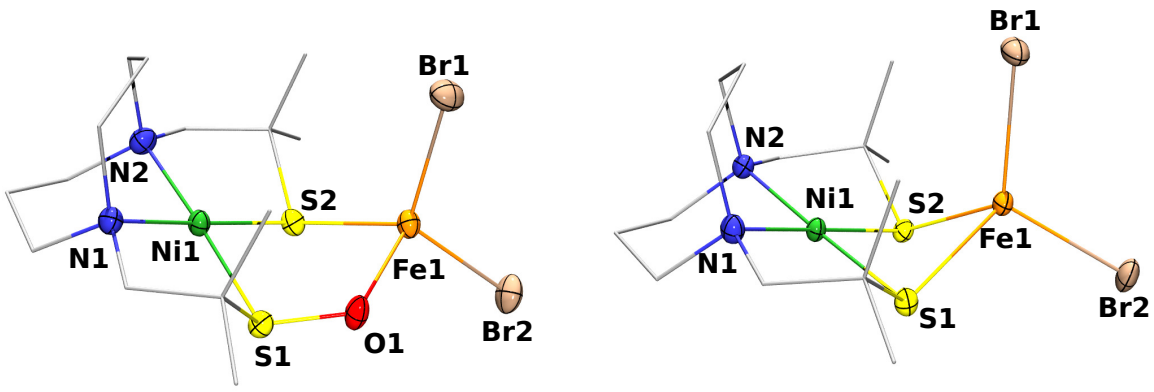

Figure 6.9. Molecular structures of **1** (left) and **2** (right) determined by single-crystal X-ray diffraction (Cambridge Crystallographic Data Centre 1515404 (**1**) and 1515403 (**2**)). Thermal ellipsoids set at 50% probability. Hydrogen atoms and co-crystallized solvent molecules are omitted for clarity. Selected distances [Å] for **1**: Fe1-Ni1 3.508, S1-O1 1.562(2), Fe1-O1 2.012(3); for **2**: Fe1-Ni1 3.074, Fe1-S1 2.4034(6), Fe1-S2 2.4100(7).

Single crystals suitable for X-ray diffraction were obtained in both cases by diffusion of diethyl ether vapor into saturated acetonitrile solutions at ambient temperature. The S-oxygenated [NiFe] complex **1** crystallizes as dark brown rods in the monoclinic space group $P2_1/c$ (Fig. 6.9, left). The Ni center is square-planar whereas the Fe center is coordinated in a pseudo-tetrahedral fashion. The distance between Ni and Fe is 3.508 Å, indicating that there is no metal-metal bond. The non-S-oxygenated [NiFe] complex **2** crystallizes as red hexagons in the space group $P2_1/c$, and the Ni(μRS)Fe core displays a butterfly-like structure with a square-planar Ni and a tetrahedral Fe center (Fig. 6.9, right). The distance between the two metal centers is 3.074 Å and thus shorter than in **1** but still indicating the absence of covalent metal-metal interactions (for further crystallographic information see Table B.1-B.4).

In the S-oxygenated complex **1**, the metal centers are bridged by one thiolato S atom and the sulfenato SO moiety with the O atom being coordinated to the Fe [d(Fe1-O1) = 2.012(3) Å]. Notably, the only other literature-known example with a sulfenato moiety that is O-bonded to a synthetic metal center is a mononuclear cobalt complex reported by Jackson *et al.*[107] In the homobimetallic diiron thiolato/sulfenato complex reported by Darensbourg *et al.*, both metal centers are bridged by the thiolato and sulfenato S atoms, and the O atom is not involved as a binding partner.[141] However, for the present heterobimetallic system, DFT calculations (see below) showed that a hypothetic isomer of compound **1** with the sulfenato ligand bridging both metal centers via the S atom is not a minimum-energy structure. In conclusion, complex **1** represents the first compound reflecting the bonding pattern proposed for the most probable sulfenate species in fully oxidized *Re*SH, which confirms the general possibility to stabilize this type of configuration.

The ^{1}H NMR spectra of **1** and **2** in CD_3OD show broad resonances and thus indicate that both complexes are paramagnetic (see Fig. B.1). Measuring the magnetic susceptibility in CD_3OD solution according to Evans' method[9,59] revealed an effective magnetic moment μ_{eff} of 4.6 μ_B for **1** and 4.9 μ_B for **2**, indicating S=2 ground states. This hypothesis was corroborated by SQUID experiments, which confirmed a temperature-independent effective magnetic moment μ_{eff} of approximately 4.9 μ_B above 50 K for both complexes (see Fig. B.4). Moreover, ^{57}Fe Mössbauer experiments in the absence of an external magnetic field revealed a large isomeric shift of δ=0.85 mm·s^{-1} with a large quadrupole splitting of ΔE_Q=2.95 mm·s^{-1} for **1** and δ=0.91 mm·s^{-1} and ΔE_Q=3.10 mm·s^{-1} for **2**, respectively, clearly revealing ferrous high-spin centers in both complexes (see Fig. B.5). Overall, the electronic structure elucidation suggests that the metal centers of both **1** and **2** can be described as low-spin Ni^{2+} and high-spin Fe^{2+} states, which is in line with the coordination geometries observed by X-ray diffraction and in partial agreement with proposals for *Re*SH ($Ni^{3+}Fe^{2+}$, low-spin).

These experimental findings were further supported by DFT calculations (for computational details see the chapter 5.11), which also suggest an S=2 ground state for both **1** and **2** in accordance with the experimental data. The lowest unoccupied molecular orbitals (LUMOs) of both complexes show antibonding character, mainly involving the $d_{x^2-y^2}$ orbital of the Ni center and the donating p-type orbitals of the surrounding N_2S_2 coordination sphere of the Ni center. The HOMOs of **1** and **2** are singly occupied molecular orbitals (SOMOs) and correspond to a d orbital of the iron center (see in the Appendix Fig. B.3).

To gain further insight into reversible cysteinate oxygenation of *Re*SH, we focused on the bonding situation of the SO moiety in complex **1** (also compare Table B.5 - B.7). Here, a calculated Mayer bond order[155,156] (MBO) of 1.14 indicates only minor double-bond character (MBO of SO in Ni(bmmp-daco)SO=1.52) and natural bond orbital (NBO) analysis[205,271] suggests a σ-bond (Table B.8). Consistently, X-ray diffraction revealed that the bond between the sulfenato S and O atoms of compound **1** is elongated in comparison to the starting material [d(S1-O1)=1.562(2) Å in **1** and d(S1-O1)=1.550(8) Å in Ni(bmmp-

daco) SO], suggesting a lower bond order of the sulfenato moiety. Furthermore, NBO analysis revealed a stronger polarization of the SO bond in **1** compared to Ni(bmmp-daco)SO. These observations can be related to O-based sulfenato binding to the Fe center, which polarizes and weakens the SO bond. During O_2 detoxification by *Re*SH, this effect may be important for the final step of sulfenate deoxygenation, which is a prerequisite for restoring catalytic H_2 cycling.[105]

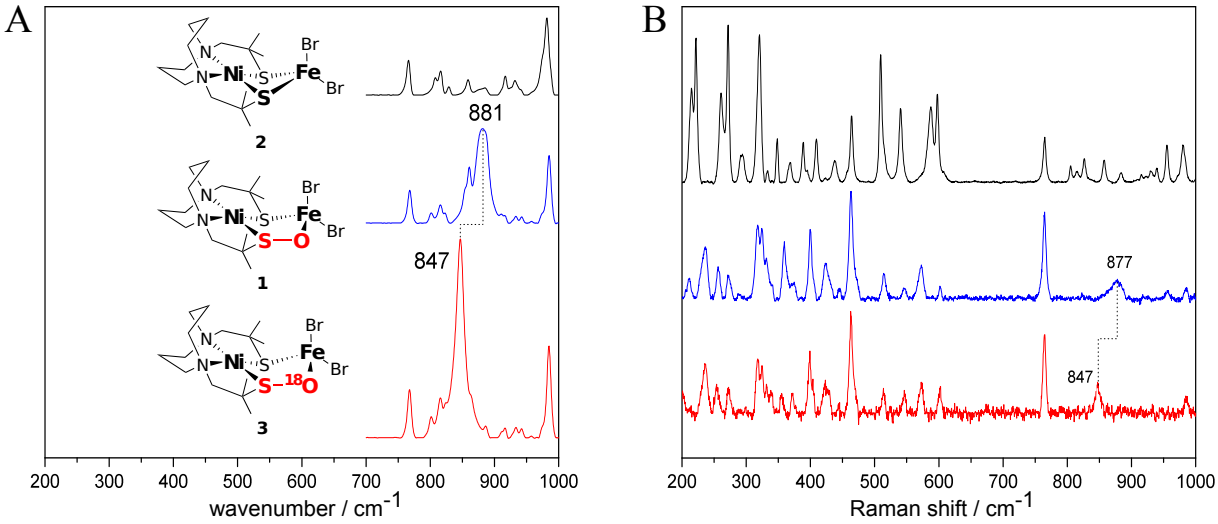

Figure 6.10. A) IR and B) RR vibrational spectra of Ni(bmmp-daco)$FeBr_2$ (**2**; black), Ni(bmmp-daco)$SOFeBr_2$ (**1**; blue), and Ni(bmmp-daco)$S^{18}OFeBr_2$ (**3**; red). The marked bands represent the $S^{16}O$ and $S^{18}O$ stretching vibrations, respectively. All spectra are baseline-corrected.

Vibrational spectroscopy is a powerful technique for characterizing hydrogenases in terms of their structural and electronic properties. So far, however, suitable approaches for the direct probing of oxygenated cysteines in [NiFe]-hydrogenases have not been established. To elucidate suitable markers for such studies, the ^{18}O-labeled S-oxygenated [NiFe] complex Ni(bmmp-daco)$S^{18}OFeBr_2$ (**3**) was also prepared (see chapter 5.6). Similar to other sulfenato complexes of Fe or Ni,[49,77,78,146] the IR spectrum of solid **1** shows a characteristic band at 881 cm^{-1}, which is absent in the non-S-oxygenated complex **2** (see Figure 6.10 A, blue and black). Furthermore, this band is shifted towards lower frequencies by about $\Delta\upsilon$=34 cm^{-1} in the spectrum of the ^{18}O-labeled [NiFe] complex **3** (Figure 6.10 A, red). This ^{18}O isotopic shift is in line with the DFT calculations [$\Delta\upsilon(SO)_{DFT}$=31 cm^{-1}] and publications on related S-oxygenated Ni complexes.[30,60,77] Based on these findings, this band was assigned to the sulfenato SO stretching vibration. Interestingly, both isotopologues of the mononuclear mixed thiolato/sulfenato complex Ni(bmmp-daco)SO exhibit higher frequencies than the corresponding heterobimetallic [NiFe] complexes [$\upsilon(S^{16}O)$=928 cm^{-1}; $\upsilon(S^{18}O)$=897 cm^{-1}; see Appendix, B.6 and B.7]. This observation confirms a weaker SO bond in complex **1** (see above), demonstrating that the SO stretching vibration is a valuable marker for evaluating relative bond lengths

and strengths of (metal-bound) sulfenate moieties. Thus computationally aided analysis of this marker mode may help to identify and characterize possible sulfenate isomers in *Re*SH.[105]

While the sulfenato SO stretching vibration of small complexes is well detected by generic IR spectroscopy, the application of this technique to large proteins is often limited by strong contributions from other signals. In contrast, resonance Raman spectroscopy selectively probes vibrational modes of a chromophore embedded in a macromolecular matrix, such as the active site of hydrogenases.[104,114] Thus, model complexes **1**-**3** were also investigated by this technique using λ=514 nm excitation.

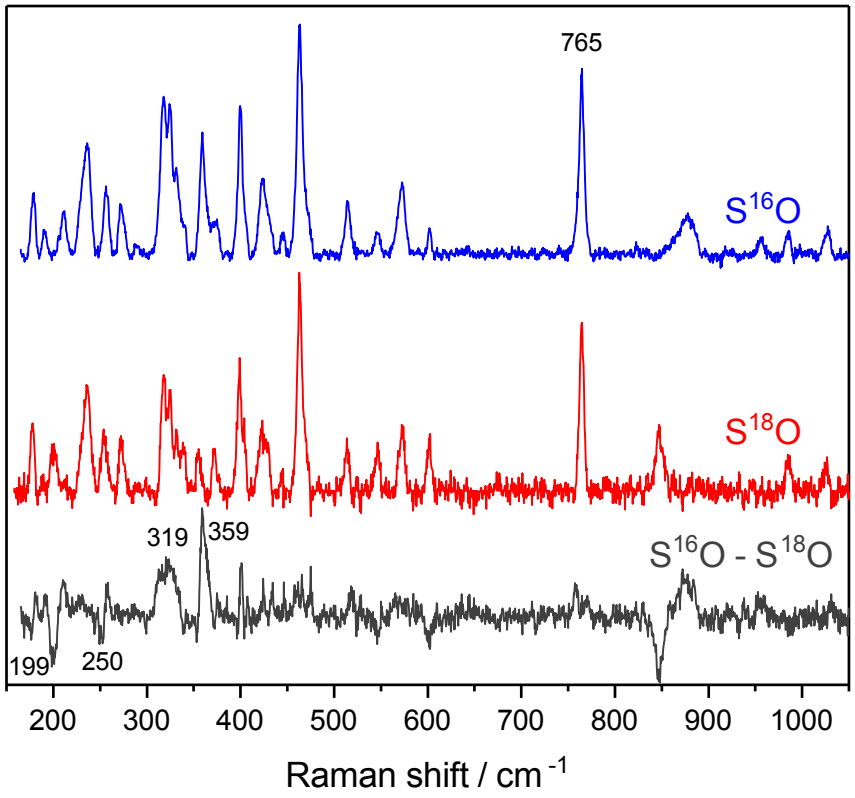

Figure 6.11. Resonance Raman spectra of Ni(bmmp-daco)$S^{16}OFeBr_2$ (**1**, blue) and Ni(bmmp-daco)$S^{18}OFeBr_2$ (**3**, red) and difference spectrum **1**-**3** (dark grey). The $S^{16}O$ (blue) and $S^{18}O$ (red) spectra were normalized with respect to the band at 765 cm^{-1} prior to the subtraction procedure.

In line with the IR data, the RR spectra of the S-oxygenated [NiFe] complexes display distinct bands at approximately 877 cm^{-1} (^{16}O-labeled; Figure 6.10 B, blue) and 847 cm^{-1} (^{18}O-labeled; Figure 6.10 B, red). This observation demonstrates that RR spectroscopy

is able to selectively probe SO stretching vibrations of metal-bound sulfenates in a coordination environment mimicking the active site of [NiFe]-hydrogenases. Furthermore, a difference spectrum calculated from the RR signatures of the ^{16}O- and ^{18}O-labeled complexes exhibits bands below 400 cm^{-1}, which likely reflect normal modes including Fe-O coordinates (see Fig. 6.11). These vibrational markers are expected to be sensitive towards variations in metal-ligand bonding. Thus, they represent further valuable probes for the characterization of metal-bound sulfenates in *Re*SH or similar enzymes.

In summary, in this chapter the first S-oxygenated heterobimetallic [NiFe] complex **1** as a structural and spectroscopic model for the S-oxygenated active site of the NAD$^+$-reducing [NiFe]-hydrogenasee from *Ralstonia eutropha* was presented. Single-crystal X-ray diffraction, vibrational spectroscopy, and DFT calculations revealed that the sulfenato moiety possesses a rather weak and polar SO bond and is bound to the iron subsite via the O atom, which is in line with the structural proposal for the S-oxygenated *Re*SH active site.[105] The present approach of biomimetic modelling in conjunction with vibrational spectroscopy provides a sound basis for the design and interpretation of future studies on this enzyme, and thus a key to the direct assessment of S-oxygenated cysteinates in O_2-tolerant dihydrogen cycling. In the future, compound **1** will also serve as a starting point for extended structural and functional modelling of biologically relevant S oxygenation.

6.3. RR and IR spectroscopy of the as-isolated and reduced Moco

In this chapter, a combined approach of RR and IR spectroscopy as well as DFT calculations was used to observe changes in the ligation sphere of the Mo ion of the Moco in Formate Dehydrogenase from *Rhodobacter capsulatus* (see Fig. 5.1). In this interdisciplinary work all DFT calculations were performed by Dennis Belger from the group of Prof. Dr. Maria-Andrea Mroginski. The synthesis of the inorganic model compound was carried out by Ricardo Nowak from the group of Prof. Dr. Carolo Schulzke and all sample-related EPR measurements were executed by PhD. Benjamin Duffus from the group of Prof. Dr. Silke Leimkühler.

As outlined in chapter 4.5 RR spectroscopy is a powerful technique to probe vibrational modes of cofactors buried inside a protein matrix, such as metal active sites or chromophores.[104] In addition, the combination of RR spectroscopy with computational chemistry by calculating the *in silico* spectrum by means of density functional theory allows an assignment of the complex experimental vibrational pattern of the active site and, in turn the extraction of valuable structural and electronic information. Such a experimental/computational concept was successfully applied to a manifold of enzymes, such as a regulatory [NiFe]-hydrogenase.[103,209,236] The final aim of this work is to contribute to an assignment of catalytically relevant intermediates of the formate splitting reaction.

6.3.1. Resonance Raman spectroscopy of the as-isolated Moco

As shown by earlier XAS studies the active site of the wild type is a hexa-coordinated Molybdenum ion in the oxidation state +VI coordinated by two dithiolene moieties, a cysteine and an sulfido ligand.[225] According to this data, a significant amount of oxo species was detectable. Furthermore, the authors observed non-integer numbers of Mo-O bonds which might indicate in addition a hydroxo species. RR spectroscopy is a very sensitive technique to determine specific metal-ligand vibrations. Thus, possible changes in the ligation sphere of the Molybdenum ion should be observable. In Fig. 6.12 the RR spectra of the as-isolated FDH^{WT} enzyme (**a**) and its catalytically inactive maturation precursor $FDH^{\Delta FdsC}$ (**c**) are displayed. The dashed lines represent the calculated Raman spectra of those structural models that exhibit the best agreement with the experimental data (see Fig. 6.12, trace **b** and **d**, see below). In contrast to the previous XAS studies, both experimental RR spectra display highly homogeneous enzyme preparations which were provided throughout the spectroscopic characterization.

The FDH harbors several different cofactors, such as the Moco active site, five [4Fe4S] as well as two [2Fe2S] clusters and a FMN. Therefore, the experimental RR spectra in Fig. 6.12 include all metal ligand vibrations as well as the deformation modes of the organic FMN. However, in the FDH^{WT} spectrum (**a**) a prominent band at 438 cm^{-1} is observed, which is absent in the $FDH^{\Delta FdsC}$ sample (**c**), but instead shows a band at at 864 cm^{-1}.

In order to validate the molecular models of the Moco active site suggested in the past[90,137,162,225] and evaluate thoroughly the current spectroscopic data, DFT calculations on six different isolated Mo models were performed (see Fig. 5.1 and further computational details in chapter 5.11). These models are characterized by the Molybdenum ion in an oxidation state +VI coordinated to the Cys386 and contain either a OH, O, SH or S as sixth ligand. In the following these models are denoted as Mo^{6+}-XH or Mo^{6+}=X. The protein environment was treated implicitly by a polarizable continuum model (PCM) with a relative dielectric constant of ε=4.[250] Note, that the Raman spectra computed for the Moco models provide only a qualitative description of the experiments that were performed under RR conditions. For the sake of clarity, only the vibrational frequency window between 300-1000 cm^{-1} is plotted where metal-ligand vibrations are expected. The normal mode assignments are given in Table 6.5. Due to the reduced size of the cofactor models, the computed Raman spectra displayed in Fig. 6.12 (trace **b** and **d**) do not reproduce all experimental spectral features. This applies specially to those bands below 400 cm^{-1}, which are mainly attributed to manifold of modes arising from the FeS clusters that give rise to relatively strong RR bands.[69,84,85,236] In the spectral region above 400 cm^{-1} the lower density of vibrational modes facilitates the identification and assignment of various relevant spectral features related directly to the Moco. Independent of the structural model, between 400-900 cm^{-1} DFT calculations predict modes involving mostly ring deformations and ring stretching vibrations of the pterin (PT) ligands. The C-S stretching vibrations of the dithiolene ligands (DT) are calculated between 700-900 cm^{-1}, in most cases coupled with C-C stretching and deformation vibrations of the

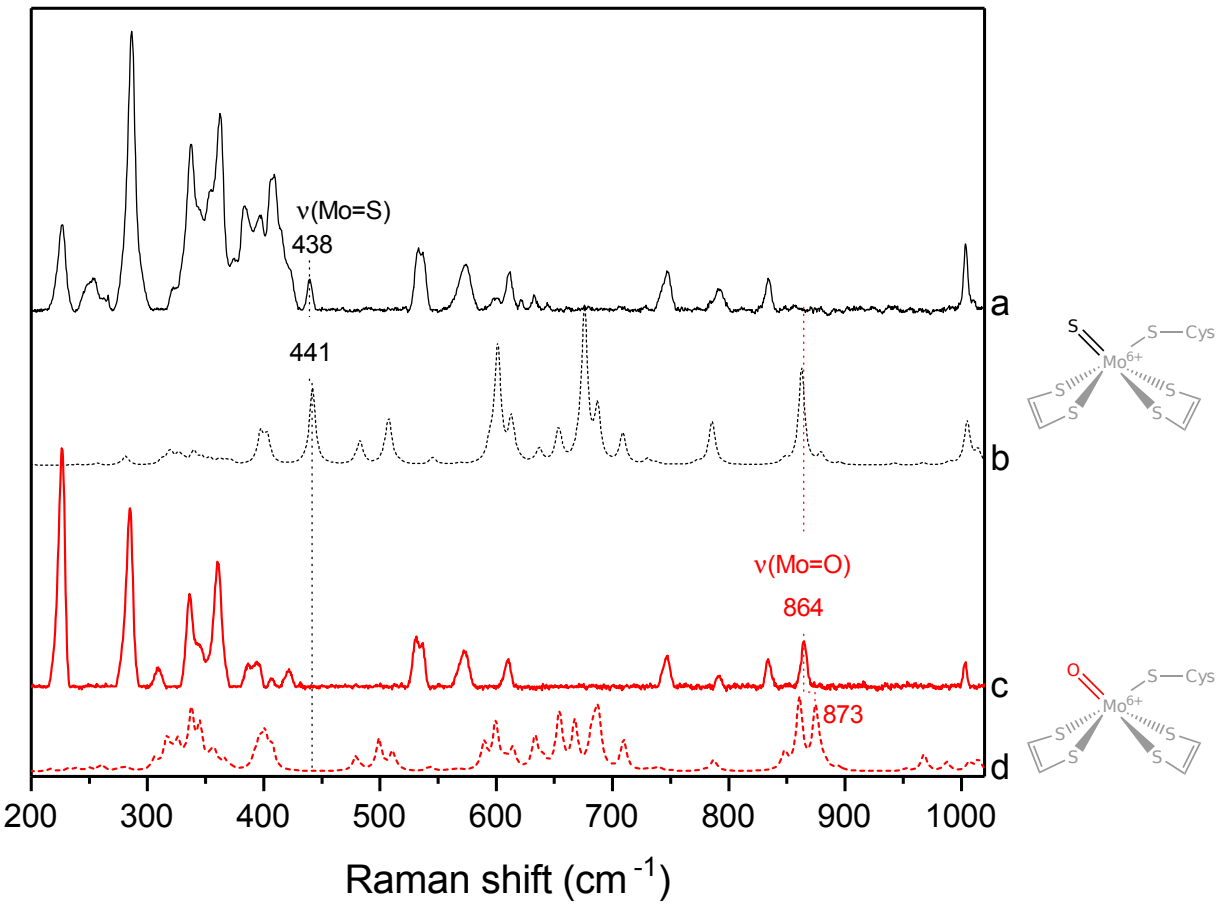

Figure 6.12. RR spectra of the as-isolated FDH^{WT} (**a**) and the FDH$^{\Delta FdsC}$ samples (**c**). The calculated spectra of those models that display the ebst match with the experimental spectra are shown as dashed lines (**b** and **d**). The corresponding color-coded structures are depicted on the right. Spectra were acquired using 5 mW of 514 nm excitation in the presence of 10 mM azide at 80 K.

neighboring rings. The vibrational modes involving the Mo ion are distributed over the entire spectral window. Mo-S stretching modes involving either the dithiolene ligands or the Cys386 are observed at frequencies below 450 cm^{-1}, while bond deformations and torsions are predicted at frequencies higher than 450 cm^{-1}. The Mo-O vibrations however, are found above 600 cm^{-1}. As a result, the stretching modes arising from Mo-S compared to Mo-O are clearly separated from each other and allow an explicit discrimination.

In the case of the Mo^{6+}-SH model, the Mo-S stretching frequency is computed at 369 cm^{-1} while Mo-S-H bending vibrations are predicted at 633 cm^{-1} and 429 cm^{-1} with very low Raman activity. Both vibrational frequencies deviate from the experimental value at 438 cm^{-1}. Contrarily, the Mo^{6+}=S model (Fig. 6.12, trace **b**) displays a pronounced band at 443 cm^{-1} assigned to Mo-S stretching mode localized on the Cys386 and which is in good agreement with the experimental RR data.

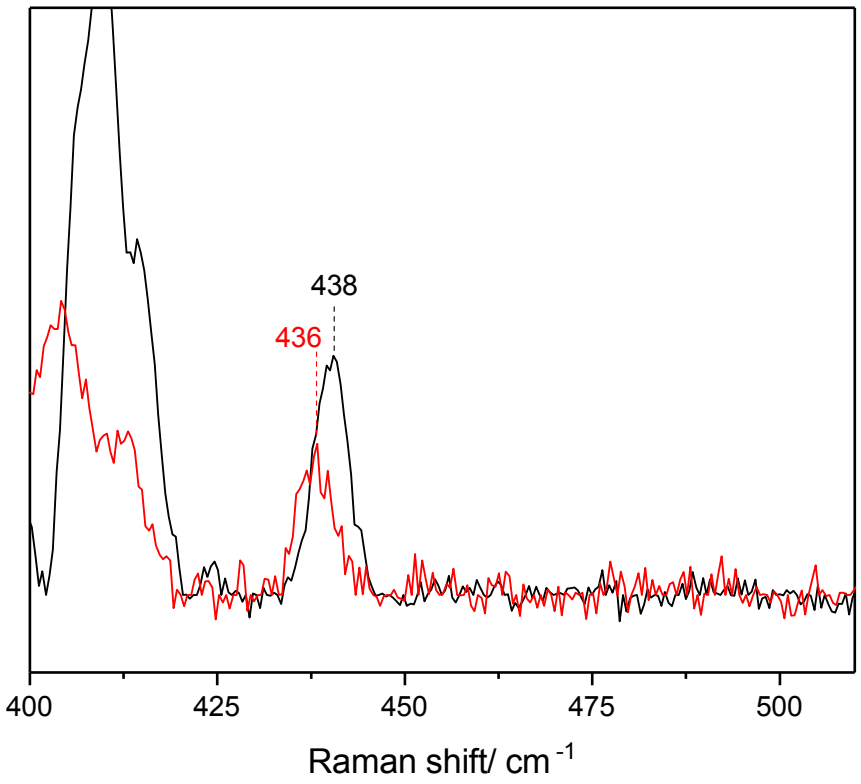

Figure 6.13. RR spectra of the FDH^{WT} in H_2O (black) and D_2O (red). Measurement conditions are the same as described in Fig. 6.12.

Interestingly, measurements performed in D_2O only lead to a small downshift pf the 438 cm^{-1} to 436 cm^{-1} (see Fig. 6.13), whereas the DFT calculations of the Mo^{6+}-SH model predict a 20 cm^{-1} upshift upon H/D exchange of the SH group. Thus, the good agreement between the experimental and calculated Raman spectra support the assignment to the Mo^{6+}=S model and thus a hexa-coordinated Moco in the FDH^{WT}.[225] In an earlier biochemical study it was shown that without the FdsC protein the Moco remains in an inactive form which is presumably desulfurized.[21] A XAS spectroscopic study suggest that this inactive FDH form harbors a hexa-coordinated active site containing an oxo ligand, two dithiolene moieties and the S-Cys(386). The authors note that the latter is observed more prominently at pH 9 and may be replaced by a further oxygen ligand at pH 7.[225] Such a pH dependence was not detected in the RR experiments performed at the two pH values. Nevertheless, structural differences at the Mo ion of the FDH$^{\Delta FdsC}$ state compared to the FDH^{WT} should also be reflected in the corresponding RR spectra. Thereby, the RR spectrum of the FDH$^{\Delta FdsC}$ lacks the peak at 438 cm^{-1} and shows a

prominent band at 864 cm^{-1} (see Fig 6.12, trace **c**). Since such a high frequency peak has not been detected in any other FDH^{WT} spectrum, the nature of this band as well as its assignment to a putative oxo-ligand at the sixth coordination site of Mo^{6+} requires verification by means of DFT calculations.

In order to determine the composition of the mode at 864 cm^{-1} and to elucidate the nature of the Mo^{6+} oxo ligand, Raman spectra calculations were performed on the Mo^{6+}_{penta}=O, Mo^{6+}_{penta}-OH models, in absence of the Cys ligand. In addition, Mo^{6+}=O and Mo^{6+}-OH with a Cys-ligand present were compared with the experimental spectrum. For the penta-coordinated Mo models the Mo-O stretching mode is calculated at 954 cm^{-1} for a Mo=O and at 700 cm^{-1} for a Mo-OH model. In both cases, the positions of the bands differ significantly from the experimental value at 864 cm^{-1}, such that the Mo^{6+}_{penta}=O and Mo^{6+}_{penta}-OH structural models are ruled out. In the case of the hexa-coordinated Mo structures where the sixth coordination site is occupied by the Cys386, the agreement between experimental and calculated spectra is significantly better, while the calculated Mo-OH frequency is too low (767 cm^{-1}) to justify the assignment to the experimental band at 864 cm^{-1}, a good agreement is found for the Mo=O stretching vibration calculated at 873 cm^{-1}. Thus, RR spectroscopy combined with DFT calculations confirms the former assumption that in the inactive $FDH^{\Delta FdsC}$ the Mo ion is coordinated by an oxo ligand.[225] While the importance of the FdsC protein in the maturation of the FDH^{WT} was already shown in activity assays, the current vibrational spectroscopic study confirmed the role of FdsC for the interconversion of the oxo to the sulfido ligand in the first coordination sphere of the Molybdenum ion.

6.3.2. IR spectroscopy of the as-isolated Moco

In general, small negatively charged molecules, such as azide or NO_3^-, enhance the stability and yield of the Moco content in enzymes. A recently published electrochemical study showed that azide inhibition strongly depends on the Molybdenum oxidation state.[211] According to that work, the Mo^{6+} species is more effectively inhibited than the Mo^{4+} state. The authors described this effect to the direct binding of azide to the Molybdenum ion. In principle, such a coordination of the azide could replace a Cys-S/Se-Mo by a Mo-N bond. Thus, changes should occur in metal-ligand related modes in the corresponding RR spectra. In the theoretical model described in the last section an implementation of the N_3^- molecule was omitted due to the reconstruction of the dithiolene and protein-based ligation as previously published.[225] Therefore, computation was repeated with azide either coordinating directly to the Mo ion or in close vicinity of the sulfido ligand. The results are summarized in Tab. 6.5. Furthermore, the IR-active asymmetric stretching vibration of the azide molecule is a sensitive marker with respect to a direct binding compared to a solely electrostatic interaction. In order to further explore the mode of azide inhibition, RR and IR spectroscopy were applied in combination with DFT calculations.

In Fig. 6.14 the RR spectra of the as-isolated FDH^{WT} supplied with 10 mM azide (black) and after azide removal (grey) are displayed (for experimental details see chapter

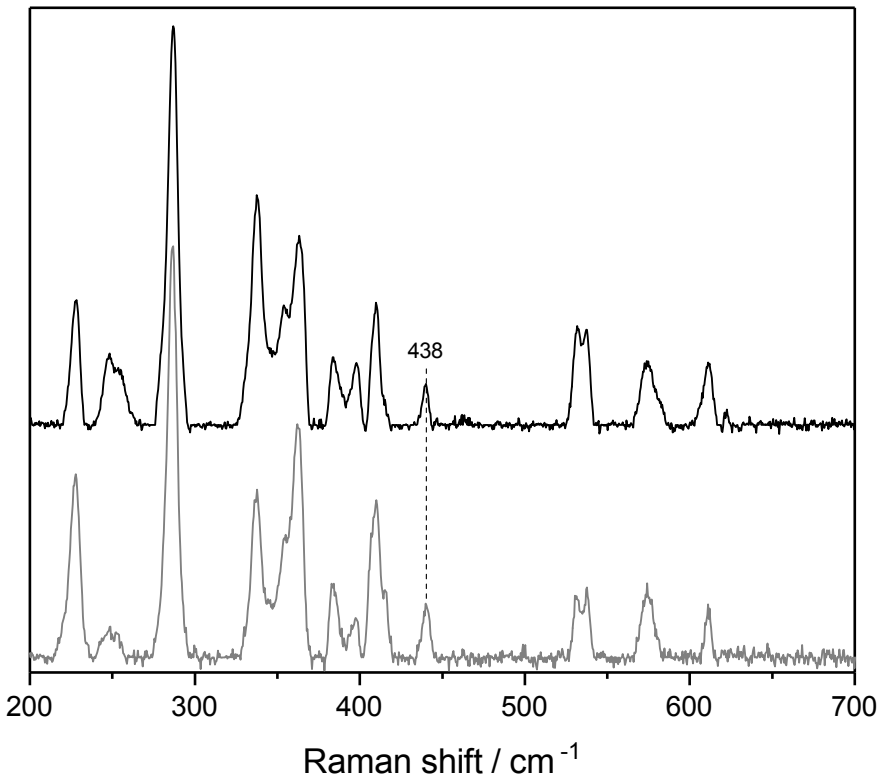

Figure 6.14. RR spectra of the FDH^{WT} supplied with 10 mM azide (black) and after azide removal (grey) and are toluene and baseline corrected (see chapter 5.8). Spectra were acquired using 514 nm excitation at 80 K.

5.1). The spectra are very similar with respect to the band positions, displaying only slight differences in the band intensities. However, such alterations could be also related to different concentrations, a varying cofactor content, small variations in the baseline correction etc. and are, therefore, difficult to interpret. According to the calculations the Mo-S(Cys) and the Mo-N stretching vibration are located at 375 and 376 cm^{-1}, respectively (see Tab. 6.5). With respect to their Mo=S stretching vibrations, the two theoretical models afford frequencies that lie within the error range for DFT calculations and are, thus, indistinguishable. Notably, the FDH additionally contains five [4Fe4S], two [2Fe2S] clusters and a flavin cofactor, which contribute to the RR spectrum preferentially in their oxidized states. Therefore, it is very difficult to discriminate different Mo^{6+} ligation spheres in the range between 300-400 cm^{-1} in the RR experimental data. As an alternative, the asymmetric stretching mode of azide can be probed by IR spectroscopy. It lies in the spectral range between 2000-2200 cm^{-1}, which is free of any protein related

vibrational modes. Applying the previously derived computational model, different putative interaction scenarios were calculated and compared with the experimental results (see Tab. 6.5). In such way, this approach should in principle allow for a discrimination of the azide binding location at the Moco.

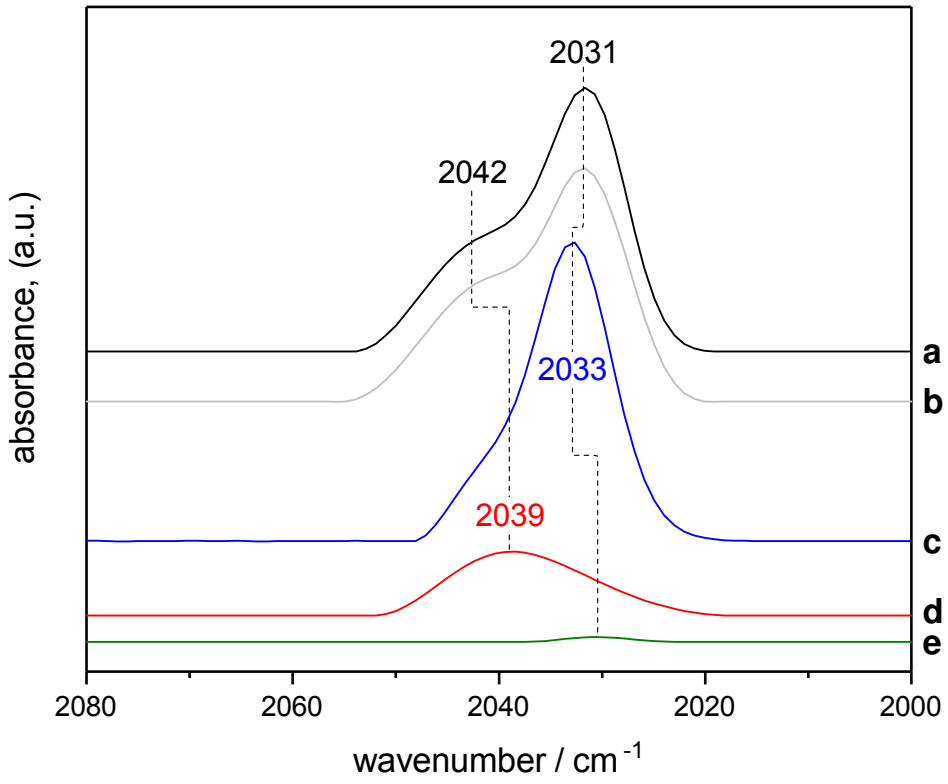

Figure 6.15. IR spectra of the as-isolated FDH^{WT} incubated with 10 mM azide (**a**), FDH^{WT} incubated with 10 mM azide and treated with 10 mM formate (**b**), FDH$^{\Delta FdsC}$ incubated with 10 mM azide (**c**), apo-FDH incubated with 10 mM azide (**d**) and FDH^{WT} after removal of azide by three subsequent buffer exchanges into azide free buffer (**e**). Free, soluble azide (2048 cm^{-1}) is removed by spectral subtraction prior to baseline correction.

In Fig. 6.15 the as-isolated IR spectra of the FDH^{WT} supplied with N_3^- (Fig. 6.15, trace **a**) is displayed. It reveals two bands at 2031 cm^{-1} and 2042 cm^{-1}. Interestingly, upon treatment with formate the spectrum does not reveal any significant changes (trace **b**). According to EPR spectroscopy a Mo^{5+} signal is detectable after incubation with formate accounting for a reduction of the active site (Benjamin Duffus, personal communication). Regarding a direct interaction between the azide molecule and the Mo ion, a shift of the stretching frequency would be expected upon changing the oxidation state from Mo^{6+} to Mo^{4+}/Mo^{5+}. Therefore, a binding in the close vicinity of the active site might be more

plausible because of the insensitivity of the asymmetric mode. A slight shift to 2033 cm^{-1} is observed in the $FDH^{\Delta FdsC}$ (trace **c**). As described in the previous section, this particular species exhibits an oxo ligand. In comparison, the apo-protein, which does not harbor the Moco, shows just one band at 2039 cm^{-1} (trace **d**). The latter, which represents the azide bound somewhere at the protein, is comparable to the band at 2042 cm^{-1} in the FDH^{WT} (trace **a**). The small shift observed between the apo-protein and FDH^{WT} could be a result of structural rearrangements in the protein upon Moco insertion. So far, the second azide interaction site is unknown. Guo *et al.* recently reported the azide-inhibited crystal structure of a metal-free FDH from *Candida boidinii*.[83] In this enzyme, azide inhibition is purely based on electrostatic interactions in the catalytic center NAD^+. The related N_3^- stretching frequency was observed at 2045 cm^{-1}. Albeit, this particular cofactor is not found in the FDH^{WT}, it still contains a FMN which might be a putative azide interaction site. In trace **e** the azide was removed by centrifugation which results in a loss of signal. This can be viewed as a control experiment, since azide-free samples were further used in the reduction process of the FDH^{WT} (*vide supra*).

Table 6.5. Experimental and calculated values (cm^{-1}) for the vibrational modes of different Moco azide systems.

	Experimental	N_3-Mo^{6+}=S	(Cys)S-Mo^{6+}=S + N_3^-
$\upsilon(N_3)$	2031	2113	2030
υ(Mo=S)	438	449	448
υ(Mo-N_3)		376	
υ(Mo-S(Cys))			375

The experimental data is compared to theoretical frequency calculations of the azide molecule in different sites at the Moco. The results are displayed in Table 6.5. The calculated value for the asymmetric stretching of the azide molecule in the direct binding scenario at the Moco is located at 2113 cm^{-1}, which is a shift by 82 cm^{-1} compared to the experimental value. On the contrary, an electrostatic interaction with the sulfido ligand would yield a theoretical stretching mode at 2030 cm^{-1}. The latter agrees very well to the experiment. Azide is known to inhibit metal-dependent as well as metal-free FDHs.[19,195] Thus, a common inhibition mechanism is rather likely than two individual ones. It was shown that in metal-free FDHs the azide interacts with His and Arg residues in the active site by hydrogen bonding.[195] This may also be in line with the pH dependence of the azide inhibition in *E .coli* FDH-H.[211] Here, at acidic pH the inhibition is stronger than in basic medium, which could be related with protonation/deprotonation of certain amino acids, especially the protonation state of the His. The important His and Arg couple is also present in the Moco binding pocket of the FDH^{WT}.[90] In summary, the present work highlights the benefit of vibrational spectroscopy in the determination of possible azide interaction sites at the Moco. A direct binding to the Moco as favored by Robinson *et al.* is very unlikely by comparing the experimental data with the DFT

calculations. According to the latter, an azide location close to the Moco yields a much better agreement between theory and experiment. However, one has to note that the protein environment is not considered in the model, due to the lack of a well-resolved crystal structure. These investigations are currently under way and may provide the basis for a quantum mechanics/molecular mechanics (QM/MM) approach in the future. Additionally, a model complex mimicking the active site and containing an azide ligand is currently synthesized, which may be used as a spectroscopic probe in order to validate the experimental data found in the FDH^{WT}.

6.3.3. Resonance Raman spectroscopy of the reduced Moco

The FDH^{WT} is a very complex enzyme harboring multiple cofactors, which all contribute to the RR spectrum.

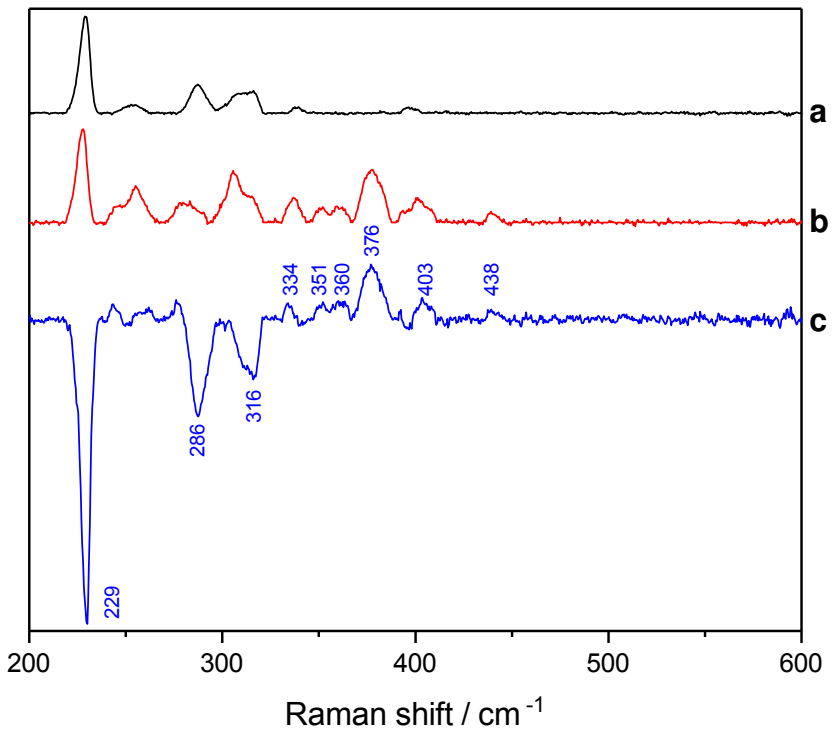

Figure 6.16. RR spectra of the reduced, azide-free apo-FDH using 10 mM NADH (**a**). The reduction of FDH was performed by treatment with 10 mM formate as well as azide removal by centrifugation (**b**) and **c** is the difference spectrum of **b-a**. Both spectra were scaled to the phenylalanin band at 1000 cm^{-1}. Spectra were acquired applying the conditions described in Fig. 6.12.

In contrast to its oxidized form, the fully reduced state of the FMN is known to be a very poor Raman scatterer as shown by many studies of flavoproteins.[94,272,282] In addition, the reduced [4Fe4S] clusters do not exhibit any resonance enhancement at 514 nm.[235,236] Assuming the latter two cofactors are completely reduced, only the [2Fe2S] clusters and the Mo active site are putative contributors to the RR signals.[69,84,85] The enzyme was anaerobically reduced using 10 mM formate. In addition, azide was removed by centrifugation (see chapter 5.1 and Fig. 6.15, trace **e**) producing much more reproducible spectroscopic results than after an aerobic, azide-containing treatment. The enzyme is still capable of oxidizing formate by subsequent cofactor reduction, which is revealed by the detection of reduced FeS clusters and a Mo^{5+} signal in EPR spectroscopy (Benjamin Duffus, personal communication). Furthermore, the absence of vibrational bands above 500 cm^{-1} indicates a fully reduced flavin.[94] One has to consider that the protein samples comprise a general Moco loading between 30-50%. Therefore, it is interesting to observe the lack of modes in this particular spectroscopic region which may suggest an autocatalytic behavior between free soluble and bound flavins of the enzyme.

Table 6.6. Comparison of experimental RR data of the FDH^{WT} derived in this work and in comparison oxidized and reduced [2Fe2S] proteins as well as a [4Fe4S] protein from previous studies in cm^{-1}. Measurement parameters are depicted in the footnotes.

Protein	RR modes [cm^{-1}]								
reduced FDH[a]	229*	286*	316*	334	351	360	376	403	438
oxidized ferredoxin[b]		282	329	339		357	367	395	426
oxidized putidaredoxin[c]		291	320	344			370	400	426
reduced putidaredoxin[c]		273	307/319				381	406	
reduced ferredoxin[d]		267/280	310	328			370	390	
oxidized [4Fe4S] iron protein[e]	248	265	281	335		356		391	

[a] RR modes marked with an * are negative peaks derived from the subtraction procedure displayed in Fig 6.16.

[b] Ferredoxin from *Porphyra umbilicalis*. Data taken from ref.[85]. The sample was excited with 514 nm at 77 K applying 100-150 mW laser power.

[c] Putidaredoxin from *Pseudomonas putida*. Data taken from ref.[69]. 2 mM of protein sample was excited with 514 nm at 17 K applying 10 mW laser power. The reduction was performed using 40 mM dithionite.

[d] Ferredoxin from *Clostridium pasteurianum*. Data taken from ref.[69]. 2 mM of protein sample was excited with 514 nm at 17 K applying 10 mW laser power. The reduction was performed using 40 mM dithionite.

[e] Iron protein from *Clostridium pasteurianum*. Data taken from ref.[68] 2 mM of protein sample was excited with 457.9 nm at 17 K applying 10 mW laser power.

In order to assign putative Mo-related modes, the corresponding apo-protein which contains all other cofactors except the Moco was used as a reference system. In Fig. 6.16, trace **a** displays the RR spectrum of the FDH^{Apo} treated with 10 mM NADH. In

trace **b**, the reduced FDH^{WT} spectrum is shown and in trace **c** the difference spectrum of FDH^{WT} minus FDH^{Apo}. While negative peaks in the difference spectra may also result from different protein folding and/or differences in cofactor concentration, the labeled six positive peaks are most likely attributed to the reduced Moco although contributions from reduced [2Fe2S] and residual amounts of oxidized [4Fe4S] clusters are not negligible.[68,69,84,85] These peaks are located at 334, 351 360, 376, 403 and 438 cm^{-1} and the results are summarized in Tab. 6.6. Especially, the modes below 400 cm^{-1} most likely represent a overlap between FeS clusters and active site vibrations. Therefore, these bands are not considered in the further analysis of active site species (*vide infra*). However, for the two bands at 403 and 438 cm^{-1} only overlays from the [2Fe2S] clusters are possible. In the oxidized putidaredoxin and ferredoxin a band is located at 426 cm^{-1} which significantly downshifts upon reduction to 390 and 406 cm^{-1}, respectively. Therefore, in the fully reduced enzymatic sample contributions from [2Fe2S] clusters can be ruled out to be the origin of the 438 cm^{-1} mode, albeit not a priori of the 403 cm^{-1} mode. Thus, both bands may be considered as candidates for the Mo=S stretching modes in different reduced active site states. Surprisingly, the mode at 438 cm^{-1} undergoes only a minor frequency shift of less than 1 cm^{-1} in comparison to the oxidized state (see Fig. 6.12).

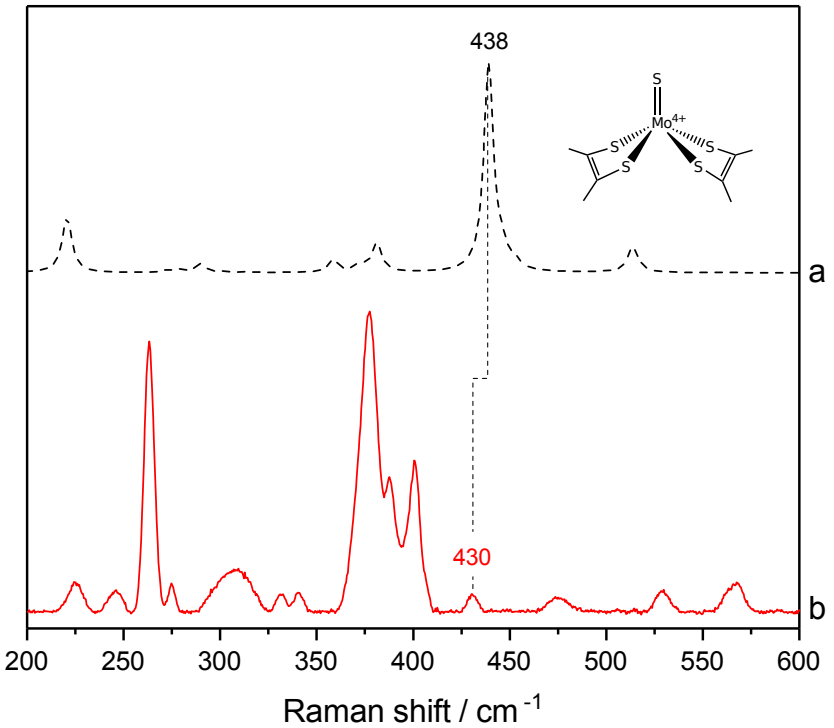

Figure 6.17. *In silico* spectrum (**a**) of the inorganic MoS(dmdt)$_2$ complex, which is shown at the top right corner and the corresponding experimentally recorded spectrum in acetonitrile (**b**) using 0.2 mW of 514 nm excitation at 80 K.

In order to explain the minor shift of the 438 cm^{-1} mode, a small inorganic, penta coordinated MoS(dmdt)$_2$ complex was investigated (for further details see 5.7). Interestingly,

the calculated peak in acetonitrile is located exactly at 438 cm^{-1}. The corresponding experimental value is found at 430 cm^{-1}, depicting only a minimal shift in organic solvent compared to the value observed in the enzymatic sample (see Fig. 6.17, trace **b**). Thus, it could be possible that the monitored bands in Fig. 6.16 trace **c** indeed belong to the reduced state of the Moco.

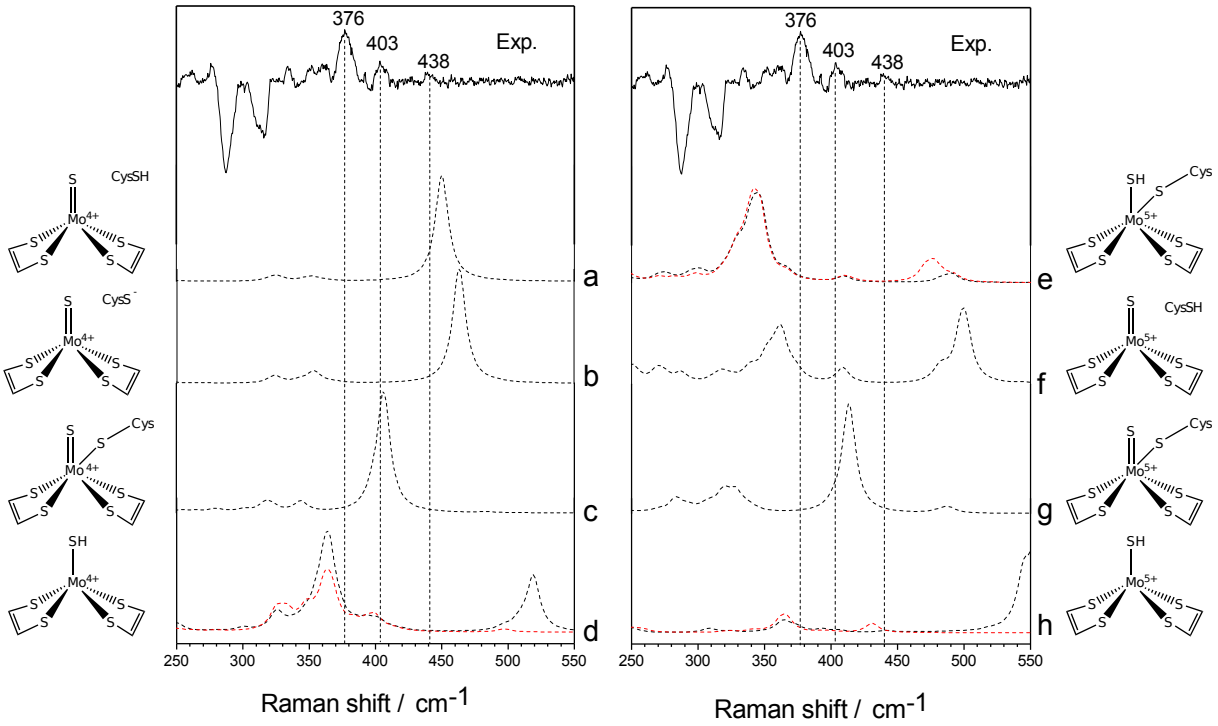

Figure 6.18. Comparison between the experimental spectrum (top) and different computed DFT spectra belonging to the different structural and electronic active site models. The corresponding structures around the Mo ion with different charges are shown left and right. The red dashed lines indicate calculated spectra in D_2O.

For the reduced FDH^{WT}, the chemical nature of the sulfur-ligand at the Mo center and its immediate environment were investigated by means of DFT calculations. For this purpose, eight structural models of a reduced Moco were generated and energy-minimized. These models differ in the nature of the sulfur-ligand (S or SH) and the presence and protonation state of Cys386 and the oxidation state of the Mo center (+IV or +V). The calculated Raman intensities of Mo-vibrational modes are plotted in Fig. 6.18 together with the corresponding structures. Normal modes involving the Mo^{4+} are predicted very near the experimental values. The band at 438 cm^{-1} is best reproduced by a penta-coordinated Mo^{4+}=S with a protonated Cys386 (CysH) model with deviations of only 12 cm^{-1} with respect to experiment (Fig. 6.18, trace **a**). This model is characterized by the presence of a protonated Cys386 directly interacting with the sulfido-ligand at the Mo center. The presence of the deprotonated Cys386 induces an additional 13 cm^{-1} upshift of the Mo^{4+}=S stretching mode as predicted for model Mo^{4+}_{penta}=S (Fig. 6.18,

trace **b**).

The spectral feature at 403 cm^{-1}, however, can be very well described by model Mo^{4+}=S(Cys) consisting of a hexa-coordinated Moco with a sulfido ligand in the fifth coordination site and the S-Cys386 on the sixth-coordination site. Here, the Mo^{4+}=S stretching mode is predicted at 406 cm^{-1} (Fig. 6.18, trace **b**). Interestingly, this vibrational mode does not seem to be significantly influenced by a change of the oxidation state of the Mo ion. In an equivalent Mo^{5+}_{hexa}=S(Cys) model, the Mo^{5+}=S stretching frequency is predicted to only 6 cm^{-1} higher than the experimental value (Fig. 6.18, trace **g**). Thus, from these spectra calculations it is not possible to discard the presence of a hexa-coordinated Mo^{5+} species. In addition, EPR spectroscopy shows the presence of a paramagnetic Mo^{5+} species supporting the idea of a mixture of reduced states (Benjamin Duffus, personal communication). However, contributions from reduced [2Fe2S] clusters cannot entirely ruled out. The largest deviations from the experimental findings are predicted for the Mo-SH models (Fig. 6.18, trace **d**, **e**, **h**), where the thiol group represents the axial ligand. For all computed reduced Mo^{4+} or Mo^{5+} states, the Mo=S band appears at wavenumbers above 438 cm^{-1}. In addition, no significant H/D effects related to the thiol groups could be detected (see Appendix section C, Fig C.1). Furthermore, in the computed Mo^{4+}-SH model, the thiol group was energetically unstable and resulted in an immediate proton transfer towards the sulfur of the Cys(386) (see Dennis Belger, private communication).

The assignment of the band at 376 cm^{-1} is difficult. Attributable modes belong either to one of the thiol-containing models or to the penta coordinated Mo^{5+}=S with a protonated Cys386 (Fig. 6.18, trace **f**). However, the latter also produces a band above 450 cm^{-1}. As a result, none of the applied models can reproduce this vibration accurately and thus, it is most likely associated with the vibrations of the reduced [2Fe2S] or residual oxidized [4Fe4S] clusters (see Tab. 6.6).[69,84,85]

In conclusion the data obtained from RR and IR spectroscopy in combination with DFT calculations may help to elucidate the underlying mechanism of the catalytic cycle in FDH. Based on the RR spectroscopic results for the as-isolated state, it was possible to demonstrate that the Moco contains six sulfur-related ligands. From the IR experiments a direct binding of the azide molecule to the Mo ion appears to be an unrealistic scenario, although, it can not be fully discarded at this stage and further experiments are necessary to prove this assumption in the future. Currently, the small $MoS(dmdt)_2$ complex incorporating an azide ligand is synthesized, which might serve as a reference system for IR and RR experiments. In Fig. 6.19 a proposal for the catalytic cycle is outlined. Based on the spectroscopic results, it is impossible to verify whether the formate molecule is split via a direct binding or a hydride transfer mechanism. The first stable intermediate observed in this work is a penta coordinated Mo^{4+} species containing additionally a protonated cysteine. After transfer of the proton to the protein the Cys386 rebinds to the Mo ion generating a hexa coordinated Mo^{4+} state. This is followed by two individual electron transfer reactions to an intermediary hexa-coordinated Mo^{5+} state and finally to the fully oxidized Mo^{6+}. The location of the proton hyperfine coupling detected in

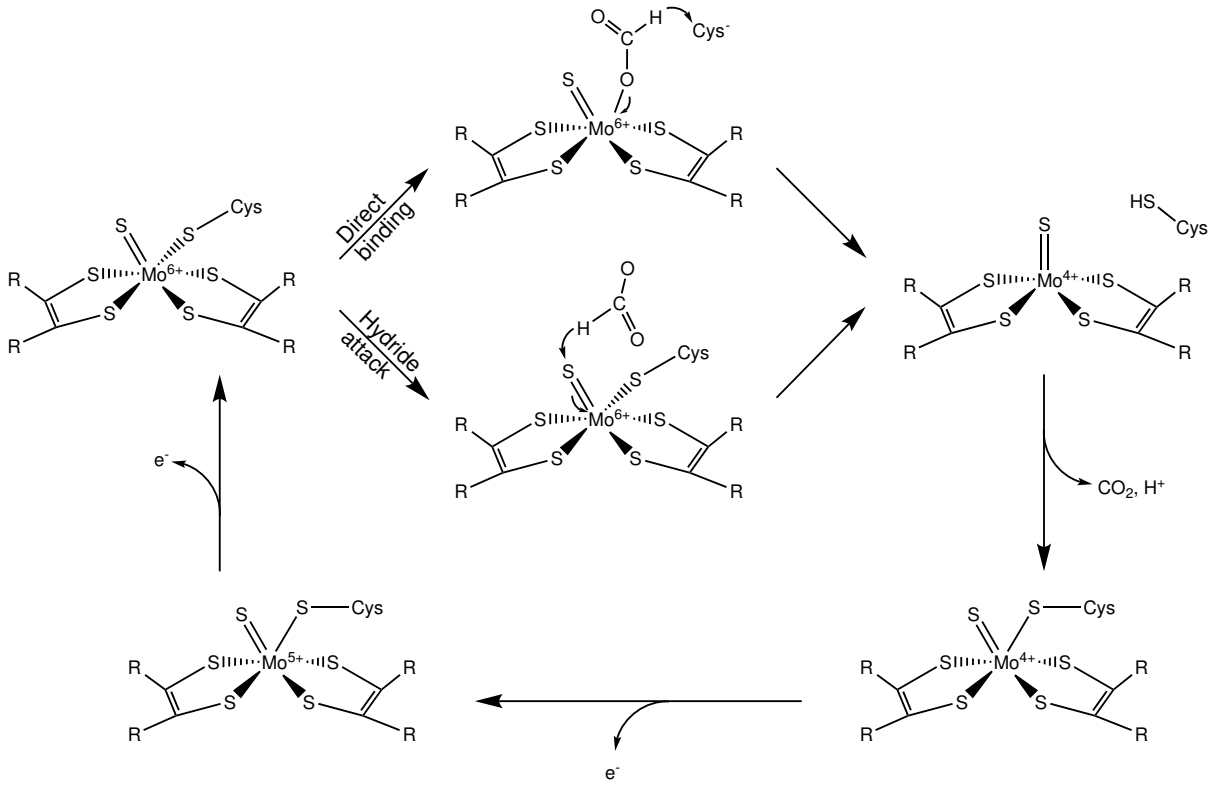

Figure 6.19. Proposed catalytic cycle based on RR spectroscopy and supporting DFT calculations. After formate oxidation a Mo^{4+} state is generated which contains a protonated cysteine. After removal of the proton, two individual single electron transfer reactions restore the Mo^{6+} species.

EPR spectroscopy remains unclear by this analysis and awaits further experimental and computational efforts. In conclusion, vibrational spectroscopy was applied successfully to characterize the electronic structure of the Moco active site. This study provided valuable information about putative intermediates involved in the catalytic cycle. RR spectroscopy was added to the analytical tool set characterizing FDHs and may provide in combination with other spectroscopic techniques and calculations more detailed insights into the fundamental properties of the Molybdenum-based chemistry in these enzymes.

Appendices

A. [NiFe]-hydrogenase

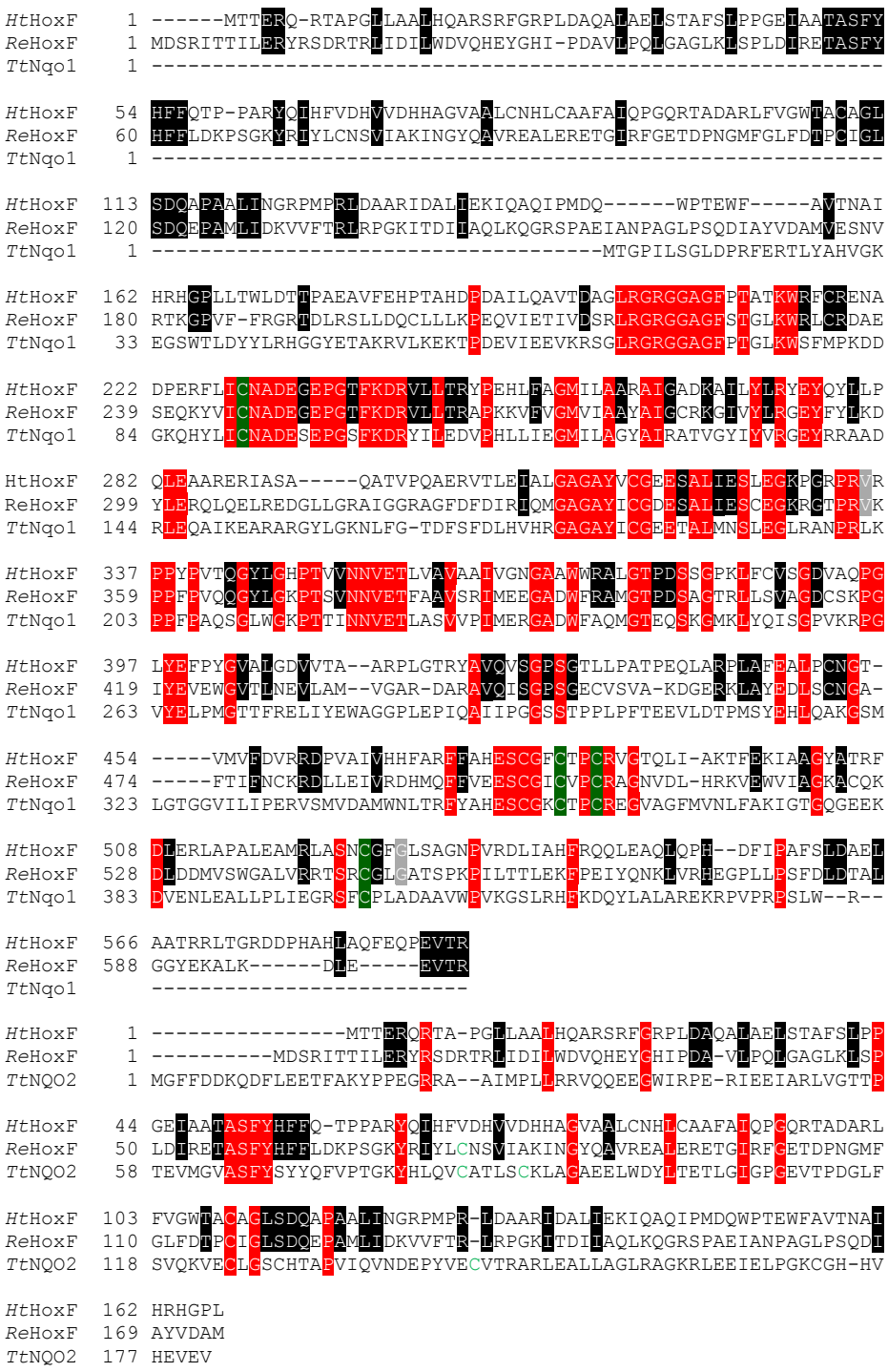

Figure A.1. Alignment of the *Ht*SH subunit HoxF with *Re*SH and the corresponding Nqo1/2 of Complex I from *Thermus thermophilus* (*Tt*). Amino acid residues that are conserved in all three species are highlighted in red, those conserved only among *Ht* and *Re* are boxed in black. Amino acid residues supposed to be involved in the coordination of Fe-S clusters are indicated in green. HoxF represents a fusion protein of Nqo2 and Nqo1 from *Tt*. Therefore, two separate alignments were made. One shows the alignment of the complete *Ht* and *Re* HoxF proteins with NqoI (revealing similarities in a large C-terminal region), and the other one aligns the N termini of the two HoxF proteins with Nqo2.

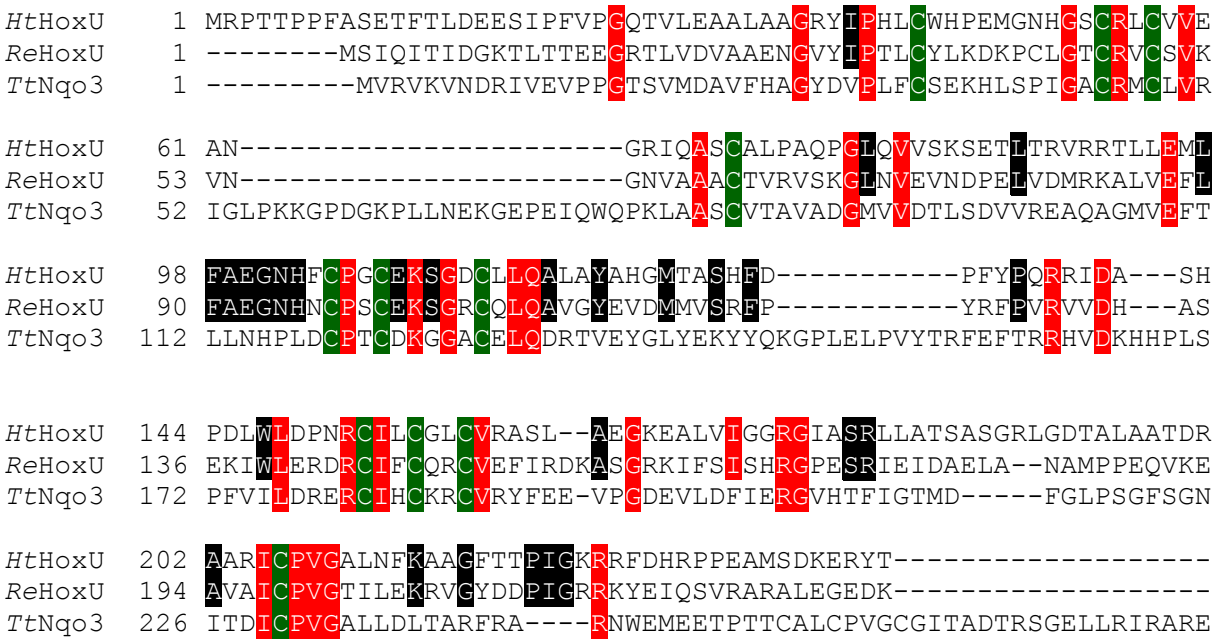

Figure A.2. Alignment of the *Ht*SH subunit HoxU with *Re*SH and the corresponding Nqo 3 subunit of Complex I from *Tt*. The color-code is the same as in Fig. A.1. As the HoxU subunits of *Ht* and *Re* represent a truncated form of Nqo3, only the first 281 amino acid residues of Nqo3 were used for the alignment.

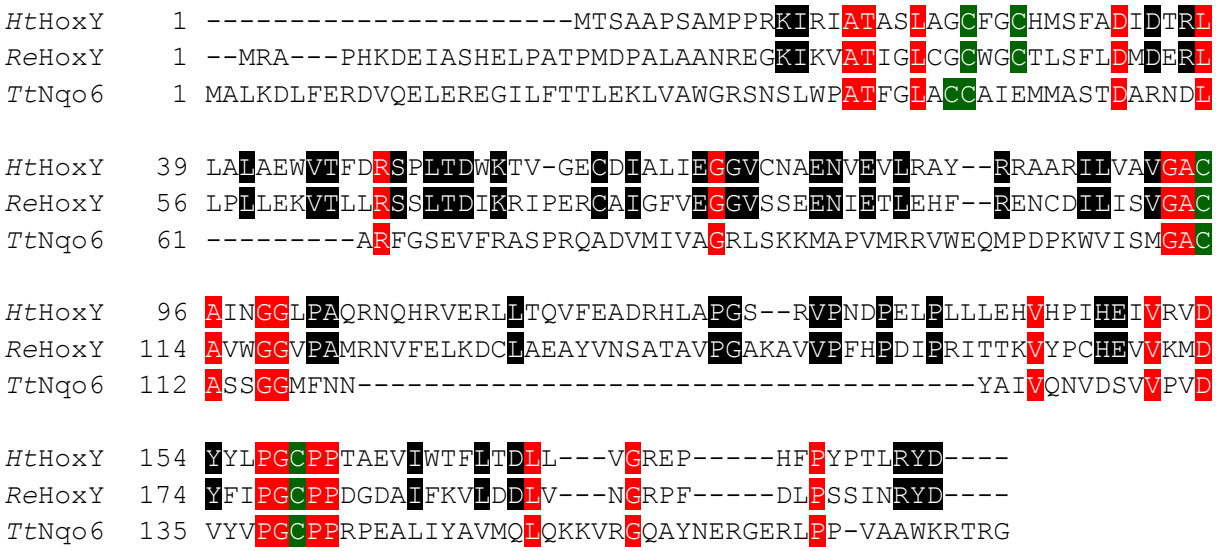

Figure A.3. Alignment of the *Ht*SH subunit HoxY with *Re*SH and the corresponding Nqo 6 subunit of Complex I from *Tt*. The color-code is the same as in Fig. A.1.

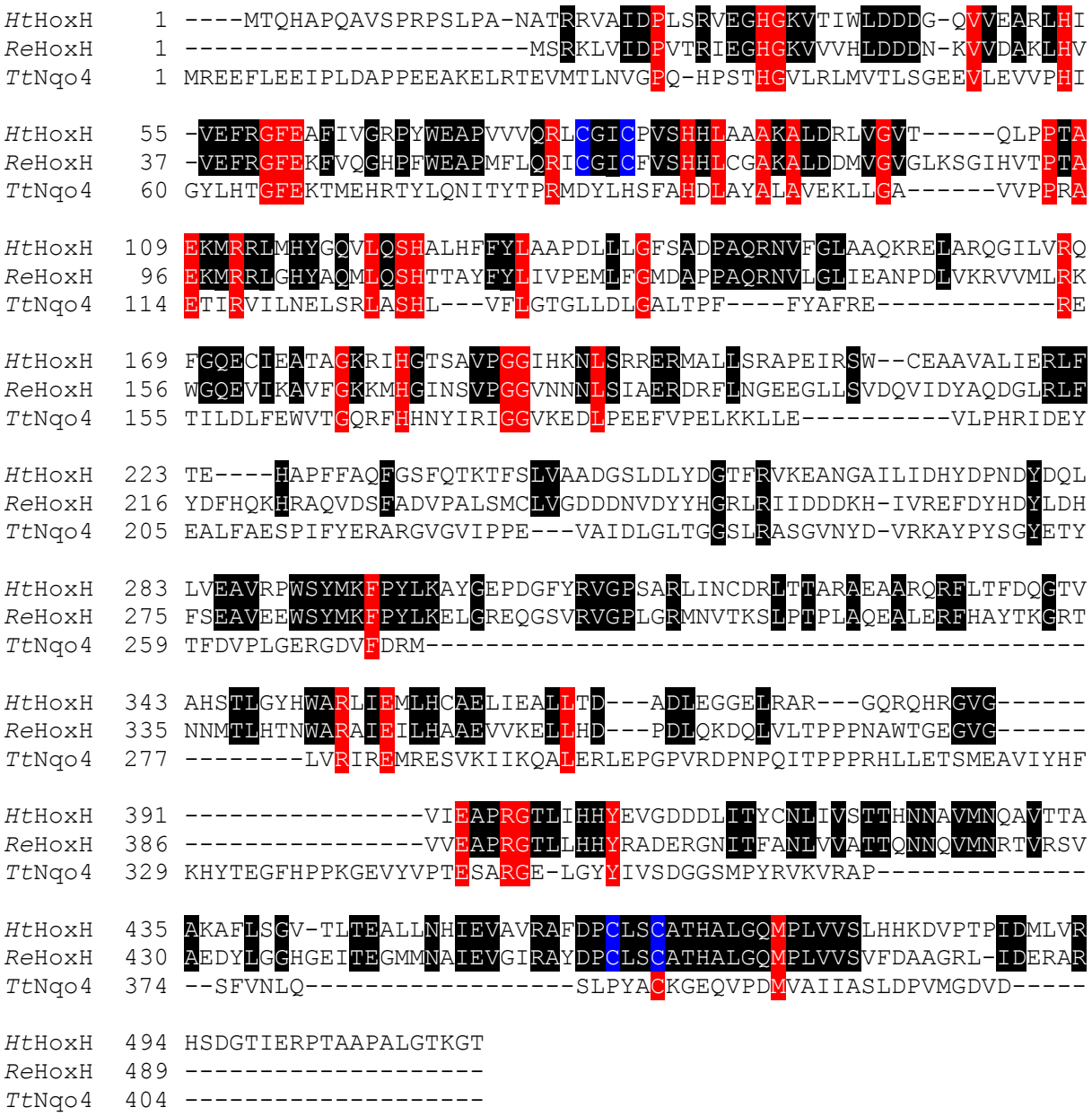

Figure A.4. Alignment of the *Ht*SH subunit HoxH with *Re*SH and the corresponding Nqo 4 subunit of Complex I from *Tt*. The color-code is the same as in Fig. A.1. Additionally, residues which are involved in the coordination of the [NiFe] catalytic center are shown in blue.

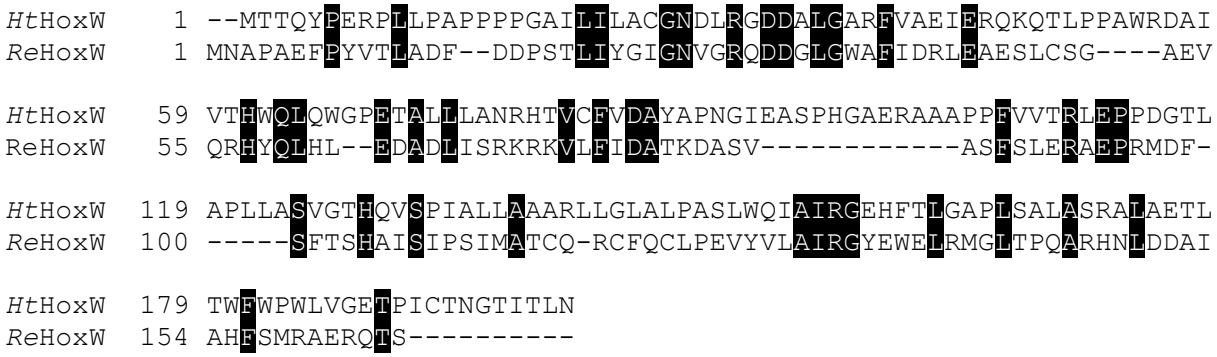

Figure A.5. Alignment of the *Ht*SH-specific endopedidases HoxW with *Re*SH. The color-code is the same as in Fig. A.1.

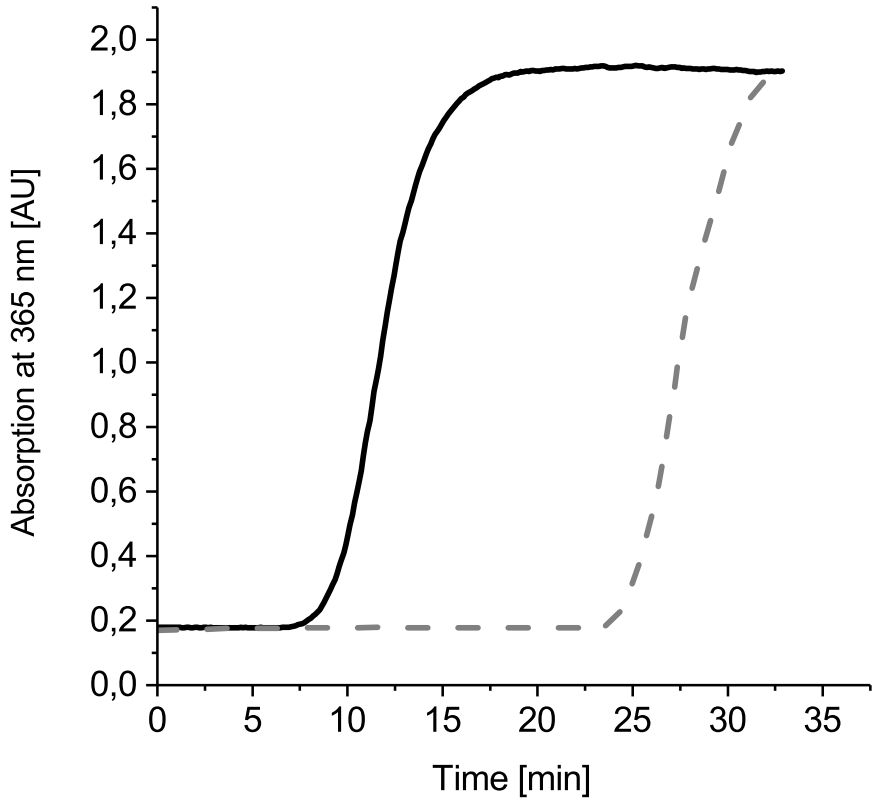

Figure A.6. Kinetics of H_2-dependent NAD^+-reduction (given in absorption units, AU, at 365 nm) catalyzed by *Ht*SH with (solid line) and without (dashed line) addition of FMN (2 μM). The assay was performed with 0.5 μM *Ht*SH at 50 °C in 50 mM bis-Tris, pH 6.5, supplemented with 1 mM NAD^+, 0.5 mM $NiCl_2$, 5 mM $MgSO_4$, and 0.75 mM TCEP.

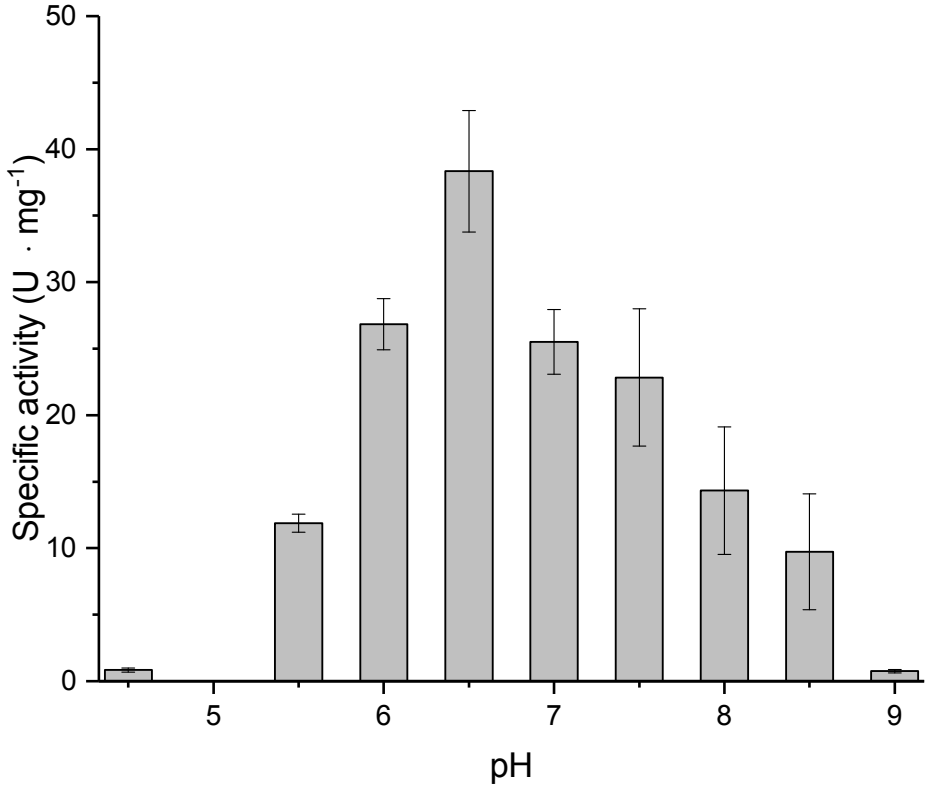

Figure A.7. pH dependence of the H_2-dependent NAD^+ reduction activity of purified *Ht*SH protein. The assay contained 60 nM *Ht*SH in one of the following buffers: 50 mM citrate, pH 4.5-7.0; 50 mM Tris/HCl, pH 7.5-8.0; 50 mM glycine, pH 8.5-9.0. Activity was measured in the presence of 1 mM NAD^+, 0.5 mM $NiCl_2$, 5 mM $MgSO_4$, 2 μM FMN, and 0.75 mM TCEP at a temperature of 50 °C.

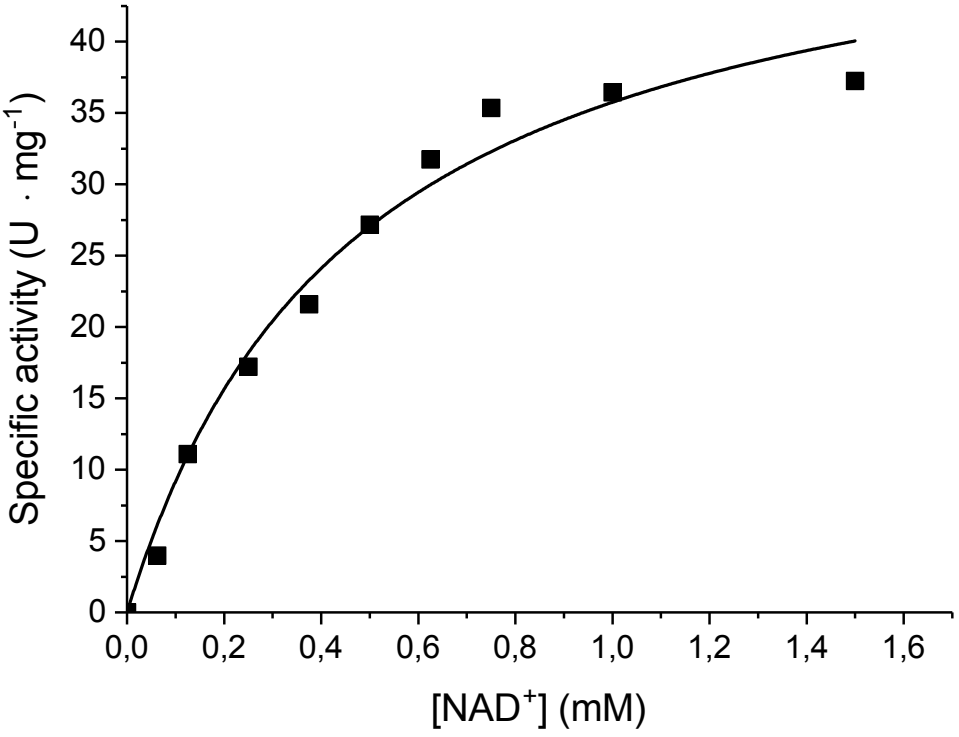

Figure A.8. Determination of the $K_M{}^{NAD^+}$ by measuring *Ht*SH-mediated H_2 oxidation at different NAD^+ concentrations. Activity was measured at a temperature of 50 °C in 50 mM H_2-saturated bis-Tris buffer, pH 6.5, 0.125-1.5 mM NAD^+, 0.5 mM $NiCl_2$, 5 mM $MgSO_4$, 2 μM FMN, and 0.75 mM TCEP. The depicted values represent the means derived from at least two measurements of one protein preparation. The Michaelis-Menten constant and the corresponding v_{max} value were calculated by non-linear regression. From three biological replicates, a K_M of 469 μM with a coefficient of variation (CV) of 9.8% was derived. The v_{max} value was 52.7 U mg^{-1}, with a CV of 3.4%, resulting in a turnover frequency (k_{cat}) of (155 ± 5) s^{-1} (assuming a molecular weight of 167.8 kDa for the heterotetrameric *Ht*SH).

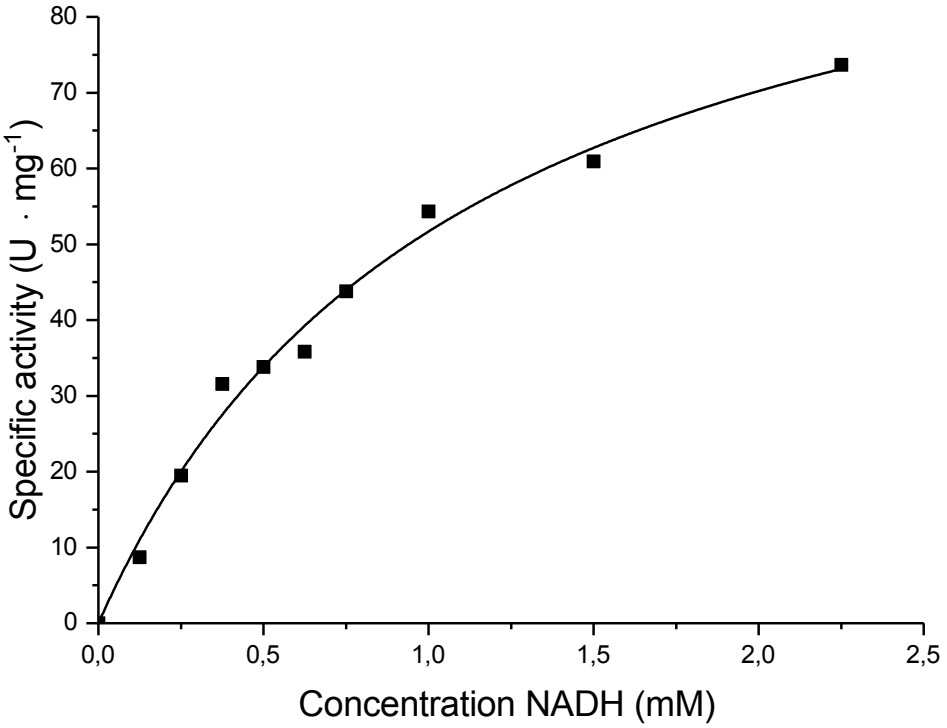

Figure A.9. Determination of the $K_M{}^{NADH}$ by measuring *Ht*SH-mediated benzyl viologen reduction activity (squares) at different NADH concentrations. Activity was measured at a temperature of 50 °C in 50 mM bis-Tris buffer, pH 6.5, containing 5 mM benzyl viologen, 0.125-2.25 mM NADH, 0.5 mM $NiCl_2$, 5 mM $MgSO_4$, 2 μM FMN, and 0.75 mM TCEP. The depicted values represent the means derived from at least two measurements of one protein preparation. The Michaelis-Menten constant and the corresponding v_{max} value were calculated by non-linear regression. From two biological replicates, a K_M 1.17 mM with a CV of 4.8% was derived. The v_{max} value was was 64.9 U mg^{-1}, with a CV of 3.5%, resulting in a turnover frequency (k_{cat}) of (179 ± 6) s^{-1} (assuming a molecular weight of 167.8 kDa for the heterotetrameric *Ht*SH).

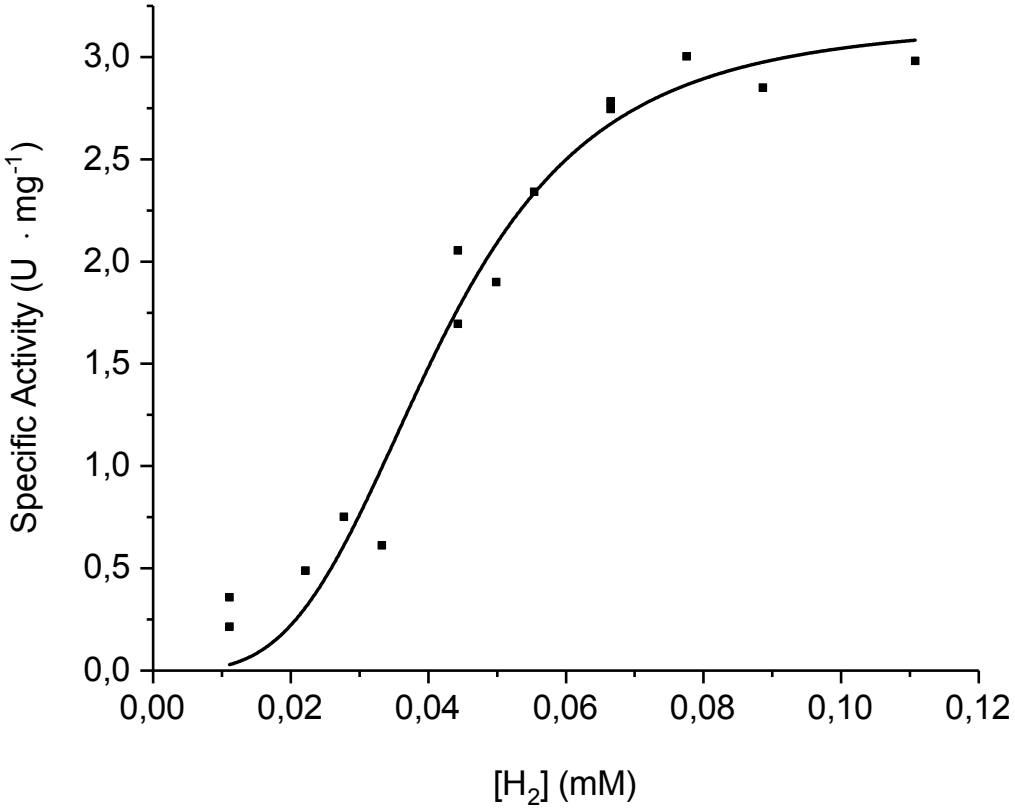

Figure A.10. Determination of the $K_M{}^{app}$ for H_2 by measuring *Ht*SH-mediated NAD^+ reduction (squares) at different H_2 concentrations. Activity was measured at a temperature of 50 °C in 50 mM bis-Tris buffer, pH 6.5, containing 1 mM NAD^+, 0.5 mM $NiCl_2$, 5 mM $MgSO_4$, 2 μM FMN, and 0.75 mM TCEP. The resulting data were not compatible with a classical Michaelis-Menten fit. Therefore, the $K_M{}^{app}$ for H_2 (ligand concentration, at which half the ligand-binding sites are occupied) was calculated by non-linear regression ($R^2 = 0.959$) and revealed to be 41.6 ± 2.5 μM with a Hill coefficient of 2.87 ± 0.8. The origin of the apparent cooperativity is unclear.

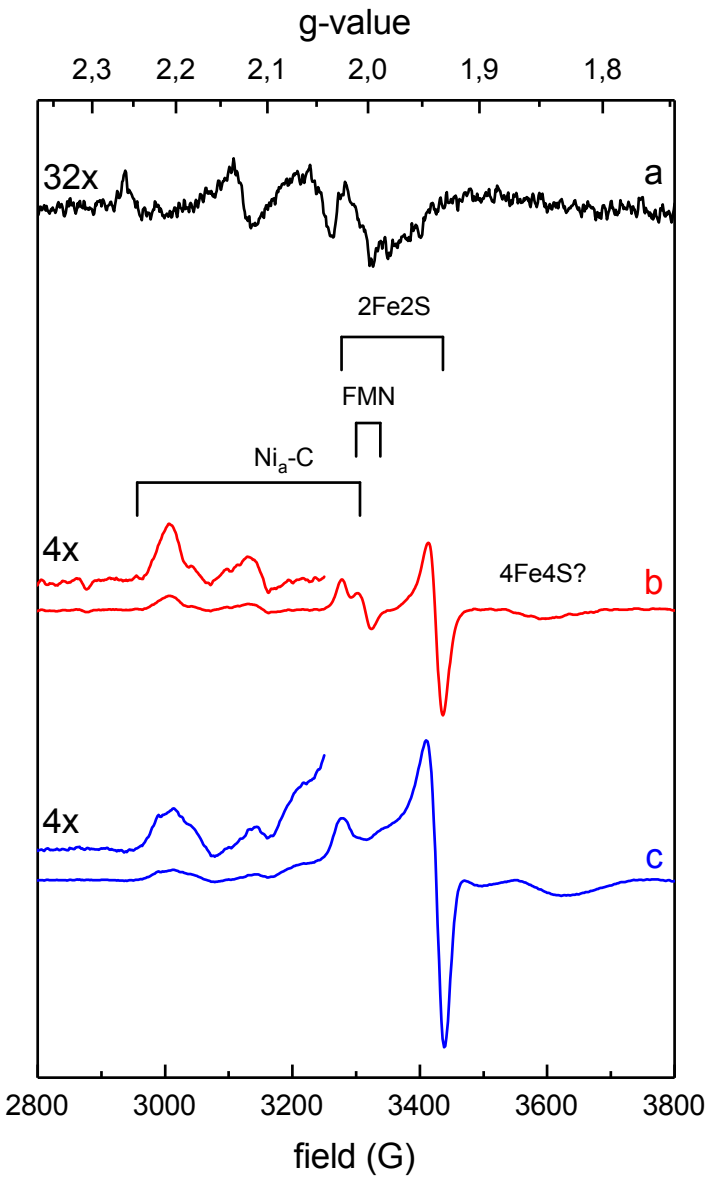

Figure A.11. EPR spectra of (a) as-isolated, (b) TCEP and NADH-reduced as well as (c) TCEP, NADH and H_2-reduced *Ht*SH. Spectra were recorded at 35 K (a), 10 K (b), and 6.5 K (c).

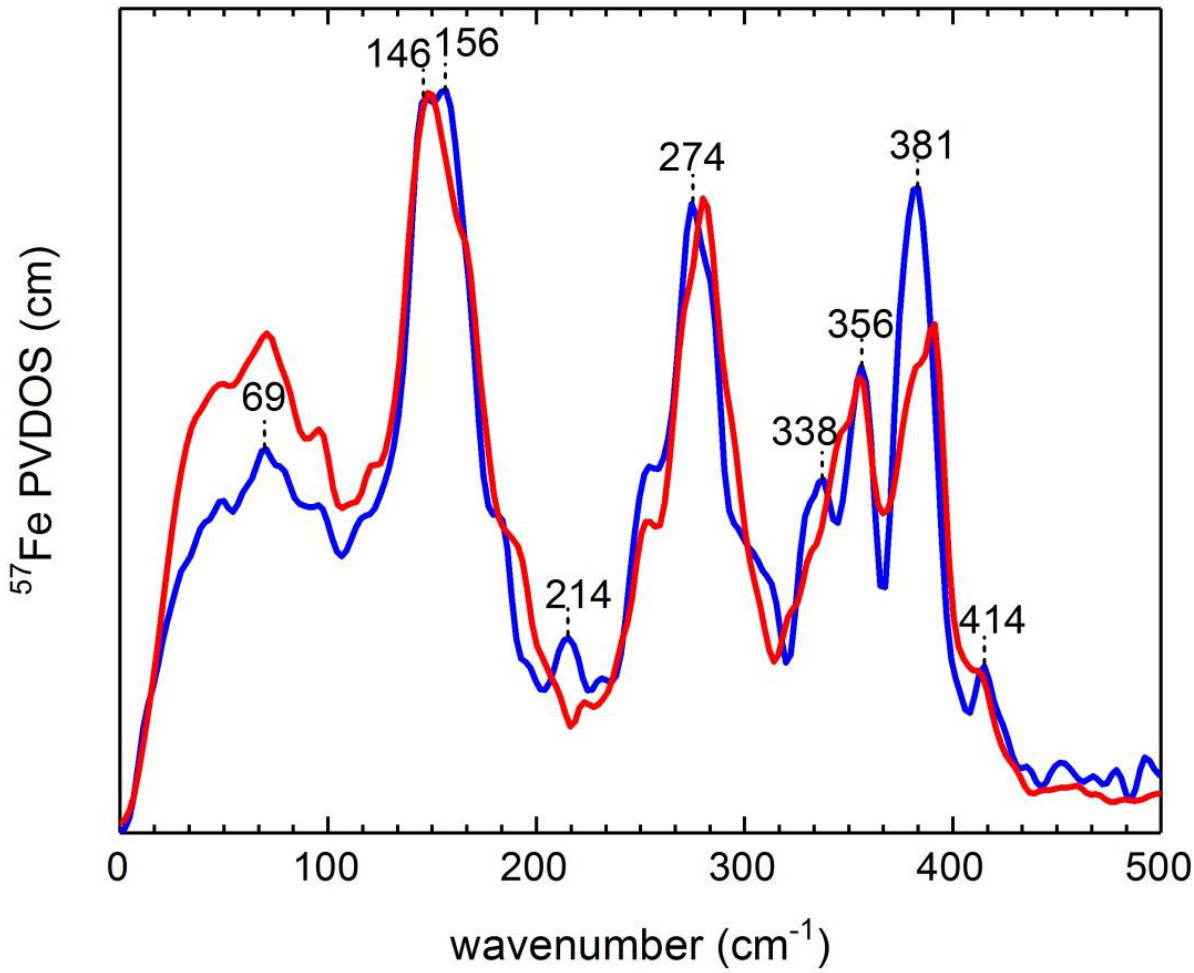

Figure A.12. NRVS-derived ^{57}Fe PVDOS in the spectral region reflecting Fe-S cluster modes. The spectra of as-isolated, oxidized *Ht*SH and *Re*SH (the latter was taken from ref.[132]) are shown as blue and red traces, respectively.

B. [NiFe] model complex

Table B.1. Crystal data and structure refinement for Ni(bmmp-daco)]SOFeBr$_2$ (**1**).

Empirical formula	C16 H31 Br2 Fe N3 Ni O S2	
Formula weight	619.94	
Temperature	150(2) K	
Wavelength	1.54184 Å	
Crystal system	Monoclinic	
Space group	P2/c	
Unit cell dimensions	a = 12.9892(3) Å	α = 90 °
	b = 9.3768(2) Å	β = 93.993(2) °
	c = 19.2510(4) Å	γ = 90 °
Volume	2339.02(9) Å^3	
Z	4	
Density (calculated)	1.760 Mg/m^3	
Absorption coefficient	11.728 mm^{-1}	
F(000)	1248	
Crystal size	0.45 x 0.04 x 0.03 mm^3	
Theta range for data collection	3.41 to 67.50 °	
Index ranges	-15<=h<=15, -10<=k<=11, -20<=l<=23	
Reflections collected	14520	
Independent reflections	4196 [R(int) = 0.0510]	
Completeness to theta = 67.50 °	99.6%	
Absorption correction	Semi-empirical from equivalents	
Max. and min. transmission	0.7198 and 0.0767	
Refinement method	Full-matrix least-squares on F^2	
Data / restraints / parameters	4196 / 0 / 240	
Goodness-of-fit on F^2	1.022	
Final R indices [I>2sigma(I)]	R1 = 0.0365, wR2 = 0.0933	
R indices (all data)	R1 = 0.0417, wR2 = 0.0977	
Largest diff. peak and hole	0.909 and -0.757 e·Å^{-3}	

Table B.2. Selected bond length (Å) and angles (°) for Ni(bmmp-daco)]SOFeBr$_2$ (**1**).

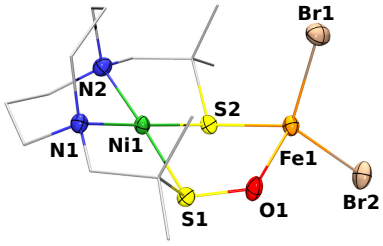

Br(1)-Fe(1)	2.4019(6)
Ni(1)-N(1)	1.970(3)
Ni(1)-N(2)	1.985(3)
Ni(1)-S(1)	2.1578(10)
Ni(1)-S(2)	2.1587(10)
Fe(1)-O(1)	2.012(3)
Fe(1)-S(2)	2.3741(9)
Fe(1)-Br(2)	2.4064(6)
S(1)-O(1)	1.562(2)
N(1)-Ni(1)-N(2)	91.31(12)
N(1)-Ni(1)-S(1)	89.04(9)
N(2)-Ni(1)-S(1)	176.61(10)
N(1)-Ni(1)-S(2)	176.53(9)
N(2)-Ni(1)-S(2)	90.20(9)
S(1)-Ni(1)-S(2)	89.64(4)
O(1)-Fe(1)-S(2)	89.27(7)
O(1)-Fe(1)-Br(1)	108.61(8)
S(2)-Fe(1)-Br(1)	119.26(3)
O(1)-Fe(1)-Br(2)	107.6(7)
S(2)-Fe(1)-Br(2)	109.48(3)
Br(1)-Fe(1)-Br(2)	118.12(3)
S(1)-O(1)-Fe(1)	121.31(13)
Ni(1)-S(2)-Fe(1)	101.30(4)

Table B.3. Crystal data and structure refinement for Ni(bmmp-daco)]SFeBr$_2$ (**2**).

Empirical formula	C16 H31 Br2 Fe N3 Ni S2	
Formula weight	562.88	
Temperature	150(2) K	
Wavelength	1.54184 Å	
Crystal system	Monoclinic	
Space group	P21/n	
Unit cell dimensions	a = 11.77290(10) Å	α = 90 °
	b = 13.21690(10) Å	β = 92.1640(10) °
	c = 12.93160(10) Å	γ = 90 °
Volume	2010.74(3) Å^3	
Z	4	
Density (calculated)	1.859 Mg/m^3	
Absorption coefficient	13.512 mm^{-1}	
F(000)	1128	
Crystal size	0.17 x 0.11 x 0.06 mm^3	
Theta range for data collection	4.79 to 67.49 °	
Index ranges	-14<=h<=9, -15<=k<=15, -15<=l<=15	
Reflections collected	7439	
Independent reflections	3615 [R(int) = 0.0230]	
Completeness to theta = 67.49 °	99.8%	
Absorption correction	Semi-empirical from equivalents	
Max. and min. transmission	0.4978 and 0.2072	
Refinement method	Full-matrix least-squares on F^2	
Data / restraints / parameters	3615 / 0 / 203	
Goodness-of-fit on F^2	0.851	
Final R indices [I>2sigma(I)]	R1 = 0.0245, wR2 = 0.0644	
R indices (all data)	R1 = 0.0265, wR2 = 0.0662	
Largest diff. peak and hole	0.555 and -0.374 e·Å^{-3}	

Table B.4. Selected bond length (Å) and angles (°) for Ni(bmmp-daco)]SFeBr$_2$ (**2**).

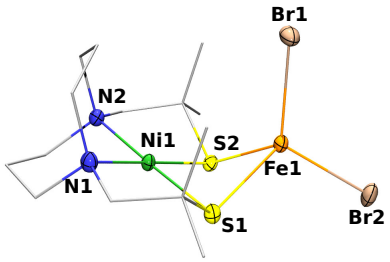

Br(1)-Fe(1)	2.3936(4)
Ni(1)-N(2)	1.974(2)
Ni(1)-N(1)	1.976(2)
Ni(1)-S(1)	2.1646(7)
Ni(1)-S(2)	2.1653(6)
Fe(1)-Br(2)	2.3772(4)
Fe(1)-S(1)	2.4036(6)
Fe(1)-S(2)	2.4099(7)
N(2)-Ni(1)-N(1)	91.74(8)
N(2)-Ni(1)-S(1)	177.64(6)
N(1)-Ni(1)-S(1)	90.44(6)
N(2)-Ni(1)-S(2)	90.40(6)
N(1)-Ni(1)-S(2)	177.62(7)
S(1)-Ni(1)-S(2)	87.41(2)
Br(2)-Fe(1)-Br(1)	116.180(18)
Br(2)-Fe(1)-S(1)	111.15(2)
Br(1)-Fe(1)-S(1)	118.36(2)
Br(2)-Fe(1)-S(2)	111.70(2)
Br(1)-Fe(1)-S(2)	116.51(2)
S(1)-Fe(1)-S(2)	76.85(2)
Ni(1)-S(1)-Fe(1)	84.40(2)
Ni(1)-S(2)-Fe(1)	84.23(2)

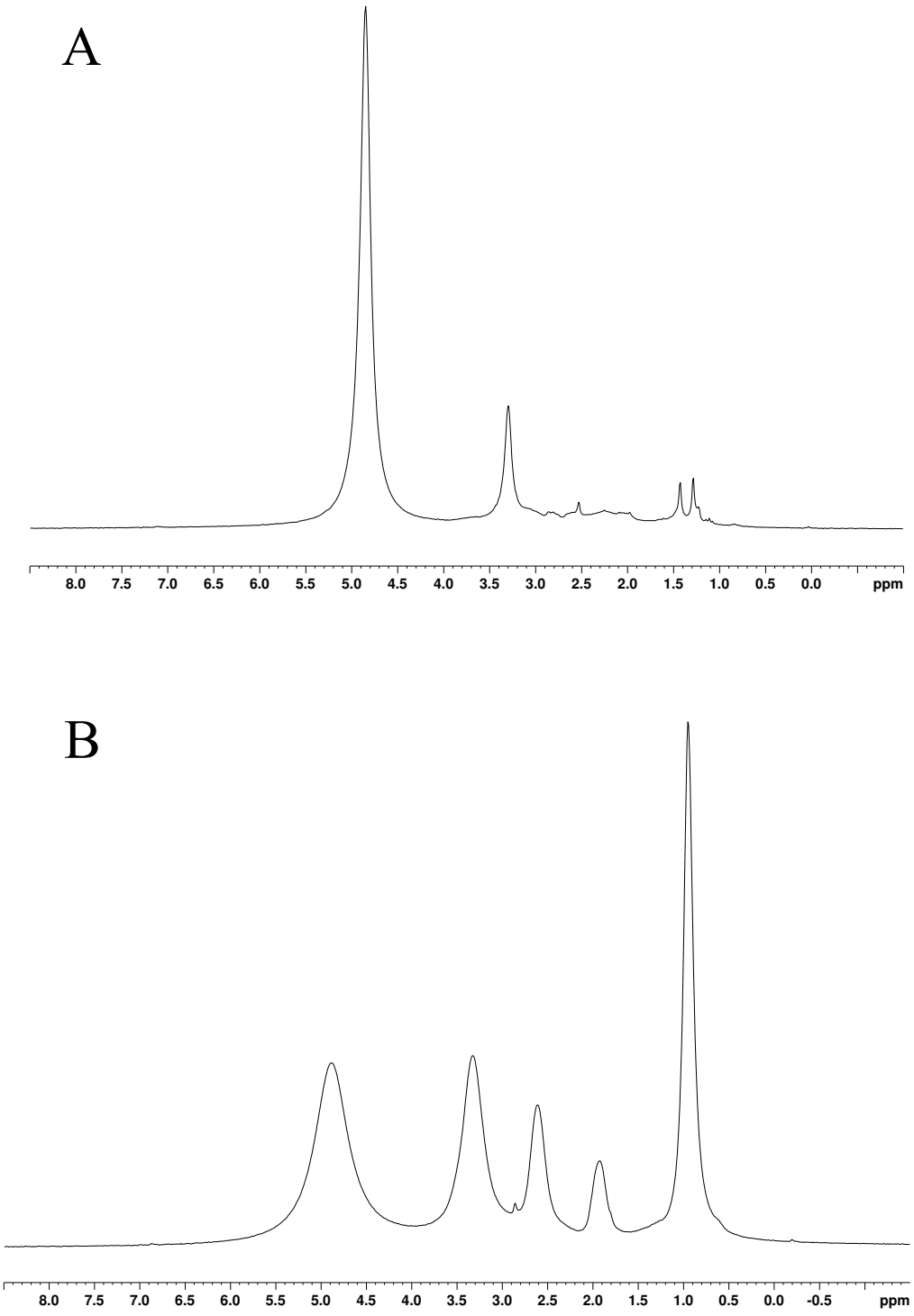

Figure B.1. A) ^{1}H NMR spectrum of [Ni(bmmp-daco)SO]$FeBr_2$ (**1**) and B) ^{1}H NMR spectrum of [Ni(bmmp-daco)]$FeBr_2$ (**2**) recorded at 200.13 MHz in methanol-d_4 at room temperature.

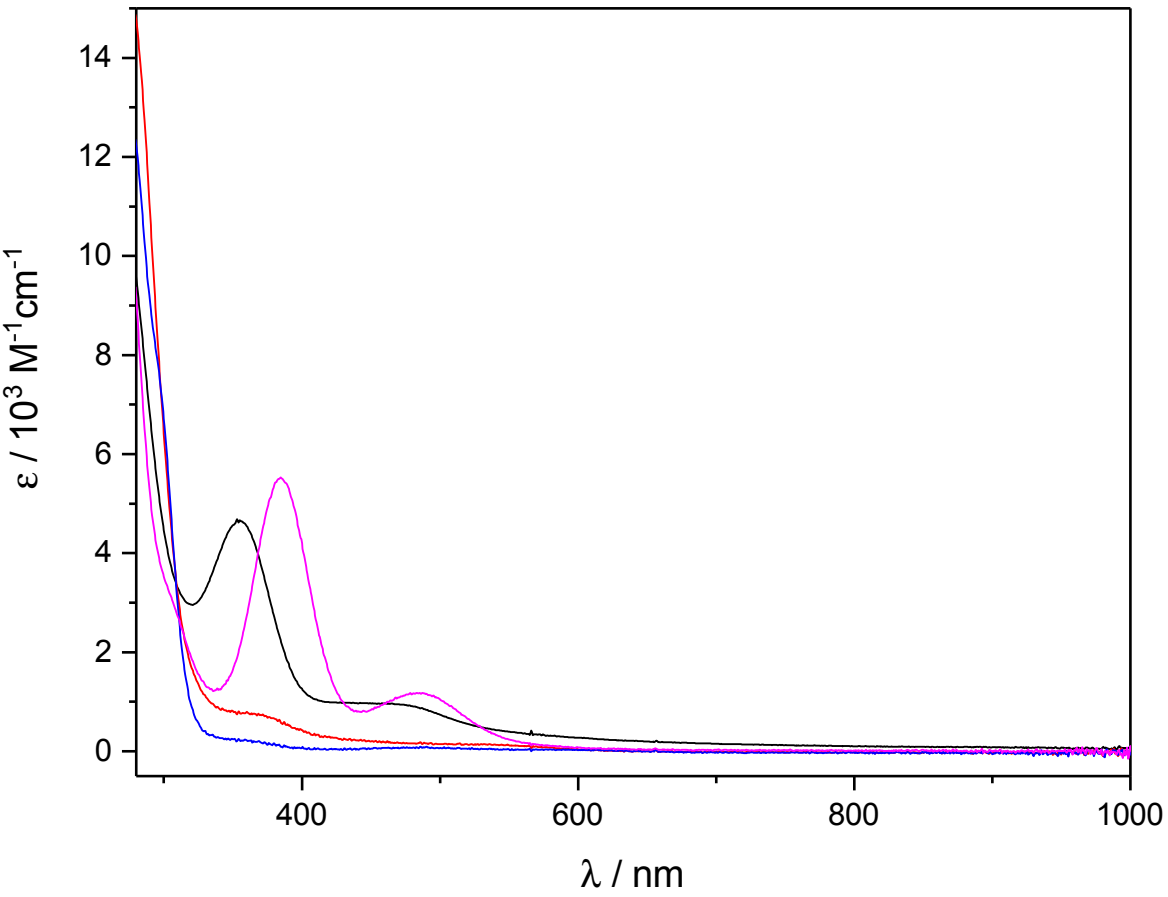

Figure B.2. UV-vis spectra of Ni(bmmp-daco) (blue), Ni(bmmp-daco)SO (pink), Ni(bmmp-daco)SOFeBr$_2$ **1** (black) and Ni(bmmp-daco)FeBr$_2$ **2** (red) in 40 μM acetonitrile solutions.

Table B.5. NBO-Analysis[205,271] of the bonding situation of the O atom in the Ni(bmmp-daco)SO.

NBO	atom	polarization	s-character	p-character	d-character
σ-bond	S	36.91%	19.10%	80.07%	0.82%
	O	63.09%	19.60%	79.61%	0.77%
lone pair	O	-	79.48%	20.51%	0.02%
lone pair	O	-	0.82%	98.88%	0.30%
lone pair	O	-	0.02%	99.67%	0.30%

Table B.6. NBO-Analysis[205,271] of the bonding situation of the O atom in complex **1**.

NBO	atom	polarization	s-character	p-character	d-character
σ-bond	S	34.28%	18.66%	80.28%	1.05%
	O	65.72%	22.26%	77.13%	0.59%
Dative-bond	Fe	8.72%	19.39%	27.10%	53.50%
	O	91.28	21.53%	78.35%	0.11%
lone pair	O	-	55.86%	44.03%	0.11%
lone pair	O	-	0.42%	99.34%	0.22%

Table B.7. NBO-Analysis[205,271] of the bonding situation of the S atom in complex **2**.

NBO	atom	polarization	s-character	p-character	d-character
Dative-bond	S	84.48%	18.78%	80.97%	0.24%
	Fe	15.52%	22.70%	29.73%	47.57%
Dative-bond	S	73.68%	13.18%	86.26%	0.55%
	Ni	26.32	26.12%	48.80%	25.08%
σ-bond	S	47.02%	19.15%	79.80%	1.01%
	C	52.98%	18.17%	81.77%	0.06%
lone pair	S	-	48.96%	50.99%	0.05%

Table B.8. Mayer Bond Order[155,156] of the S-O bond, NPA[204] charges of S, O, Ni and Fe atoms, and important bond distances (in Å) in Ni(bmmp-daco)SO, **1** and **2**.

Compound	MBO O-Fe	MBO Fe-S	MBO S-O	O charge	S(O)/S charge	Ni charge	Fe charge	S-O bond	S-Fe bond	O-Fe bond	Ni-Fe dist.
NiSO	-	-	1.52	-0.94	0.93/0.12	-	1.545	-	-	-	-
1	0.64	0.43	1.34	-0.84	0.90/0.06	0.02	0.36	1.563	2.348	2.041	3.589
2	-	0.43	-	-	0.12/0.12	0.06	0.08	-	2.386	-	2.964

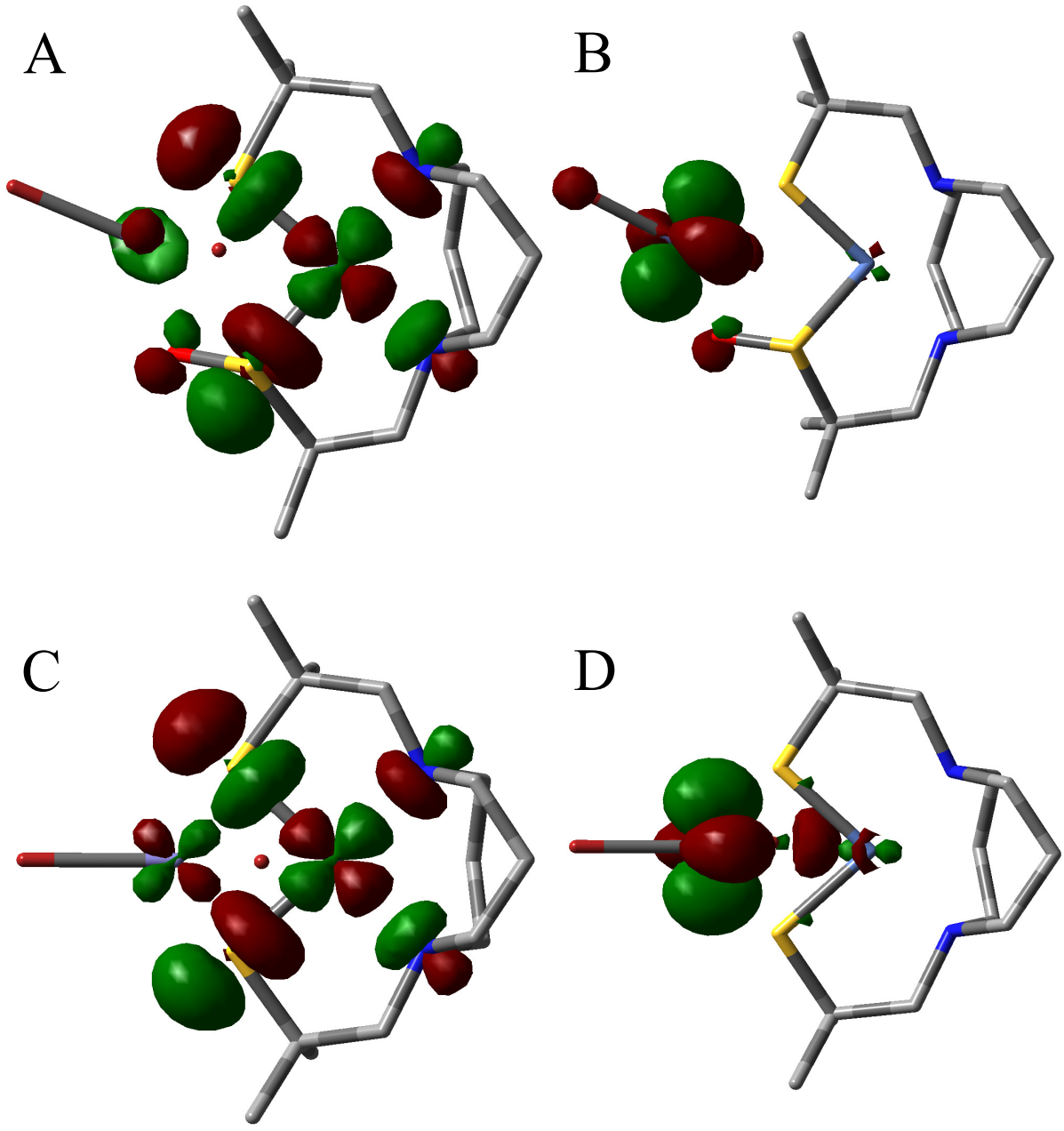

Figure B.3. SOMO (A) and LUMO (B) of Ni(bmmp-daco)SOFeBr$_2$ (**1**) and SOMO (C) and LUMO (D) of Ni(bmmp-daco)FeBr$_2$ (**2**).

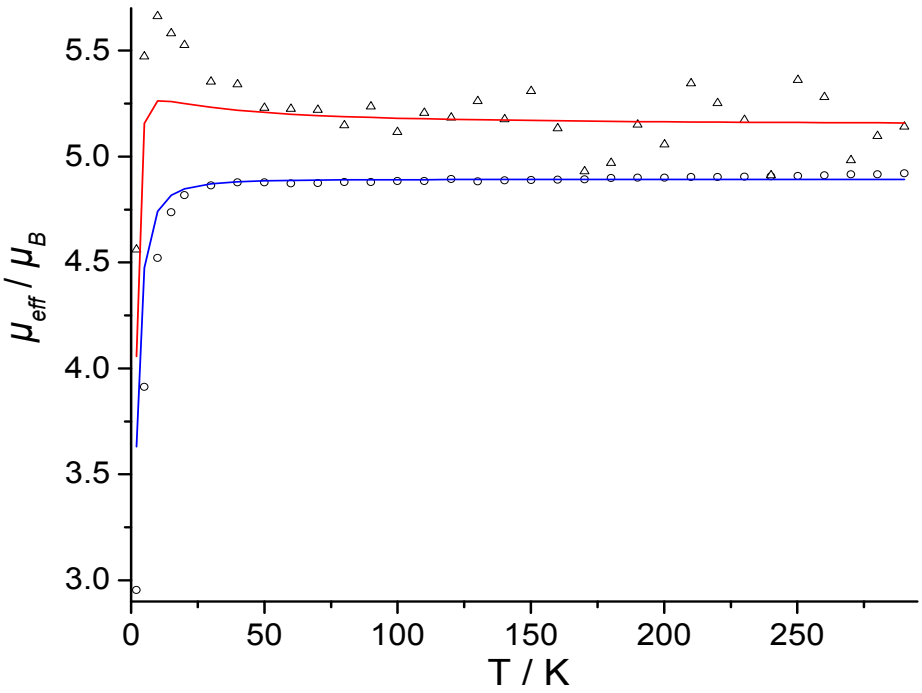

Figure B.4. Temperature dependence of the effective magnetic moment μ_{eff} of **1** (red) and **2** (blue); symbols represent experimental data. The solid lines are the result of spin Hamiltonian simulations for S=2 with parameters D = 6.5 cm^{-1}, E = 0, average <g> = 2.1 for **1**, and parameters D = 3.9 cm^{-1}, E = 0, average <g> = 2.0 for **2**. The increase of the data for **1** at low temperature is assigned to weak intermolecular interaction and was modeled with a mean field parameter 2zJ = 8 cm^{-1}.

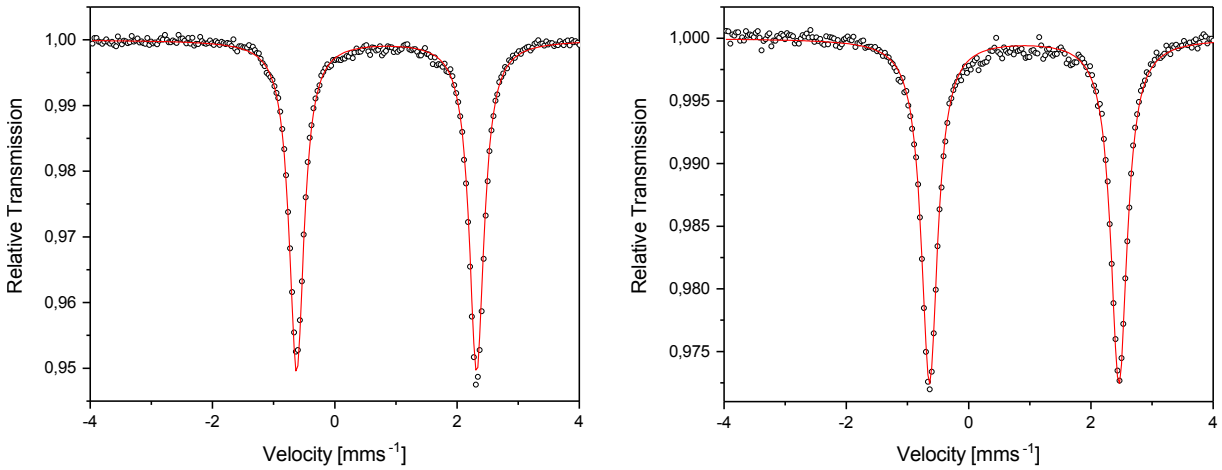

Figure B.5. ^{57}Fe Mößbauer spectra recorded at 80 K without applied field of **1** (left) and **2** (right); symbols: experimental data; solid lines: fitted Lorentzian quadrupole doublets with parameters given in the text.

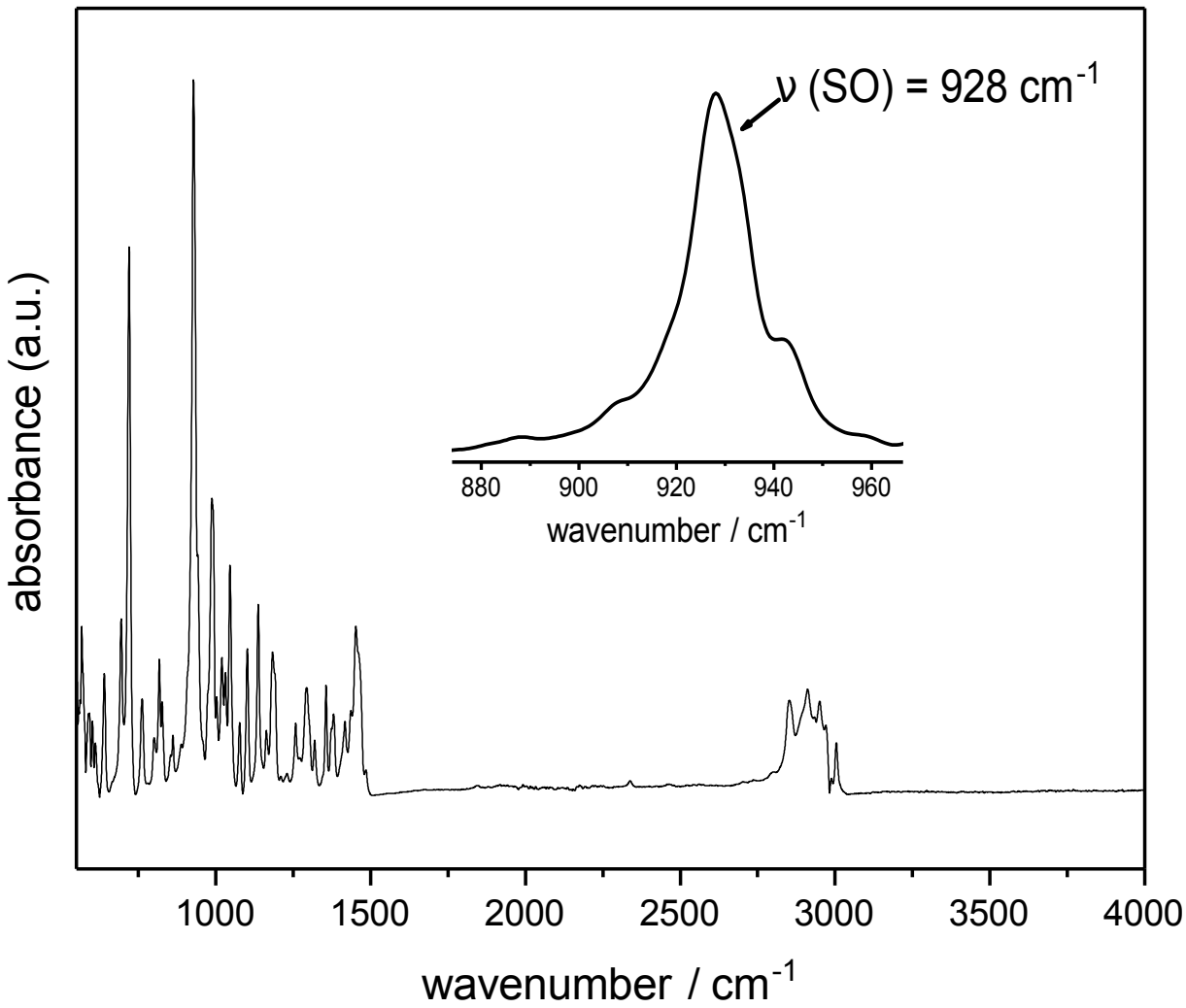

Figure B.6. Normalized IR spectrum (ATR-Diamond) of Ni(bmmp-daco)SO.

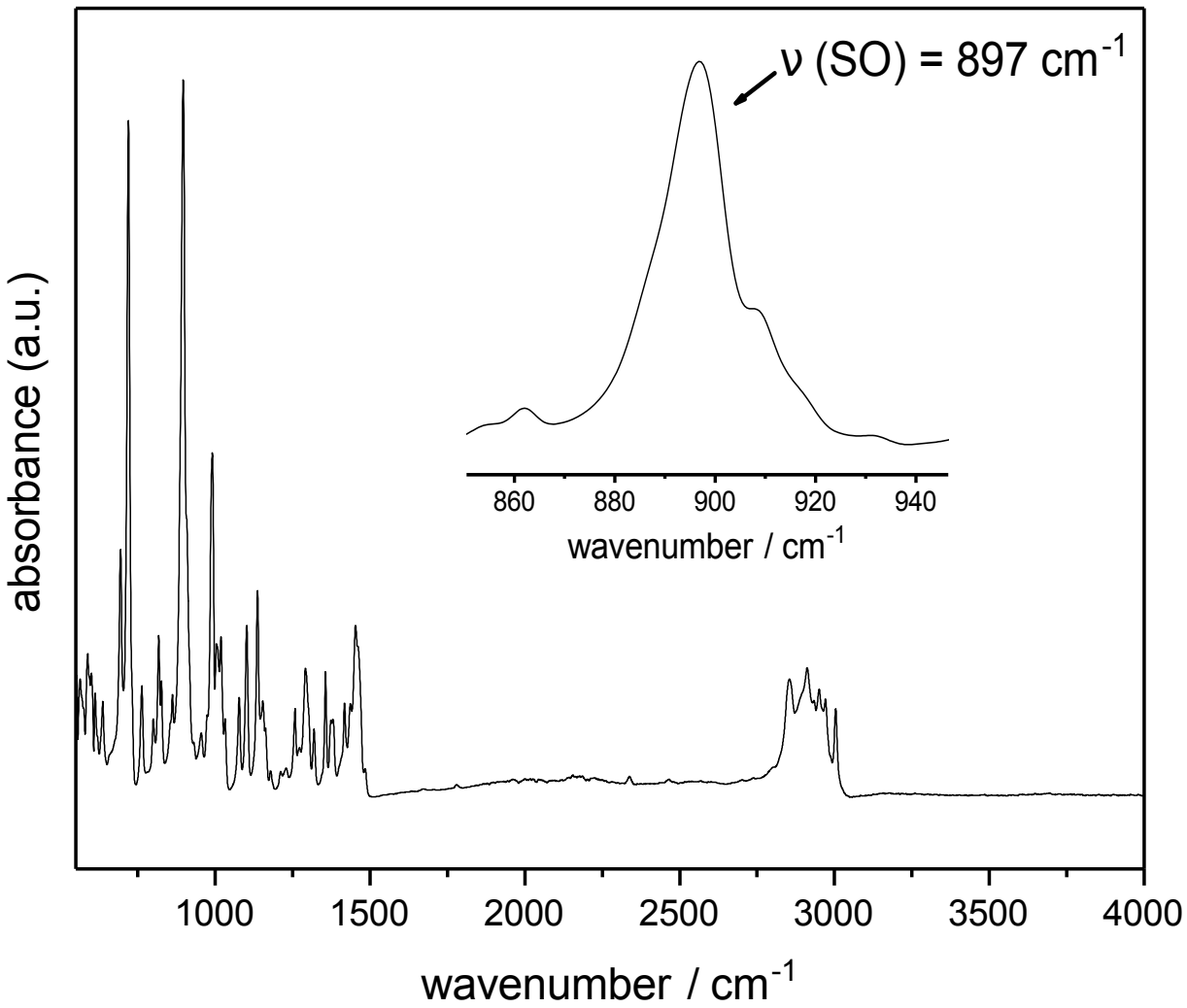

Figure B.7. Normalized IR spectrum (ATR-Diamond) of Ni(bmmp-daco)$S^{18}O$.

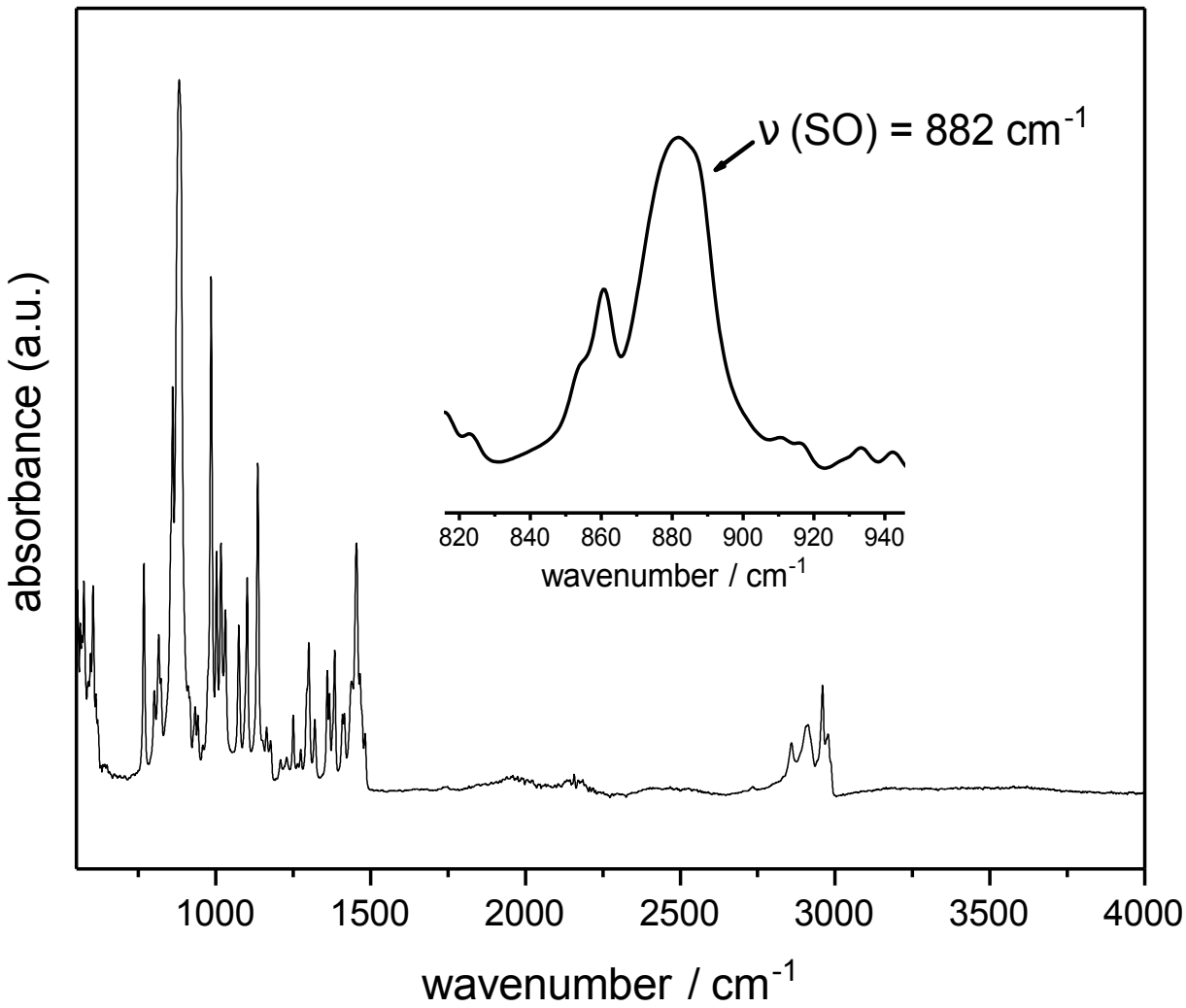

Figure B.8. Normalized IR spectrum (ATR-Diamond) of Ni(bmmp-daco)SOFeBr$_2$ (**1**).

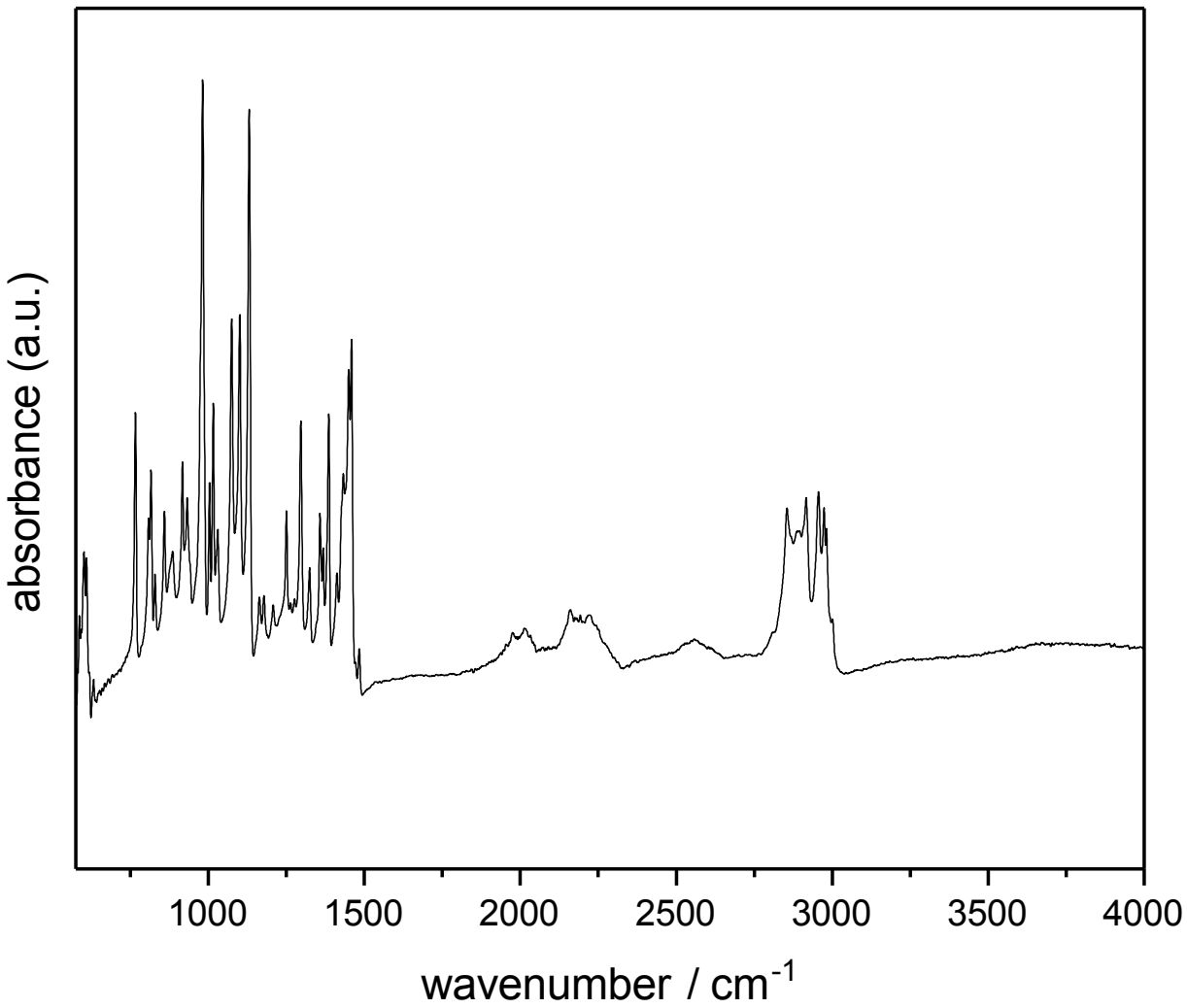

Figure B.9. Normalized IR spectrum (ATR-Diamond) of Ni(bmmp-daco)SFeBr$_2$ (**2**).

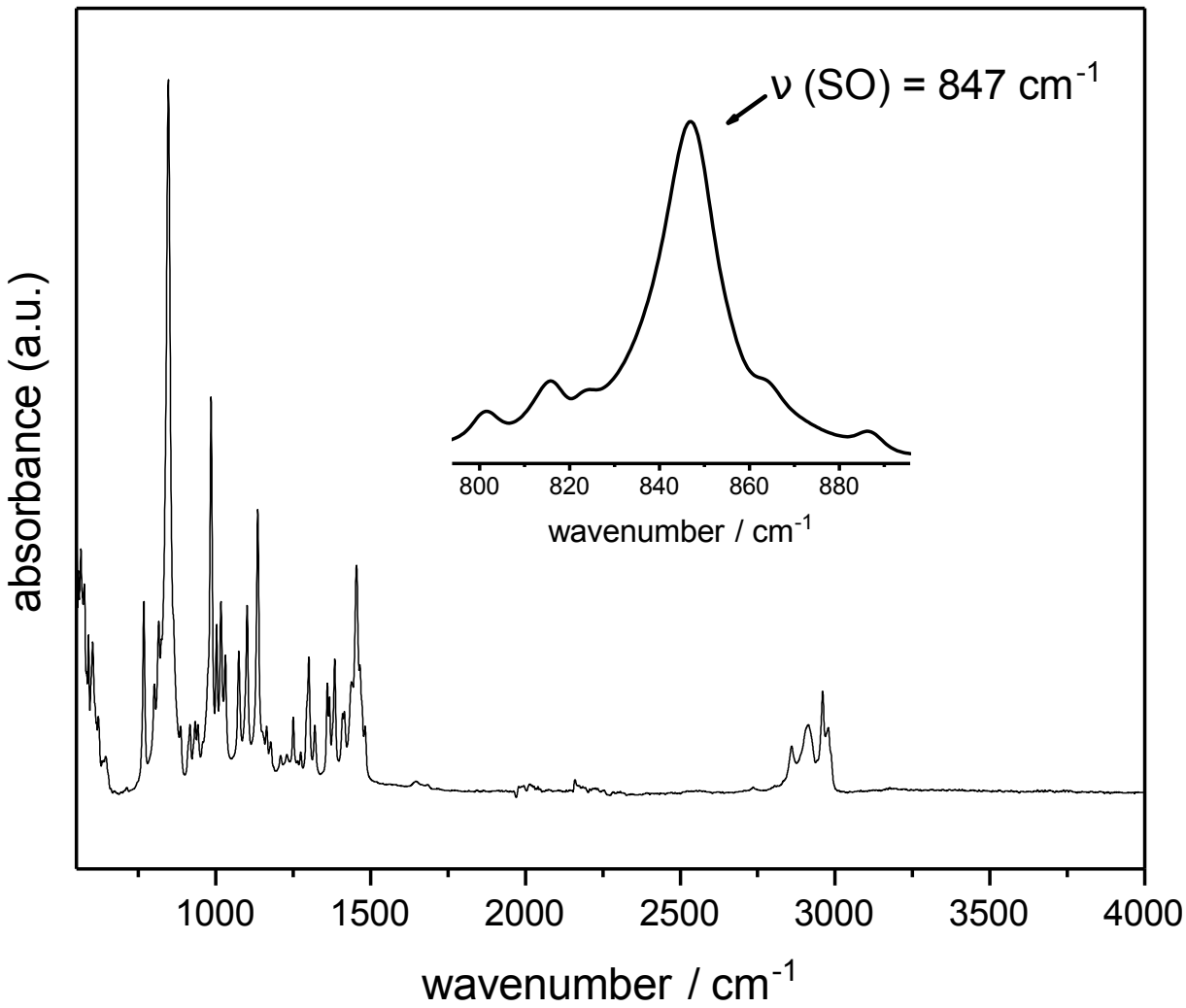

Figure B.10. Normalized IR spectrum (ATR-Diamond) of Ni(bmmp-daco)$S^{18}OFeBr_2$ (**3**).

C. Molybdenum cofactor

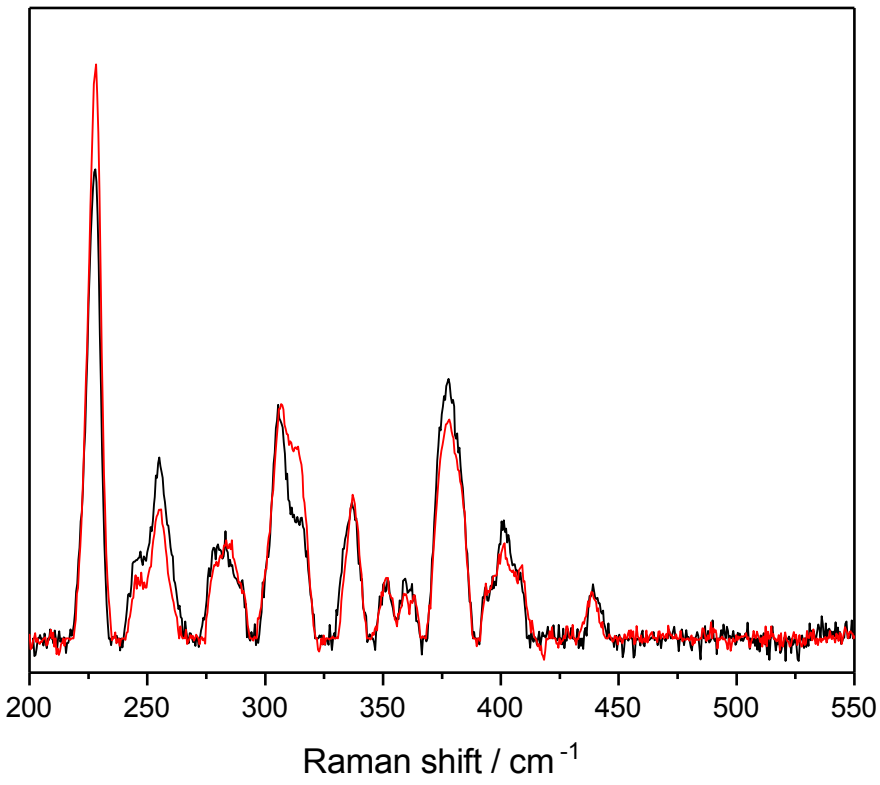

Figure C.1. FDH^{WT} reduced with 10 mM formate (black) and 10 mM d-formate (red). Spectra were acquired using 514 nm excitation at 70 K.

7. Bibliography

[1] A. Abou-Hamdan, P. Ceccaldi, H. Lebrette, O. Gutiérrez-Sanz, P. Richaud, L. Cournac, B. Guigliarelli, A. L. de Lacey, C. Léger, A. Volbeda, B. Burlat, and S. Dementin. A threonine stabilizes the NiC and NiR catalytic intermediates of NiFe-hydrogenase. *J. Biol. Chem.*, 290:8550–8558, 2015.

[2] S. Albracht. Nickel hydrogenases: in search of the active site. *Biochim. Biophys. Acta*, 1188:167–204, 1994.

[3] S. Albracht and A. de Jong. Bovine-heart NADH:ubiquinone oxidoreductase is a monomer with 8 Fe-S clusters and 2 FMN groups. *Biochim. Biophys. Acta*, 1318: 92–106, 1997.

[4] A. Alissandratos and C. J. Easton. Biocatalysis for the application of CO_2 as a chemical feedstock. *Beilstein J. Org. Chem.*, 11:2370–2387, 2015.

[5] P. Amendola, S. Antoniutti, G. Albertin, and E. Bordignon. Molecular hydrogen complexes. Preparation and reactivity of new ruthenium(II) and osmium(II) derivatives and a comparison along the iron triad. *Inorg. Chem.*, 29:318–324, 1990.

[6] J. Appel, S. Phunpruch, K. Steinmüller, and R. Schulz. The bidirectional hydrogenase of *Synechocystis* sp. PCC 6803 works as an electron valve during photosynthesis. *Arch. Microbiol.*, 173:333–338, 2000.

[7] N. M. Atherton. Principles of electron spin resonance. *Magn. Reson. Chem.*, 33: 698–698, 1995.

[8] M. J. Axley, A. Bock, and T. C. Stadtman. Catalytic properties of an *Escherichia coli* formate dehydrogenase mutant in which sulfur replaces selenium. *PNAS*, 88: 8450–8454, 1991.

[9] T. Ayers, R. Turk, C. Lane, J. Goins, D. Jameson, and S. J. Slattery. Tuning redox and spin state properties of Fe(II) N-heterocyclic complexes via electronic/steric influence on metalâligand binding. *Inorg. Chim. Acta*, 357:202–206, 2004.

[10] T. Baba, T. Ara, M. Hasegawa, Y. Takai, Y. Okumura, M. Baba, K. A. Datsenko, M. Tomita, B. L. Wanner, and H. Mori. Construction of *Escherichia coli* K-12 in-frame, single-gene knockout mutants: the Keio collection. *Mol. Syst. Biol.*, 2: 1–11, 2006.

[11] K. A. Bagley, E. C. Duin, W. Roseboom, S. P. J. Albracht, and W. H. Woodruff. Infrared-detectable group senses changes in charge density on the nickel center in hydrogenase from *Chromatium vinosum*. *Biochemistry*, 34:5527–5535, 1995.

[12] G. A. Bain and J. F. Berry. Diamagnetic Corrections and Pascal's Constants. *J. Chem. Educ.*, 85:532–536, 2008.

[13] J. L. Barilone, H. Ogata, W. Lubitz, and M. van Gastel. Structural differences between the active sites of the Ni-A and Ni-B states of the NiFe hydrogenase: an approach by quantum chemistry and single crystal ENDOR spectroscopy. *PCCP*, 17:16204–16212, 2015.

[14] J. Barker. Mass spectrometry - Analytical Chemistry by Open Learning. 2nd Edition by J. Wiley and Sons. 1999.

[15] A. D. Becke. Density–functional thermochemistry. III. The role of exact exchange. *J. Chem. Phys.*, 98:5648–5652, 1993.

[16] J. Benemann. Hydrogen biotechnology: Progress and prospects. *Nat. Biotechnol.*, 14:1101–1103, 1996.

[17] B. Bennett, N. Benson, A. G. McEwan, and R. C. Bray. Multiple States of the Molybdenum Centre of Dimethylsulphoxide Reductase from *Rhodobacter Capsulatus* Revealed by EPR Spectroscopy. *Eur. J. Biochem.*, 225:321–331, 1994.

[18] A. K. Bhattacharya and A. G. Hortmann. General synthesis of 1,3-dithiol-2-ones. *J. Org. Syn. Chem.*, 39:95–97, 1974.

[19] J. S. Blanchard and W. W. Cleland. Kinetic and chemical mechanisms of yeast formate dehydrogenase. *Biochemistry*, 19:3543–3550, 2002.

[20] B. Bleijlevens, F. A. van Broekhuizen, A. L. de Lacey, W. Roseboom, V. M. Fernández, and S. P. J. Albracht. The activation of the NiFe-hydrogenase from *Allochromatium vinosum*. An infrared spectro-electrochemical study. *J. Biol. Inorg. Chem.*, 9:743–752, 2004.

[21] N. Böhmer, T. Hartmann, and S. Leimkühler. The chaperone FdsC for *Rhodobacter capsulatus* formate dehydrogenase binds the bis-molybdopterin guanine dinucleotide cofactor. *FEBS Lett.*, 588:531–537, 2014.

[22] J. C. Boyington. Crystal Structure of Formate Dehydrogenase H: Catalysis Involving Mo, Molybdopterin, Selenocysteine, and an Fe4S4 Cluster. *Science*, 275:1305–1308, 1997.

[23] D. Brazzolotto, M. Gennari, N. Queyriaux, T. R. Simmons, J. Pécaut, S. Demeshko, F. Meyer, M. Orio, V. Artero, and C. Duboc. Nickel-centred proton reduction catalysis in a model of NiFe hydrogenase. *Nat. Chem.*, 8:1054–1060, 2016.

[24] M. Brecht, M. van Gastel, T. Buhrke, B. Friedrich, and W. Lubitz. Direct detection of a hydrogen ligand in the NiFe center of the regulatory H_2-sensing hydrogenase from *Ralstonia eutropha* in its reduced state by HYSCORE and ENDOR spectroscopy. *J. Am. Chem. Soc.*, 125:13075–13083, 2003.

[25] R. Breglia, M. A. Ruiz-Rodriguez, A. Vitriolo, R. F. Gonzàlez-Laredo, L. de Gioia, C. Greco, and M. Bruschi. Theoretical insights into NiFe-hydrogenases oxidation resulting in a slowly reactivating inactive state. *J. Biol. Inorg. Chem.*, 22:137–151, 2017.

[26] M. Bruschi, G. Zampella, P. Fantucci, and L. Degiogia. DFT investigations of models related to the active site of [NiFe] and [Fe] hydrogenases. *Coord. Chem. Rev.*, 249:1620–1640, 2005.

[27] M. Bruschi, M. Tiberti, A. Guerra, and L. de Gioia. Disclosure of key stereoelectronic factors for efficient H_2 binding and cleavage in the active site of NiFe-hydrogenases. *J. Am. Chem. Soc.*, 136:1803–1814, 2014.

[28] F. O. Bryant and M. W. W. Adams. Characterization of hydrogenase from the hyperthermophilic archaebacterium, *Pyrococcus furiosus*. *J. Biol. Chem.*, 164:5070–5079, 1989.

[29] T. Buhrke, O. Lenz, N. Krauss, and B. Friedrich. Oxygen tolerance of the H_2-sensing NiFe hydrogenase from *Ralstonia eutropha* H16 is based on limited access of oxygen to the active site. *J. Biol. Chem.*, 280:23791–23796, 2005.

[30] R. M. Buonomo, I. Font, M. J. Maguire, J. H. Reibenspies, T. Tuntulani, and M. Y. Darensbourg. Study of Sulfinate and Sulfenate Complexes Derived from the Oxygenation of Thiolate Sulfur in [1,5-Bis(2-mercapto-2-methylpropyl)-1,5-diazacyclooctanato(2-)]nickel(II). *J. Am. Chem. Soc.*, 117:963–973, 1995.

[31] T. Burgdorf, O. Lenz, T. Buhrke, E. van der Linden, A. K. Jones, S. P. J. Albracht, and B. Friedrich. NiFe-hydrogenases of *Ralstonia eutropha* H16: modular enzymes for oxygen-tolerant biological hydrogen oxidation. *J. Mol. Microbiol. Biotechnol.*, 10:181–196, 2005.

[32] T. Burgdorf, E. van der Linden, M. Bernhard, Q. Y. Yin, J. W. Back, A. F. Hartog, A. O. Muijsers, C. G. de Koster, S. P. J. Albracht, and B. Friedrich. The soluble NAD^+-Reducing NiFe-hydrogenase from *Ralstonia eutropha* H16 consists of six subunits and can be specifically activated by NADPH. *J. Bacteriol.*, 187:3122–3132, 2005.

[33] I. Bürstel, E. Siebert, S. Frielingsdorf, I. Zebger, B. Friedrich, and O. Lenz. CO synthesized from the central one-carbon pool as source for the iron carbonyl in O_2-tolerant NiFe-hydrogenase. *PNAS*, 113:14722–14726, 2016.

[34] M. D. Butts, B. L. Scott, and G. J. Kubas. Syntheses and Structures of Alkyl and Aryl Halide Complexes of the Type $[(PiPr_3)_2PtH(\eta^1\text{-}XR)]BAr_f$ and Analogues with Et_2O, THF, and H_2 Ligands. Halide-to-Metal π Bonding in Halocarbon Complexes. *J. Am. Chem. Soc.*, 118:11831–11843, 1996.

[35] R. Cammack, D. S. Patil, E. Hatchikian, and V. M. Fernández. Nickel and iron-sulphur centres in *Desulfovibrio gigas* hydrogenase: ESR spectra, redox properties and interactions. *Biochim. Biophys. Acta*, 912:98–109, 1987.

[36] N. M. F. S. A. Cerqueira, P. A. Fernandes, P. J. Gonzalez, J. J. G. Moura, and M. J. Ramos. The sulfur shift: an activation mechanism for periplasmic nitrate reductase and formate dehydrogenase. *Inorg. Chem.*, 52:10766–10772, 2013.

[37] G. M. Chambers, M. T. Huynh, Y. Li, S. Hammes-Schiffer, T. B. Rauchfuss, E. Reijerse, and W. Lubitz. Models of the Ni-L and Ni-SI_a States of the NiFe-Hydrogenase Active Site. *Inorg. Chem.*, 55:419–431, 2016.

[38] P. Chandrasekaran and J. P. Donahue. Synthesis of 4,5-Dimethyl-1,3-dithiol-2-one. *Org. Synth.*, 86:333–343, 2009.

[39] P. Chandrasekaran, K. Arumugam, U. Jayarathne, L. M. Pérez, J. T. Mague, and J. P. Donahue. Synthesis, structures, and properties of mixed dithiolene-carbonyl and dithiolene-phosphine complexes of tungsten. *Inorg. Chem.*, 48:2103–2113, 2009.

[40] S. K. Chandrayan, P. M. McTernan, R. C. Hopkins, J. Sun, F. E. Jenney, and M. W. W. Adams. Engineering hyperthermophilic archaeon *Pyrococcus furiosus* to overproduce its cytoplasmic NiFe-hydrogenase. *J. Biol. Chem.*, 287:3257–3264, 2012.

[41] J. Christensen, C. H. amd Rass-Hansen, C. C. Marsden, E. Taarning, and K. Egeblad. The Renewable Chemicals Industry. *ChemSusChem*, 1:283–289, 2008.

[42] A. Ciaccafava, D. Tombolelli, L. Domnik, J. Fesseler, J.-H. Jeoung, H. Dobbek, M. A. Mroginski, I. Zebger, and P. Hildebrandt. When the inhibitor tells more than the substrate: The cyanide-bound state of a carbon monoxide dehydrogenase. *Chem. Sci.*, 7:3162–3171, 2016.

[43] T. R. Cook, D. K. Dogutan, S. Y. Reece, Y. Surendranath, T. S. Teets, and D. G. Nocera. Solar Energy Supply and Storage for the Legacy and Nonlegacy Worlds. *Chem. Rev.*, 110:6474–6502, 2010.

[44] J. M. Coremans, J. W. van der Zwaan, and S. P. J. Albracht. Distinct redox behaviour of prosthetic groups in ready and unready hydrogenase from *Chromatium vinosum*. *Biochim. Biophys. Acta*, 1119:157–168, 1992.

[45] L. Cournac, G. Guedeney, G. Peltier, and P. M. Vignais. Sustained photoevolution of molecular hydrogen in a mutant of *Synechocystis* sp. strain PCC 6803 deficient in the type I NADPH-dehydrogenase complex. *J. Bacteriol.*, 186:1737–1746, 2004.

[46] L. Cournac, G. Guedeney, G. Peltier, and P. M. Vignais. The bidirectional NiFe-hydrogenase in *Synechocystis* sp. PCC 6803 is reduced by flavodoxin and ferredoxin and is essential under mixotrophic, nitrate-limiting conditions. *J. Biol. Chem.*, 289: 1930–1937, 2014.

[47] J. A. Cracknell, A. F. Wait, O. Lenz, B. Friedrich, and F. A. Armstrong. A kinetic and thermodynamic understanding of O_2 tolerance in NiFe-hydrogenases. *PNAS*, 106:20681–20686, 2009.

[48] J. N. Daniels, M. M. Wuebbens, K. V. Rajagopalan, and H. Schindelin. Crystal structure of a molybdopterin synthase-precursor Z complex: insight into its sulfur transfer mechanism and its role in molybdenum cofactor deficiency. *Biochemistry*, 47:615–626, 2008.

[49] M. Y. Darensbourg and W. Weigand. Sulfoxygenation of Active Site Models of [NiFe] and [FeFe] Hydrogenases - A Commentary on Possible Chemical Models of Hydrogenase Enzyme Oxygen Sensitivity. *Eur. J. Inorg. Chem.*, 2011:994–1004, 2011.

[50] M. Y. Darensbourg, E. J. Lyon, and J. J. Smee. The bio-organometallic chemistry of active site iron in hydrogenases. *Coord. Chem. Rev.*, 206-207:533–561, 2000.

[51] G. Davidson, S. B. Choudhury, Z. Gu, K. Bose, W. Roseboom, S. P. J. Albracht, and M. J. Maroney. Structural Examination of the Nickel Site in *Chromatium vinosum* Hydrogenase: Redox State Oscillations and Structural Changes Accompanying Reductive Activation and CO Binding. *Biochemistry*, 39:7468–7479, 2000.

[52] A. L. de Lacey, E. C. Hatchikian, A. Volbeda, M. Frey, J. C. Fontecilla-Camps, and V. M. Fernández. Infrared-Spectroelectrochemical Characterization of the [NiFe] Hydrogenase of *Desulfovibrio gigas*. *J. Am. Chem. Soc.*, 119:7181–7189, 1997.

[53] A. L. de Lacey, V. M. Fernández, M. Rousset, and R. Cammack. Activation and inactivation of hydrogenase function and the catalytic cycle: spectroelectrochemical studies. *Chem. Rev.*, 107:4304–4330, 2007.

[54] J. Dernedde, T. Eitinger, N. Patenge, and B. Friedrich. *hyp* Gene Products in *Alcaligenes eutrophus* are part of a Hydrogenase-Maturation System. *Eur. J. Biochem.*, 235:351–358, 1996.

[55] S. Ding, P. Ghosh, A. M. Lunsford, N. Wang, N. Bhuvanesh, M. B. Hall, and M. Y. Darensbourg. Hemilabile Bridging Thiolates as Proton Shuttles in Bioinspired H_2 Production Electrocatalysts. *J. Am. Chem. Soc.*, 138:12920–12927, 2016.

[56] P. M. A. Dirac. The Quantum Theory of Absorption and Emission. *Proc. Royal Soc. Lond.*, 114:243–265, 1927.

[57] L. Ducháčková, D. Schröder, and J. Roithová. Effect of the carboxylate shift on the reactivity of zinc complexes in the gas phase. *Inorg. Chem.*, 50:3153–3158, 2011.

[58] A. Erkens, K. Schneider, and A. Müller. The NAD-linked soluble hydrogenase from *Alcaligenes eutrophus* H16: detection and characterization of EPR signals deriving from nickel and flavin. *J. Biol. Inorg. Chem.*, 1:99–110, 1996.

[59] D. F. Evans. The Determination of the Pararnagnetic Susceptibility of Substances in Solution by Nuclear Magnetic Resonance. *J. Chem. Soc*, 0:2003–2005, 1959.

[60] P. J. Farmer, T. Solouki, D. K. Mills, T. Soma, D. H. Russell, J. H. Reibenspies, and M. Y. Darensbourg. Isotopic labeling investigation of the oxygenation of nickel-bound thiolates by molecular oxygen. *J. Am. Chem. Soc.*, 114:4601–4605, 1992.

[61] V. M. Fernández, E. C. Hatchikian, and R. Cammack. Properties and reactivation of two different deactivated forms of *Desulfovibrio gigas* hydrogenase. *Biochim. Biophys. Acta*, 832:69–79, 1985.

[62] C. Fichtner, C. Laurich, E. Bothe, and W. Lubitz. Spectroelectrochemical characterization of the NiFe hydrogenase of *Desulfovibrio vulgaris* Miyazaki F. *Biochemistry*, 45:9706–9716, 2006.

[63] S. Foerster, M. Stein, M. Brecht, H. Ogata, Y. Higuchi, and W. Lubitz. Single crystal EPR studies of the reduced active site of NiFe hydrogenase from *Desulfovibrio vulgaris* Miyazaki F. *J. Am. Chem. Soc.*, 125:83–93, 2003.

[64] S. Foerster, M. van Gastel, M. Brecht, and W. Lubitz. An orientation-selected ENDOR and HYSCORE study of the Ni-C active state of *Desulfovibrio vulgaris* Miyazaki F hydrogenase. *J. Biol. Inorg. Chem.*, 10:51–62, 2005.

[65] J. Friedebold and B. Bowien. Physiological and biochemical characterization of the soluble formate dehydrogenase, a molybdoenzyme from *Alcaligenes eutrophus*. *J. Bacteriol.*, 175:4719–4728, 1993.

[66] M. J. Frisch, G. W. Trucks, H. B. Schlegel, G. E. Scuseria, M. A. Robb, J. R. Cheeseman, G. Scalmani, V. Barone, B. Mennucci, G. A. Petersson, H. Nakatsuji, M. Caricato, X. Li, H. P. Hratchian, A. F. Izmaylov, J. Bloino, G. Zheng, J. L. Sonnenberg, M. Hada, M. Ehara, K. Toyota, R. Fukuda, J. Hasegawa, M. Ishida, T. Nakajima, Y. Honda, O. Kitao, H. Nakai, T. Vreven, J. A. J. Montgomery, J. E. Peralta, F. Ogliaro, M. Bearpark, J. J. Heyd, E. Brothers, K. N. Kudin, V. N. Staroverov, R. Kobayashi, J. Normand, K. Raghavachari, A. Rendell, J. C. Burant, S. S. Iyengar, J. Tomasi, M. Cossi, N. Rega, J. M. Millam, M. Klene,

J. E. Knox, J. B. Cross, V. Bakken, C. Adamo, J. Jaramillo, R. Gomperts, R. E. Stratmann, O. Yazyev, A. J. Austin, R. Cammi, C. Pomelli, J. W. Ochterski, R. L. Martin, K. Morokuma, V. G. Zakrzewski, G. A. Voth, P. Salvador, J. J. Dannenberg, S. Dapprich, A. D. Daniels, Ö. Farkas, J. B. Foresman, J. V. Ortiz, J. Cioslowski, and D. J. Fox. Gaussian 09 Revision E.01. 2009.

[67] J. Fritsch, P. Scheerer, S. Frielingsdorf, S. Kroschinsky, B. Friedrich, O. Lenz, and C. M. T. Spahn. The crystal structure of an oxygen-tolerant hydrogenase uncovers a novel iron-sulphur centre. *Nature*, 479:249–252, 2011.

[68] W. Fu, V. Morgan, L. E. Mortenson, and M. K. Johnson. Resonance Raman studies of the [4Fe-4S] to [2Fe-2S] cluster conversion in the iron protein of nitrogenase. *FEBS*, 284:165–168, 1991.

[69] W. Fu, P. M. Drozdzewski, M. D. Davies, S. G. Sligar, and M. K. Johnson. Resonance Raman and Magnetic Circular Dichroism Studies of Reduced [2Fe-2S] Proteins. *J. Biol. Chem.*, 267:15502–15510, 1992.

[70] C. D. Garner, P. E. Baugh, D. Collison, E. S. Davies, A. Dinsmore, J. A. Joule, and C. R. Wilson. Approaches to the total synthesis of Moco and Tuco. *J. Inorg. Biochem.*, 4:19072–19076, 2014.

[71] F. Germer, I. Zebger, M. Saggu, F. Lendzian, R. Schulz, and J. Appel. Overexpression, isolation, and spectroscopic characterization of the bidirectional NiFe hydrogenase from *Synechocystis* sp. PCC 6803. *J. Biol. Chem.*, 284:36462–36472, 2009.

[72] B. F. Gherman, M.-H. Baik, S. J. Lippard, and R. A. Friesner. Dioxygen activation in methane monooxygenase: a theoretical study. *J. Am. Chem. Soc.*, 126:2978–2990, 2004.

[73] S. M. Glueck, S. Gümüs, W. M. F. Fabian, and K. Faber. Biocatalytic carboxylation. *Chem. Soc. Rev.*, 39:313–328, 2010.

[74] C. A. Goddard and R. H. Holm. Synthesis and Reactivity Aspects of the Bis(dithiolene) Chalcogenide Series $[W^{IV}Q(S_2C_2R_2)_2]^{2-}$ (Q = O, S, Se). *Inorg. Chem.*, 38:5389–5398, 1999.

[75] T. Goris, A. F. Wait, M. Saggu, J. Fritsch, N. Heidary, M. Stein, I. Zebger, F. Lendzian, F. A. Armstrong, B. Friedrich, and O. Lenz. A unique iron-sulfur cluster is crucial for oxygen tolerance of a NiFe-hydrogenase. *Nat. Chem. Biol.*, 7: 310–318, 2011.

[76] E. Goto, T. Kodama, and Y. Minoda. Growth and Taxonomy of Thermophilic Hydrogen Bacteria. *Agric. Biol. Chem.*, 42:1305–1308, 2014.

[77] C. A. Grapperhaus and M. Y. Darensbourg. Oxygen Capture by Sulfur in Nickel Thiolates. *Acc. Chem. Res.*, 31:451–459, 1998.

[78] C. A. Grapperhaus, C. S. Mullins, P. M. Kozlowski, and M. S. Mashuta. Synthesis and oxygenation of a Nickel(II) and Zinc(II) dithiolate: An experimental and theoretical comparison. *Inorg. Chem.*, 43:2859–2866, 2004.

[79] B. L. Greene, C.-H. Wu, P. M. McTernan, M. W. W. Adams, and R. B. Dyer. Proton-coupled electron transfer dynamics in the catalytic mechanism of a NiFe-hydrogenase. *J. Am. Chem. Soc.*, 137:4558–4566, 2015.

[80] B. L. Greene, C.-H. Wu, G. E. Vansuch, M. W. W. Adams, and R. B. Dyer. Proton Inventory and Dynamics in the Ni_a-S to Ni_a-C Transition of a NiFe Hydrogenase. *Biochemistry*, 55:1813–1825, 2016.

[81] B. L. Greene, G. E. Vansuch, B. C. Chica, M. W. W. Adams, and R. B. Dyer. Applications of Photogating and Time Resolved Spectroscopy to Mechanistic Studies of Hydrogenases. *Acc. Chem. Res.*, 50:2718–2726, 2017.

[82] B. Guigliarelli, C. More, A. Fournel, M. Asso, E. C. Hatchikian, R. Williams, R. Cammack, and P. Bertrand. Structural organization of the Ni and (4Fe-4S) centers in the active form of *Desulfovibrio gigas* hydrogenase. Analysis of the magnetic interactions by electron paramagnetic resonance spectroscopy. *Biochemistry*, 34:4781–4790, 1995.

[83] Q. Guo, L. Gakhar, K. Wickersham, K. Francis, A. Vardi-Kilshtain, D. T. Major, C. M. Cheatum, and A. Kohen. Structural and Kinetic Studies of Formate Dehydrogenase from *Candida boidinii*. *Biochemistry*, 55:2760–2771, 2016.

[84] S. Han, R. S. Czernuszewicz, T. Kimura, M. W. W. Adam, and T. G. Spiro. Fe_2S_2 Protein Resonance Raman Spectra Revisited: Structural Variations among Adrenodoxin, Ferredoxin, and Red Paramagnetic Protein. *J. Am. Chem. Soc.*, 111:3505–3511, 1989.

[85] S. Han, R. S. Czernuszewicz, and T. G. Spiro. Vibrational Spectra and Normal Mode Analysis for [2Fe-2S] Protein Analogues Using ^{34}S, ^{54}Fe, and ^{2}H Substitution: Coupling of Fe-S Stretching and S-C-C Bending Modes. *J. Am. Chem. Soc.*, 111: 3496–3504, 1989.

[86] R. Happe, W. Roseboom, A. J. Pierik, S. P. Albracht, and K. A. Bagley. Biological activation of hydrogen. *Nature*, 385:126, 1997.

[87] R. Happe, W. Roseboom, G. Egert, C. G. Friedrich, C. Massanz, B. Friedrich, and S. P. J. Albracht. Unusual FTIR and EPR properties of the H_2-activating site of the cytoplasmic NAD-reducing hydrogenase from *Ralstonia eutropha*. *FEBS Lett*, 466:259–263, 2000.

[88] T. Hartmann and S. Leimkühler. The oxygen-tolerant and NAD^+-dependent formate dehydrogenase from *Rhodobacter capsulatus* is able to catalyze the reduction of CO_2 to formate. *FEBS J.*, 280:6083–6096, 2013.

[89] T. Hartmann, N. Schwanhold, and S. Leimkühler. Assembly and catalysis of molybdenum or tungsten-containing formate dehydrogenases from bacteria. *Biochim. Biophys. Acta*, 1854:1090–1100, 2015.

[90] T. Hartmann, P. Schrapers, T. Utesch, M. Nimtz, Y. Rippers, H. Dau, M. A. Mroginski, M. Haumann, and S. Leimkühler. The Molybdenum Active Site of Formate Dehydrogenase Is Capable of Catalyzing C-H Bond Cleavage and Oxygen Atom Transfer Reactions. *Biochemistry*, 55:2381–2389, 2016.

[91] P. J. Hay and W. R. Wadt. *Ab initio* effective core potentials for molecular calculations. Potentials for the transition metal atoms Sc to Hg. *J. Chem. Phys.*, 82: 270–283, 1985.

[92] N. R. Hayashi, T. Ishida, A. Yokota, T. Kodama, and Y. Igarashi. *Hydrogenophilus thermoluteolus* gen. nov., sp. nov., a thermophilic, facultatively chemolithoautotrophic, hydrogen-oxidizing bacterium. *Int. J. Syst. Evol. Bacteriol.*, 49 Pt 2: 783–786, 1999.

[93] R. Hidalgo, P. A. Ash, A. J. Healy, and K. A. Vincent. Infrared Spectroscopy During Electrocatalytic Turnover Reveals the Ni-L Active Site State During H_2 Oxidation by a NiFe Hydrogenase. *Angew. Chem.*, 54:7110–7113, 2015.

[94] M. Hikita, K. Shinzawa-Itoh, M. Moriyama, T. Ogura, K. Kihira, and S. Yoshikawa. Resonance Raman Spectral Properties of FMN of Bovine Heart NADH:ubiquinone Oxidoreductase Suggesting a Mechanism for the Prevention of Spontaneous Production of Reactive Oxygen Species. *Biochemistry*, 52:98–104, 2013.

[95] P. Hildebrandt and F. Siebert. Vibrational Spectroscopy in Life Science. 1st Edition by J. Wiley and Sons. 2008.

[96] R. Hille, J. Hall, and P. Basu. The mononuclear molybdenum enzymes. *Chem. Rev.*, 114:3963–4038, 2014.

[97] A. Hochheimer, R. A. Schmitz, R. K. Thauer, and R. Hedderich. The Tungsten Formylmethanofuran Dehydrogenase from *Methanobacterium Thermoautotrophicum* Contains Sequence Motifs Characteristic for Enzymes Containing Molybdopterin Dinucleotide. *Eur. J. Biochem.*, 234:910–920, 1995.

[98] A. Hochheimer, D. Linder, R. K. Thauer, and R. Hedderich. The molybdenum formylmethanofuran dehydrogenase operon and the tungsten formylmethanofuran dehydrogenase operon from *Methanobacterium thermoautotrophicum*. *Eur. J. Biochem.*, 242:156–162, 1996.

[99] A. Hochheimer, R. Hedderich, and R. K. Thauer. The formylmethanofuran dehydrogenase isoenzymes in *Methanobacterium wolfei* and *Methanobacterium thermoautotrophicum*: induction of the molybdenum isoenzyme by molybdate and constitutive synthesis of the tungsten isoenzyme. *Eur. J. Biochem.*, 170:389–393, 1998.

[100] M. Horch, L. Lauterbach, M. Saggu, P. Hildebrandt, F. Lendzian, R. Bittl, O. Lenz, and I. Zebger. Probing the active site of an O_2-tolerant NAD^+-reducing NiFe-hydrogenase from *Ralstonia eutropha* H16 by in situ EPR and FTIR spectroscopy. *Angew. Chem.*, 49:8026–8029, 2010.

[101] M. Horch, L. Lauterbach, O. Lenz, P. Hildebrandt, and I. Zebger. NAD(H)-coupled hydrogen cycling - structure-function relationships of bidirectional NiFe hydrogenases. *FEBS Lett.*, 586:545–556, 2012.

[102] M. Horch, Y. Rippers, M. A. Mroginski, P. Hildebrandt, and I. Zebger. Combining spectroscopy and theory to evaluate structural models of metalloenzymes: a case study on the soluble NiFe hydrogenase from *Ralstonia eutropha*. *ChemPhysChem*, 14:185–191, 2013.

[103] M. Horch, J. Schoknecht, M. A. Mroginski, O. Lenz, P. Hildebrandt, and I. Zebger. Resonance Raman spectroscopy on NiFe hydrogenase provides structural insights into catalytic intermediates and reactions. *J. Am. Chem. Soc.*, 136:9870–9873, 2014.

[104] M. Horch, P. Hildebrandt, and I. Zebger. Concepts in bio-molecular spectroscopy: vibrational case studies on metalloenzymes. *PCCP*, 17:18222–18237, 2015.

[105] M. Horch, L. Lauterbach, M. A. Mroginski, P. Hildebrandt, O. Lenz, and I. Zebger. Reversible active site sulfoxygenation can explain the oxygen tolerance of a NAD^+-reducing NiFe hydrogenase and its unusual infrared spectroscopic properties. *J. Am. Chem. Soc.*, 137:2555–2564, 2015.

[106] B. M. Hover, A. Loksztejn, A. A. Ribeiro, and K. Yokoyama. Identification of a cyclic nucleotide as a cryptic intermediate in molybdenum cofactor biosynthesis. *J. Am. Chem. Soc.*, 135:7019–7032, 2013.

[107] W. G. Jackson, A. F. M. M. Rahman, and D. C. Craig. The First Oxygen-Bonded Sulfenate Ion: Crystal and Molecular Structures of Bis(ethylenediamine)(2-pyridinesulfenato-O)cobalt(III) and Bis(ethylenediamine)(2-pyridinesulfinato- O)cobalt(III). *Inorg. Chem.*, 42:383–388, 2003.

[108] G. Jeschke. Kurze Einführung in die elektronenparamagnetische Resonanzspektroskopie. Universität Konstanz. 2008.

[109] H. K. Joshi, J. A. Cooney, F. E. Inscore, N. E. Gruhn, D. L. Lichtenberger, and J. H. Enemark. Investigation of metal-dithiolate fold angle effects: implications for molybdenum and tungsten enzymes. *PNAS*, 100:3719–3724, 2003.

[110] J. Kalms, A. Schmidt, S. Frielingsdorf, P. van der Linden, D. von Stetten, O. Lenz, P. Carpentier, and P. Scheerer. Krypton Derivatization of an O_2-Tolerant Membrane-Bound NiFe Hydrogenase Reveals a Hydrophobic Tunnel Network for Gas Transport. *Angew. Chem.* , 55:5586–5590, 2016.

[111] S. Kamali, H. Wang, D. Mitra, H. Ogata, W. Lubitz, B. C. Manor, T. B. Rauchfuss, D. Byrne, V. Bonnefoy, J. R. Jenney, E. Francis, M. W. W. Adams, Y. Yoda, E. Alp, J. Zhao, and S. P. Cramer. Observation of the Fe-CN and Fe-CO vibrations in the active site of NiFe hydrogenase by nuclear resonance Vib. Spectrosc. *Angew. Chem.*, 52:724–728, 2013.

[112] M. Kampa, M.-E. Pandelia, W. Lubitz, M. van Gastel, and F. Neese. A metal-metal bond in the light-induced state of NiFe hydrogenases with relevance to hydrogen evolution. *J. Am. Chem. Soc.*, 135:3915–3925, 2013.

[113] K. Karstens, S. Wahlefeld, M. Horch, M. Grunzel, L. Lauterbach, F. Lendzian, I. Zebger, and O. Lenz. Impact of the iron-sulfur cluster proximal to the active site on the catalytic function of an O_2-tolerant NAD^+-reducing NiFe-hydrogenase. *Biochemistry*, 54:389–403, 2015.

[114] S. Katz, J. Noth, M. Horch, H. S. Shafaat, T. Happe, P. Hildebrandt, and I. Zebger. Vibrational Spectroscopy reveals the initial steps of biological hydrogen evolution. *Chem. Sci.*, 7:6746–6752, 2016.

[115] R. M. Kelly and J. W. Deming. Extremely thermophilic archaebacteria: biological and engineering considerations. *Biotechnol. Prog.*, 4:47–62, 1988.

[116] S. V. Khangulov, V. N. Gladyshev, G. C. Dismukes, and T. C. Stadtman. Selenium-containing formate dehydrogenase H from *Escherichia coli*: a molybdopterin enzyme that catalyzes formate oxidation without oxygen transfer. *Biochemistry*, 37: 3518–3528, 1998.

[117] T. Kishima, T. Matsumoto, H. Nakai, S. Hayami, T. Ohta, and S. Ogo. A High-Valent Iron(IV) Peroxo Core Derived from O_2. *Angew. Chem.*, 128:734–737, 2016.

[118] L. Kleihues, O. Lenz, M. Bernhard, T. Buhrke, and B. Friedrich. The H_2 Sensor of *Ralstonia eutropha* Is a Member of the Subclass of Regulatory [NiFe] Hydrogenases. *J. Bacteriol.*, 182:2716–2724, 2000.

[119] T. Krämer, M. Kampa, W. Lubitz, M. van Gastel, and F. Neese. Theoretical spectroscopy of the Ni(II) intermediate states in the catalytic cycle and the activation of NiFe hydrogenases. *Chembiochem*, 14:1898–1905, 2013.

[120] H. A. Kramers and W. Heisenberg. Über die Streuung von Strahlung durch Atome. *Z. Phys.*, 31:681–708, 1925.

[121] H. Krassen, A. Schwarze, B. Friedrich, K. Ataka, O. Lenz, and J. Heberle. Photosynthetic Hydrogen Production by a Hybrid Complex of Photosystem I and [NiFe]-Hydrogenase. *ACS Nano*, 3:4055–4061, 2009.

[122] O. Kruse and B. Hankamer. Microalgal hydrogen production. *Curr. Opin. Biotechnol.*, 21:238–243, 2010.

[123] G. J. Kubas. Fundamentals of H_2 binding and reactivity on transition metals underlying hydrogenase function and H_2 production and storage. *Chem. Rev.*, 107: 4152–4205, 2007.

[124] J. Kuper, A. Llamas, H. J. Hecht, R. R. Mendel, and G. Schwarz. Structure of a molybdopterin-bound cnx1g domain links molybdenum and copper metabolism. *Nature*, 430:803–806, 2004.

[125] P. Kwan, C. L. McIntosh, D. P. Jennings, R. C. Hopkins, S. K. Chandrayan, C.-H. Wu, M. W. W. Adams, and A. K. Jones. The NiFe-Hydrogenase of *Pyrococcus furiosus* Exhibits a New Type of Oxygen Tolerance. *J. Am. Chem. Soc.*, 137:13556–13565, 2015.

[126] U. K. Laemmli. Cleavage of Structural Proteins during the Assembly of the Head of Bacteriophage T4. *Nature*, 227:680–685.

[127] M. W. Lake, C. A. Temple, K. V. Rajagopalan, and H. Schindelin. The crystal structure of the *Escherichia coli* MobA protein provides insight into molybdopterin guanine dinucleotide biosynthesis. *J. Biol. Chem.*, 275:40211–40217, 2000.

[128] G. Landsberg and L. Mandelstam. Eine neue Erscheinung bei der Lichtzerstreuung in Krystallen. *Sci. Nat.*, 16:772, 1928.

[129] L. Lauterbach and O. Lenz. Catalytic production of hydrogen peroxide and water by oxygen-tolerant NiFe-hydrogenase during H_2 cycling in the presence of O_2. *J. Am. Chem. Soc.*, 135:17897–17905, 2013.

[130] L. Lauterbach, Z. Idris, K. A. Vincent, and O. Lenz. Catalytic properties of the isolated diaphorase fragment of the NAD-reducing NiFe-hydrogenase from *Ralstonia eutropha*. *PloS one*, 6:e25939, 2011.

[131] L. Lauterbach, J. Liu, M. Horch, P. Hummel, A. Schwarze, M. Haumann, K. A. Vincent, O. Lenz, and I. Zebger. The Hydrogenase Subcomplex of the NAD^+-Reducing [NiFe] Hydrogenase from *Ralstonia eutropha* - Insights into Catalysis and Redox Interconversions. *Eur. J. Inorg. Chem.*, 2011:1067–1079, 2011.

[132] L. Lauterbach, H. Wang, M. Horch, L. B. Gee, Y. Yoda, Y. Tanaka, I. Zebger, O. Lenz, and S. P. Cramer. Nuclear resonance Vib. Spectrosc. reveals the FeS cluster composition and active site vibrational properties of an O_2-tolerant NAD^+-reducing NiFe hydrogenase. *Chem Sci.*, 6:1055–1060, 2015.

[133] V. I. Lebedev and D. N. Laikov. A quadrature formula for the sphere of the 131st algebraic order of accuracy. *Doklady Mathematics*, 59:477–481, 1999.

[134] Lee, C. and Yang, W. and Parr, R. G. Development of the Colle-Salvetti correlation-energy formula into a functional of the electron density. *Phys. Rev. B*, 37:785–789, 1988.

[135] M. Lenz, O.and Ludwig, T. Schubert, I. Bürstel, S. Ganskow, T. Goris, A. Schwarze, and B. Friedrich. H_2 Conversion in the Presence of O_2 as Performed by the Membrane-Bound [NiFe]-Hydrogenase of *Ralstonia eutropha*. *ChemPhysChem*, 11: 1107–1119, 2010.

[136] S. Leonhartsberger, I. Korsa, and A. Bock. The molecular biology of formate metabolism in enterobacteria. *J. Mol. Microbiol. Biotechnol.*, 225:269–276, 2002.

[137] M. Leopoldini, S. G. Chiodo, M. Toscano, and N. Russo. Reaction mechanism of molybdoenzyme formate dehydrogenase. *Chemistry*, 14:8674–8681, 2008.

[138] S. O. N. Lill and P. E. M. Siegbahn. An autocatalytic mechanism for NiFe-hydrogenase: reduction to Ni(I) followed by oxidative addition. *Biochemistry*, 48: 1056–1066, 2009.

[139] B. S. Lim, J. P. Donahue, and R. H. Holm. Synthesis and Structures of Bis(dithiolene)molybdenum Complexes Related to the Active Sites of the DMSO Reductase Enzyme Family. *Inorg. Chem.*, 39:263–273, 2000.

[140] N. J. Lindenmaier, S. Wahlefeld, E. Bill, T. Szilvási, C. Eberle, S. Yao, P. Hildebrandt, M. Horch, I. Zebger, and M. Driess. An S-Oxygenated NiFe Complex Modelling Sulfenate Intermediates of an O_2 -Tolerant Hydrogenase. *Angew. Chem.*, 56:2208–2211, 2017.

[141] T. Liu, B. Li, M. L. Singleton, M. B. Hall, and M. Y. Darensbourg. Sulfur oxygenates of biomimetics of the diiron subsite of the FeFe-hydrogenase active site: Properties and oxygen damage repair possibilities. *J. Am. Chem. Soc.*, 131:8296–8307, 2009.

[142] D. A. Long. The Raman Effect: A Unified Treatment of the Theory of Raman Scattering by Molecules. 1st Edition by J. Wiley and Sons. 2002.

[143] J. Löwenstein, L. Lauterbach, C. Teutloff, O. Lenz, and R. Bittl. Active site of the NAD^+-reducing hydrogenase from *Ralstonia eutropha* studied by EPR spectroscopy. *J. Phys. Chem. B*, 119:13834–13841, 2015.

[144] W. Lubitz, H. Ogata, O. Rüdiger, and E. Reijerse. Hydrogenases. *Chem. Rev.*, 114: 4081–4148, 2014.

[145] C. E. Lubner, P. Knörzer, P. J. N. Silva, K. A. Vincent, T. Happe, D. A. Bryant, and J. H. Golbeck. Wiring an [FeFe]-Hydrogenase with Photosystem I for Light-Induced Hydrogen Production. *Biochemistry*, 49:10264–10266, 2010.

[146] P. Lugo-Mas, A. Dey, L. Xu, S. D. Davin, J. Benedict, W. Kaminsky, K. O. Hodgson, B. Hedman, E. I. Solomon, and J. A. Kovacs. How does single oxygen atom addition affect the properties of an Fe-nitrile hydratase analogue? The compensatory role of the unmodified thiolate. *J. Am. Chem. Soc.*, 128:11211–11221, 2006.

[147] K. Ma, R. N. Schicho, R. M. Kelly, and M. W. W. Adams. Hydrogenase of the hyperthermophile *Pyrococcus furiosus* is an elemental sulfur reductase or sulfhydrogenase: evidence for a sulfur-reducing hydrogenase ancestor. *PNAS*, 90:5341–5344, 1993.

[148] K. Ma, R. Weiss, and M. W. W. Adams. Characterization of hydrogenase II from the hyperthermophilic archaeon *Pyrococcus furiosus* and assessment of its role in sulfur reduction. *J. Bacteriol.*, 182:1864–1871, 2000.

[149] V. Madhu and S. K. Das. New series of asymmetrically substituted Bis(1,2-dithiolato)-nickel(III) complexes exhibiting near IR absorption and structural diversity. *Inorg. Chem.*, 47:5055–5070, 2008.

[150] L. B. Maia, L. Fonseca, I. Moura, and J. J. G. Moura. Reduction of Carbon Dioxide by a Molybdenum-Containing Formate Dehydrogenase: A Kinetic and Mechanistic Study. *J. Am. Chem. Soc.*, 138:8834–8846, 2016.

[151] C. J. Marx and M. E. Lidstrom. Development of improved broad-host-range vectors for use in methylotrophs and other Gram-negative bacteria. *Microbiol.*, 147:2065–2075, 2001.

[152] C. Massanz, S. Schmidt, and B. Friedrich. Subforms and In Vitro Reconstitution of the NAD-Reducing Hydrogenase of *Alcaligenes eutrophus*. *J. Bacteriol.*, 180: 1023–1029, 1998.

[153] K. G. Matz, R. P. Mtei, B. Leung, S. J. N. Burgmayer, and M. L. Kirk. Noninnocent dithiolene ligands: a new oxomolybdenum complex possessing a donor-acceptor dithiolene ligand. *J. Am. Chem. Soc.*, 132:7830–7831, 2010.

[154] K. G. Matz, R. P. Mtei, R. Rothstein, M. L. Kirk, and S. J. N. Burgmayer. Study of molybdenum(4+) quinoxalyldithiolenes as models for the noninnocent pyranopterin in the molybdenum cofactor. *Inorg. Chem.*, 50:9804–9815, 2011.

[155] I. Mayer. Charge, bond order and valence in the AB initio SCF theory. *Chem. Phys. Lett.*, 97:270–274, 1983.

[156] I. Mayer. Bond order and valence: Relations to Mulliken's population analysis. *Int. J. Quantum Chem.*, 26:151–154, 1984.

[157] A. P. Mehta, S. H. Abdelwahed, and T. P. Begley. Molybdopterin biosynthesis: trapping an unusual purine ribose adduct in the MoaA-catalyzed reaction. *J. Am. Chem. Soc.*, 135:10883–10885, 2013.

[158] D. K. Mills, J. H. Reibenspies, and M. Y. Darensbourg. Sterically protected nickel(II) in a N_2S_2 donor environment: 1,5-bis(mercaptoethyl)-1,5-diazacyclooctane and its methylated derivative, 1990.

[159] D. Mitra, V. Pelmenschikov, Y. Guo, D. A. Case, H. Wang, W. Dong, M.-L. Tan, T. Ichiye, F. E. Jenney, M. W. W. Adams, Y. Yoda, J. Zhao, and S. P. Cramer. Dynamics of the 4Fe-4S cluster in *Pyrococcus furiosus* D14C ferredoxin via nuclear resonance vibrational and resonance Raman spectroscopies, force field simulations, and density functional theory calculations. *Biochemistry*, 50:5220–5235, 2011.

[160] Y. Montet, P. Amara, A. Volbeda, X. Vernede, E. C. Hatchikian, M. J. Field, M. Frey, and J. C. Fontecilla-Camps. Gas access to the active site of Ni-Fe hydrogenases probed by X-ray crystallography and molecular dynamics. *Nat. Struct. Biol.*, 4:523–526, 1997.

[161] D. Moss, E. Nabedryk, J. Breton, and W. Mäntele. Redox-linked conformational changes in proteins detected by a combination of infrared spectroscopy and protein electrochemistry. *Eur. J. Biochem.*, 187:565–572, 1990.

[162] C. S. Mota, M. G. Rivas, C. D. Brondino, I. Moura, J. J. G. Moura, P. J. Gonzalez, and N. M. F. S. A. Cerqueira. The mechanism of formate oxidation by metal-dependent formate dehydrogenases. *J. Biol. Inorg. Chem.*, 16:1255–1268, 2011.

[163] R. P. Mtei, E. Perera, B. Mogesa, B. Stein, P. Basu, and M. L. Kirk. A Valence Bond Description of Dizwitterionic Dithiolene Character in an Oxomolybdenum-bis(dithione). *Eur. J. Inorg. Chem.*, 2011:5467–5470, 2011.

[164] B. J. Murphy, R. Hidalgo, M. M. Roessler, R. M. Evans, P. A. Ash, W. K. Myers, K. A. Vincent, and F. A. Armstrong. Discovery of Dark pH-Dependent H(+) Migration in a NiFe-Hydrogenase and Its Mechanistic Relevance: Mobilizing the Hydrido Ligand of the Ni-C Intermediate. *J. Am. Chem. Soc.*, 137:8484–8489, 2015.

[165] E. Nakamaru-Ogiso, T. Yano, T. Yagi, and T. Ohnishi. Characterization of the iron-sulfur cluster N7 (N1c) in the subunit NuoG of the proton-translocating NADH-quinone oxidoreductase from *Escherichia coli*. *J. Biol. Chem.*, 280:301–307, 2005.

[166] V. N. Nemykin, J. G. Olsen, E. Perera, and P. Basu. Synthesis, molecular and electronic structure, and TDDFT and TDDFT-PCM study of the solvatochromic

properties of $(Me_2Pipdt)Mo(CO)_4$ complex (Me_2Pipdt = *N,N'* dimethylpiperazine-2,3-dithione). *Inorg. Chem.*, 45:3557–3568, 2006.

[167] M. Neumann, M. Schulte, N. Junemann, W. Stocklein, and S. Leimkühler. *Rhodobacter capsulatus* XdhC is involved in molybdenum cofactor binding and insertion into xanthine dehydrogenase. *J. Biol. Chem.*, 281:15701–15708, 2006.

[168] M. Neumann, G. Mittelstädt, F. Seduk, C. Iobbi-Nivol, and S. Leimkühler. MocA is a specific cytidylyltransferase involved in molybdopterin cytosine dinucleotide biosynthesis in *Escherichia coli*. *J. Biol. Chem.*, 284:21891–21898, 2009.

[169] J. Nichols and K. V. Rajagopalan. *Escherichia coli* MoeA and MogA. Function in metal incorporation step of molybdenum cofactor biosynthesis. *J. Biol. Chem.*, 277: 24995–25000, 2002.

[170] J. D. Nichols and K. V. Rajagopalan. *In vitro* molybdenum ligation to molybdopterin using purified components. *J. Biol. Chem.*, 280:7817–7822, 2005.

[171] Y. Nicolet, C. Piras, P. Legrand, E. C. Hatchikian, and J. C. Fontecilla-Camps. *Desulfovibrio desulfuricans* iron hydrogenase: the structure shows unusual coordination to an active site Fe binuclear center. *Structure*, 7:13–23, 1999.

[172] D. Niks, J. Duvvuru, M. Escalona, and R. Hille. Spectroscopic and Kinetic Properties of the Molybdenum-containing, NAD^+-dependent Formate Dehydrogenase from *Ralstonia eutropha*. *J. Biol. Chem.*, 291:1162–1174, 2016.

[173] C. J. O'Connor. Magnetochemistry Advances in Theory and Experimentation. *in Progress in Inorg. Chem., John Wiley and Sons, Inc, Hoboken, NJ, USA, 203*, 1982.

[174] H. Ogata, S. Hirota, A. Nakahara, H. Komori, N. Shibata, T. Kato, K. Kano, and Y. Higuchi. Activation process of NiFe hydrogenase elucidated by high-resolution X-ray analyses: conversion of the ready to the unready state. *Structure*, 13:1635–1642, 2005.

[175] H. Ogata, P. Kellers, and W. Lubitz. The crystal structure of the NiFe hydrogenase from the photosynthetic bacterium *Allochromatium vinosum*: characterization of the oxidized enzyme (Ni-A state). *J. Mol. Biol.*, 402:428–444, 2010.

[176] H. Ogata, T. Kramer, H. Wang, D. Schilter, V. Pelmenschikov, M. van Gastel, F. Neese, T. B. Rauchfuss, L. B. Gee, A. D. Scott, Y. Yoda, Y. Tanaka, W. Lubitz, and S. P. Cramer. Hydride bridge in NiFe-hydrogenase observed by nuclear resonance Vib. Spectrosc. *Nat. Commun.*, 6:7890, 2015.

[177] H. Ogata, K. Nishikawa, and W. Lubitz. Hydrogens detected by subatomic resolution protein crystallography in a NiFe hydrogenase. *Nature*, 520:571–574, 2015.

[178] S. Ogo, K. Ichikawa, T. Kishima, T. Matsumoto, H. Nakai, K. Kusaka, and T. Ohhara. A functional NiFehydrogenase mimic that catalyzes electron and hydride transfer from H_2. *Science*, 339:682–684, 2013.

[179] T. Ohnishi. Iron-sulfur clusters/semiquinones in complex I. *Biochim. Biophys. Acta*, 1364:186–206, 1998.

[180] T. Palmer, C.-L. Santini, C. Iobbi-Nivol, D. J. Eaves, D. H. Boxer, and G. Giordano. Involvement of the *narJ* and *mob* gene products in distinct steps in the biosynthesis of the molybdoenzyme nitrate reductase in *Escherichia coli*. *Mol. Micro.*, 20:875–884, 1996.

[181] M.-E. Pandelia, P. Infossi, M. Stein, M.-T. Giudici-Orticoni, and W. Lubitz. Spectroscopic characterization of the key catalytic intermediate Ni-C in the O_2-tolerant NiFe hydrogenase I from *Aquifex aeolicus*: evidence of a weakly bound hydride. *Chem. Commun.*, 48:823–825, 2012.

[182] S. D. Patel, R. Aebersold, and G. Attardi. cDNA-derived amino acid sequence of the NADH-binding 51-kDa subunit of the bovine respiratory NADH dehydrogenase reveals striking similarities to a bacterial NAD^+-reducing hydrogenase. *PNAS*, 88: 4225–4229, 1991.

[183] E. Perera and P. Basu. Synthesis, characterization and structure of a low coordinate desoxomolybdenum cluster stabilized by a dithione ligand. *Dalton trans.*, 25:5023–5028, 2009.

[184] J. W. Peters, W. N. Lanzilotta, B. J. Lemon, and L. C. Seefeldt. X-ray Crystal Structure of the Fe-Only Hydrogenase (CpI) from Clostridium pasterrianum to 1.8 Angstrom Resolution. *Science*, 282:1853–1858, 1998.

[185] G. A. Petersson and M. A. Al-Laham. A complete basis set model chemistry. II. Open-shell systems and the total energies of the first-row atoms. *J. Chem. Phys.*, 94:6081–6090, 1991.

[186] A. J. Pierik, W. Roseboom, R. P. Happe, K. A. Bagley, and S. P. J. Albracht. Carbon Monoxide and Cyanide as Intrinsic Ligands to Iron in the Active Site of [NiFe]-Hydrogenases. *J. Biol. Chem.*, 274:3331–3337, 1999.

[187] S. J. Pilkington, J. M. Skehel, R. B. Gennis, and J. E. Walker. Relationship between mitochondrial NADH-ubiquinone reductase and a bacterial NAD-reducing hydrogenase. *Biochemistry*, 30:2166–2175, 1991.

[188] I. V. Pimkov, A. Peterson, D. N. Vaccarello, and P. Basu. A Regioselective Synthesis of the Dephospho Dithiolene Protected Molybdopterin. *RSC Adv.*, 4:19072–19076, 2014.

[189] D. M. Pitterle and K. V. Rajagopalan. Two proteins encoded at the *chlA* locus constitute the converting factor of *Escherichia coli chlA1*. *J. Bacteriol.*, 171:3373–3378, 1989.

[190] D. M. Pitterle and K. V. Rajagopalan. Molybdopterin formation by converting factor of *E. coli chlA1*. *FASEB J*, 5:A468, 1991.

[191] D. M. Pitterle and K. V. Rajagopalan. The biosynthesis of molybdopterin in *Escherichia coli*. Purification and characterization of the converting factor. *J. Biol. Chem.*, 268:13499–13505, 1993.

[192] D. M. Pitterle, J. L. Johnson, and K. V. Rajagopalan. Purification and characterization of the converting factor from *E. coli chlA1*. *FASEB J*, 4:A1957, 1990.

[193] D. M. Pitterle, J. L. Johnson, and R. K. V. *In vitro* synthesis of molybdopterin from precursor Z using purified converting factor. Role of protein-bound sulfur in formation of the dithiolene. *J. Biol. Chem.*, 268:13506–13509, 1993.

[194] G. Placzek. Quantenmechanik der Strahlung. *Akademische Verlagsgesellschaft mbH: Leipzig*, 1934.

[195] V. O. Popov and V. S. Lamzin. NAD^+-dependet formate dehydrogenase. *Biochem. J.*, 301:625–643, 1994.

[196] A. Porthun, M. Bernhard, and B. Friedrich. Expression of a functional NAD-reducing NiFe hydrogenase from the gram-positive *Rhodococcus opacus* in the gram-negative *Ralstonia eutropha*. *Arch. Microbiol.*, 177:159–166, 2002.

[197] J. Preissler, S. Wahlefeld, C. Lorent, C. Teutloff, M. Horch, L. Lauterbach, S. P. Cramer, I. Zebger, and O. Lenz. Enzymatic and spectroscopic properties of a thermostable [NiFe]-hydrogenase performing H_2-driven NAD^+-reduction in the presence of O_2. *Biochim. Biophys. Acta*, 1859:8–18, 2018.

[198] J. Qiao, Y. Liu, F. Hong, and J. Zhang. A review of catalysts for the electroreduction of carbon dioxide to produce low-carbon fuels. *Chem. Soc. Rev.*, 43:631–675, 2014.

[199] H. Raaijmakers, S. Macieira, J. M. Dias, S. Teixeira, S. Bursakov, R. Huber, J. J. G. Moura, I. Moura, and M. J. Romão. Gene Sequence and the 1.8 Å Crystal Structure of the Tungsten-Containing Formate Dehydrogenase from *Desulfovibrio gigas*. *Structure*, 10:1261–1272, 2002.

[200] H. C. A. Raaijmakers and M. J. Romão. Formate-reduced *E. coli* formate dehydrogenase H: The reinterpretation of the crystal structure suggests a new reaction mechanism. *J. Biol. Inorg. Chem.*, 11:849–854, 2006.

[201] C. V. Raman and K. S. A. Krishan. A New Type of Secondary Radiation. *Nature*, 121:501–502, 1928.

[202] J. Ratzka, L. Lauterbach, O. Lenz, and M. B. Ansorge-Schumacher. Systematic evaluation of the dihydrogen-oxidising and NAD^+-reducing soluble [NiFe]-hydrogenase from *Ralstonia eutropha* H16 as a cofactor regeneration catalyst. *Biocatal. Biotransformation*, 29:246–252, 2011.

[203] T. Reda, C. D. Barker, and J. Hirst. Reduction of the iron-sulfur clusters in mitochondrial NADH:ubiquinone oxidoreductase (complex I) by EuII-DTPA, a very low potential reductant. *Biochemistry*, 47:8885–8893, 2008.

[204] A. E. Reed, B. Weinstock, and F. Weinhold. Natural population analysis. *J. Chem. Phys.*, 83:735–746, 1985.

[205] A. E. Reed, L. A. Curtiss, and F. Weinhold. Intermolecular interactions from a natural bond orbital, donor-acceptor viewpoint. *Chem. Rev.*, 88:899–926, 1988.

[206] H. A. Reeve, L. Lauterbach, P. A. Ash, O. Lenz, and K. A. Vincent. A modular system for regeneration of NAD cofactors using graphite particles modified with hydrogenase and diaphorase moieties. *Chem. Commun.*, 48:1589–1591, 2012.

[207] H. A. Reeve, L. Lauterbach, O. Lenz, and K. A. Vincent. Enzyme-Modified Particles for Selective Biocatalytic Hydrogenation by Hydrogen-Driven NADH Recycling. *ChemCatChem*, 7:3480–3487, 2015.

[208] S. Reschke, K. G. V. Sigfridsson, P. Kaufmann, N. Leidel, S. Horn, K. Gast, C. Schulzke, M. Haumann, and S. Leimkü hler. Identification of a bis-molybdopterin intermediate in molybdenum cofactor biosynthesis in *Escherichia coli*. *J. Biol. Chem.*, 288:29736–29745, 2013.

[209] Y. Rippers, T. Utesch, P. Hildebrandt, I. Zebger, and M. A. Mroginski. Insights into the structure of the active site of the O_2-tolerant membrane bound NiFe hydrogenase of *R. eutropha* H16 by molecular modelling. *PCCP*, 13:16146–16149, 2011.

[210] Y. Rippers, M. Horch, P. Hildebrandt, I. Zebger, and M. A. Mroginski. Revealing the absolute configuration of the CO and CN^- ligands at the active site of a NiFe hydrogenase. *ChemPhysChem*, 13:3852–3856, 2012.

[211] W. E. Robinson, A. Bassegoda, E. Reisner, and J. Hirst. Oxidation-State-Dependent Binding Properties of the Active Site in a Mo-Containing Formate Dehydrogenase. *J. Am. Chem. Soc.*, 139:9927–9936, 2017.

[212] R. A. Rothery, B. Stein, M. Solomonson, M. L. Kirk, and J. H. Weiner. Pyranopterin conformation defines the function of molybdenum and tungsten enzymes. *PNAS*, 109:14773–14778, 2012.

[213] M. J. Rudolph, M. M. Wuebbens, K. V. Rajagopalan, and H. Schindelin. Crystal structure of molybdopterin synthase and its evolutionary relationship to ubiquitin activation. *Nat. Struct. Biol.* , 8:42–46, 2001.

[214] J. A. Santamaria-Araujo, B. Fischer, T. Otte, M. Nimtz, R. R. Mendel, V. Wray, and G. Schwarz. The tetrahydropyranopterin structure of the sulfur-free and metal-free molybdenum cofactor precursor. *J. Biol. Chem.*, 279:15994–15999, 2004.

[215] R. G. Sawers, S. P. Ballantine, and D. H. Boxer. Differential Expression of Hydrogenase Isoenzymes in *Escherichia coli* K-12: Evidence for a Third Isoenzyme. *J. Bacteriol.*, 164:1324–1331, 1985.

[216] R. G. Sawers, D. J. Jamieson, C. F. Higgins, and D. H. Boxer. Characterization and Physiological Roles of Membrane-Bound Hydrogenase Isoenzymes from *Salmonella typhimurium*. *J. Bacteriol.*, 368:398–404, 1986.

[217] D. Schilter, J. M. Camara, M. T. Huynh, S. Hammes-Schiffer, and T. B. Rauchfuss. Hydrogenase Enzymes and Their Synthetic Models: The Role of Metal Hydrides. *Chem. Rev.*, 116:8693–8749, 2016.

[218] O. Schmitz, G. Boison, R. Hilscher, B. Hundeshagen, W. Zimmer, F. Lottspeich, and H. Bothe. Molecular Biological Analysis of a Bidirectional Hydrogenase from Cyanobacteria. *Eur. J. Biochem.*, 233:266–276, 1995.

[219] O. Schmitz, G. Boison, H. Salzmann, H. Bothe, K. Schütz, S.-h. Wang, and T. Happe. HoxE-a subunit specific for the pentameric bidirectional hydrogenase complex (HoxEFUYH) of cyanobacteria. *Biochim. Biophys. Acta*, 1554:66–74, 2002.

[220] K. Schneider and H. G. Schlegel. Purification and properties of soluble hydrogenase from *Alcaligenes eutrophus* H 16. *Biochim. Biophys. Acta*, 452:66–80, 1976.

[221] K. Schneider and H. G. Schlegel. Production of superoxide radicals by soluble hydrogenase from *Alcaligenes eutrophus* H16. *Biochem. J.*, 193:99–107, 1981.

[222] K. Schneider, R. Cammack, H. G. Schlegel, and D. O. Hall. The iron-sulphur centres of soluble hydrogenase from *Alcaligenes eutrophus*. *Biochim. Biophys. Acta*, 578: 445–461, 1979.

[223] K. Schneider, R. Cammack, and H. G. Schlegel. Content and localization of FMN, Fe-S clusters and nickel in the NAD-linked hydrogenase of *Nocardia opaca* 1b. *Eur. J. Biochem.*, 142:75–84, 1984.

[224] K. Schneider, H. G. Schlegel, and J. Karla. Effect of nickel on activity and subunit composition of purified hydrogenase from *Nocardia opaca* 1b. 138:533–541, 1984.

[225] P. Schrapers, T. Hartmann, R. Kositzki, H. Dau, S. Reschke, C. Schulzke, S. Leimkühler, and M. Haumann. Sulfido and cysteine ligation changes at the molybdenum cofactor during substrate conversion by formate dehydrogenase (FDH) from *Rhodobacter capsulatus*. *Inorg. Chem.*, 54:3260–3271, 2015.

[226] G. N. Schrauzer and V. P. Mayweg. Preparation, Reactions, and Structure of Bisdithio-α-diketone Complexes of Nickel, Palladium, and Platinum. *J. Am. Chem. Soc.*, 87:1483–1489, 1965.

[227] G. N. Schrauzer, V. P. Mayweg, and W. Heinrich. Coordination Compounds with Delocalized Ground States. α-Dithiodiketone-Substituted Group VI Metal Carbonyls and Related Compounds. *J. Am. Chem. Soc.*, 88:5174–5179, 1966.

[228] Schrauzer, G. N. and Mayweg, V. P. Coordination Compounds with Delocalized Ground States. Bisdithioglyoxalnickel and Related Complexes[1a,b]. *J. Am. Chem. Soc.*, 87:3585–3592, 1965.

[229] E. Schwartz, U. Gerischer, and B. Friedrich. Transcriptional Regulation of *Alcaligenes eutrophus* Hydrogenase Genes. *J. Bacteriol.*, 180, 1998.

[230] A. Schwarze, M. J. Kopczak, M. Rögner, and O. Lenz. Requirements for Construction of a Functional Hybrid Complex of Photosystem I and [NiFe]-Hydrogenase. *Appl. Environ. Microbiol.*, 76:2641–2651, 2010.

[231] L. T. Serebryakova, M. Medina, N. A. Zorin, I. N. Gogotov, and R. Cammack. Reversible hydrogenase of *Anabaena variabilis* ATCC 29413: catalytic properties and characterization of redox centres. *FEBS Lett.*, 383:79–82, 1996.

[232] G. M. Sheldrick. *SHEL-X*, Universität Göttingen. 1997.

[233] S. Shima, O. Pilak, M. Schick, M. S. Stagni, W. Meyer-Klaucke, E. Warkentin, R. K. Thauer, and U. Ermler. The Crystal Structure of [Fe]-Hydrogenase Reveals the Geometry of the Active Site. *Science*, 321:572–575, 2008.

[234] Y. Shomura, M. Taketa, H. Nakashima, H. Tai, H. Nakagawa, Y. Ikeda, M. Ishii, Y. Igarashi, H. Nishihara, K.-S. Yoon, S. Ogo, S. Hirota, and Y. Higuchi. Structural basis of the redox switches in the NAD^+-reducing soluble NiFe-hydrogenase. *Science*, 357:928–932, 2017.

[235] E. Siebert, M. Horch, Y. Rippers, J. Fritsch, S. Frielingsdorf, O. Lenz, F. Velazquez Escobar, F. Siebert, L. Paasche, U. Kuhlmann, F. Lendzian, M. A. Mroginski, I. Zebger, and P. Hildebrandt. Resonance Raman spectroscopy as a tool to monitor the active site of hydrogenases. *Angew. Chem.*, 52:5162–5165, 2013.

[236] E. Siebert, Y. Rippers, S. Frielingsdorf, J. Fritsch, A. Schmidt, J. Kalms, S. Katz, O. Lenz, P. Scheerer, L. Paasche, V. Pelmenschikov, U. Kuhlmann, M. A. Mroginski, I. Zebger, and P. Hildebrandt. Resonance Raman Spectroscopic Analysis of the NiFe Active Site and the Proximal 4Fe-3S Cluster of an O_2-Tolerant Membrane-Bound Hydrogenase in the Crystalline State. *J. Phys. Chem B*, 119:13785–13796, 2015.

[237] P. E. M. Siegbahn, J. W. Tye, and M. B. Hall. Computational studies of NiFe and FeFe hydrogenases. *Chem. Rev.*, 107:4414–4435, 2007.

[238] T. R. Simmons, G. Berggren, M. Bacchi, M. Fontecave, and V. Artero. Mimicking hydrogenases: From biomimetics to artificial enzymes. *Coord. Chem. Rev.*, 270-271: 127–150, 2014.

[239] A. Smekal. Zur Quantentheorie der Dispersion. *Sci. Nat.*, 11:873–875, 1923.

[240] C. Sparacino-Watkins, J. F. Stolz, and P. Basu. Nitrate and Periplasmic Nitrate Reductases. *Chem. Soc. Rev.*, 43:676–706, 2014.

[241] V. Stewart and C. H. MacGregor. Nitrate reductase in *Escherichia coli* K-12: Involvement of *chiC*, *chlE*, and *chlG* loci. *J. Bacteriol.*, 151:788–799, 1982.

[242] S. Stoll and A. Schweiger. EasySpin, a comprehensive software package for spectral simulation and analysis in EPR. *J. Magn. Reson.*, 178:42–55, 2006.

[243] S. T. Stripp, B. Soboh, U. Lindenstrauss, M. Braussemann, M. Herzberg, D. H. Nies, R. G. Sawers, and J. Heberle. HypD is the scaffold protein for Fe-$(CN)_2$CO cofactor assembly in [NiFe]-hydrogenase maturation. *Biochemistry*, 52:3289–3296, 2013.

[244] W. Sturhahn. CONUSS and PHOENIX: Evaluation of nuclear resonant scattering data. *Hyperfine Interact.*, 125:149–172, 2000.

[245] I. Sumner and G. A. Voth. Proton transport pathways in NiFe-hydrogenase. *J. Phys. Chem. B*, 116:2917–2926, 2012.

[246] H. Tai, K. Nishikawa, S. Inoue, Y. Higuchi, and S. Hirota. FT-IR Characterization of the Light-Induced Ni-L2 and Ni-L3 States of NiFe Hydrogenase from *Desulfovibrio vulgaris* Miyazaki F. *J. Phys. Chem. B*, 119:13668–13674, 2015.

[247] H. Tai, L. Xu, K. Nishikawa, Y. Higuchi, and S. Hirota. Equilibrium between inactive ready Ni-SI_r and active Ni-SI_a states of NiFe hydrogenase studied by utilizing Ni-SI_r-to-Ni-SI_a photoactivation. *Chem. Commun.*, 53:10444–10447, 2017.

[248] M. Taketa, H. Nakagawa, M. Habukawa, H. Osuka, K. Kihira, H. Komori, N. Shibata, M. Ishii, Y. Igarashi, H. Nishihara, K.-S. Yoon, S. Ogo, Y. Shomura, and Y. Higuchi. Crystallization and preliminary X-ray analysis of the NAD^+-reducing

NiFe hydrogenase from *Hydrogenophilus thermoluteolus* TH-1. *Acta Cryst. F*, 71: 96–99, 2015.

[249] M. Tiberti, E. Papaleo, N. Russo, L. de Gioia, and G. Zampella. Evidence for the formation of a Mo-H intermediate in the catalytic cycle of formate dehydrogenase. *Inorg. Chem.*, 51:8331–8339, 2012.

[250] J. Tomasi, B. Mennucci, and R. Cammi. Quantum mechanical continuum solvation models. *Chem. Rev.*, 105:2999–3093, 2005.

[251] A. Tran-Betcke, U. Warnecke, C. Böcker, C. Zaborosch, and B. Friedrich. Cloning and nucleotide sequences of the genes for the subunits of NAD-reducing hydrogenase of *Alcaligenes eutrophus* H16. *J. Bacteriol.*, 172:2920–2929, 1990.

[252] J. A. Turner. Sustainable Hydrogen Production. *Science*, 13:972–974, 2004.

[253] J. A. van Bokhoven and C. Lamberti. X-Ray Absorption and X-Ray Emission Spectroscopy: Theory and Applications, J. Wiley and Sons. 2016.

[254] E. van der Linden, T. Burgdorf, A. L. de Lacey, T. Buhrke, M. Scholte, V. M. Fernández, B. Friedrich, and S. P. Albracht. An improved purification procedure for the soluble [NiFe]-hydrogenase of *Ralstonia eutropha*: new insights into its (in)stability and spectroscopic properties. *J. Biol. Inorg. Chem.*, 11:247–260, 2006.

[255] J. W. van der Zwaan, S. P. J. Albracht, R. D. Fontijn, and E. C. Slater. Monovalent nickel in hydrogenase from *Chromatium vinosum*. *FEBS Lett.*, 179:271–277, 1985.

[256] M. van Gastel, M. Stein, M. Brecht, O. Schröder, F. Lendzian, R. Bittl, H. Ogata, Y. Higuchi, and W. Lubitz. A single-crystal ENDOR and density functional theory study of the oxidized states of the NiFe hydrogenase from *Desulfovibrio vulgaris* Miyazaki F. *J. Biol. Inorg. Chem.*, 11:41–51, 2006.

[257] M. J. van Stipdonk, P. Basu, S. A. Dille, J. K. Gibson, G. Berden, and J. Oomens. Infrared multiple photon dissociation spectroscopy of a gas-phase oxo-molybdenum complex with 1,2-dithiolene ligands. *J. Phys. Chem. A*, 118:5407–5418, 2014.

[258] P. M. Vignais and B. Billoud. Occurrence, classification, and biological function of hydrogenases: an overview. *Chem. Rev.*, 107:4206–4272, 2007.

[259] P. M. Vignais, B. Billoud, and J. Meyer. Classification and phylogeny of hydrogenases. *FEMS Microbiol. Rev.*, 25:455–501, 2001.

[260] A. Volbeda, M.-H. Charon, C. Piras, E. C. Hatchikian, M. Frey, and J. C. Fontecilla-Camps. Crystal structure of the nickel-iron hydrogenase from *Desulfovibrio gigas*. *Nature*, 373:580–587, 1995.

[261] A. Volbeda, E. Garcin, C. Piras, A. L. De Lacey, V. M. Fernández, E. C. Hatchikian, M. Frey, and J. C. Fontecilla-Camps. Structure of the [NiFe] hydrogenase active site: evidence for biologically uncommon Fe ligands. *J. Am. Chem. Soc.*, 118:12989–12996, 1996.

[262] A. Volbeda, L. Martin, C. Cavazza, M. Matho, B. W. Faber, W. Roseboom, S. P. J. Albracht, E. Garcin, M. Rousset, and J. C. Fontecilla-Camps. Structural differences between the ready and unready oxidized states of NiFe hydrogenases. *J. Biol. Inorg. Chem.*, 10:239–249, 2005.

[263] A. Volbeda, L. Martin, E. Barbier, O. Gutiérrez-Sanz, A. L. de Lacey, P.-P. Liebgott, S. Dementin, M. Rousset, and J. C. Fontecilla-Camps. Crystallographic studies of NiFe-hydrogenase mutants: towards consensus structures for the elusive unready oxidized states. *J. Biol. Inorg. Chem.*, 20:11–22, 2015.

[264] Vosko, S. H. and Wilk, L. and Nusair, M. Accurate spin-dependent electron liquid correlation energies for local spin density calculations: a critical analysis. *Can. J. Phys.*, 58:1200–1211, 1980.

[265] T. Wagner, U. Ermler, and S. Shima. The methanogenic CO_2 reducing-and-fixing enzyme is bifunctional and contains 46 4Fe-4S clusters. *Science* , 354:114–117, 2016.

[266] P.-h. Wang, R. B. Best, and J. Blumberger. Multiscale simulation reveals multiple pathways for H_2 and O_2 transport in a NiFe-hydrogenase. *J. Am. Chem. Soc.*, 133: 3548–3556, 2011.

[267] R. Wang, F. P. Healey, and J. Myers. Amperometric Measurement of Hydrogen Evolution in *Chlamydomonas*. *Plant Physiol.*, 48:108–110, 1971.

[268] C. J. R. C. Weast and M. J. Astle. Handbook of Chemistry and Physics. 49th Edition CRC Press Inc. 1979.

[269] W. Weigand and R. Wünsch. Sulfenato, Thiosulfinato, and Thiosulfonato Transition Metal Complexes. *Chem. Ber.*, 129:1409–1419, 1996.

[270] F. Weigend and R. Ahlrichs. Balanced basis sets of split valence, triple zeta valence and quadruple zeta valence quality for H to Rn: Design and assessment of accuracy. *PCCP*, 7:3297–3305, 2005.

[271] F. Weinhold, C. R. Landis, and E. D. Glendening. What is NBO analysis and how is it useful? *Int. Rev. Phys. Chem.*, 35:399–440, 2016.

[272] T. A. Werther, S. Wahlefeld, J. Salewski, U. Kuhlmann, I. Zebger, P. Hildebrandt, and H. W. Dobbek. Redox-dependent substrate-cofactor interactions in the Michaelis-complex of a flavin-dependent oxidoreductase. *Nat. Commun.*, 8: 16084, 2017.

[273] B. L. Westcott, N. E. Gruhn, and J. H. Enemark. Evaluation of Molybdenum–Sulfur Interactions in Molybdoenzyme Model Complexes by Gas-Phase Photoelectron Spectroscopy. The "Electronic Buffer" Effect. *J. Am. Chem. Soc.*, 120:3382–3386, 1998.

[274] B. R. Williams, Y. Fu, G. P. A. Yap, and S. J. N. Burgmayer. Structure and reversible pyran formation in molybdenum pyranopterin dithiolene models of the molybdenum cofactor. *J. Am. Chem. Soc.*, 134:19584–19587, 2012.

[275] J. Windhager, R. A. Seidel, U.-P. Apfel, H. Görls, G. Linti, and W. Weigand. Oxidation of diiron and triiron sulfurdithiolato complexes: mimics for the active site of FeFe-hydrogenase. *Chem. Biodiv.*, 5:2023–2041, 2008.

[276] I. Wolf, T. Buhrke, J. Dernedde, A. Pohlmann, and B. Friedrich. Duplication of *hyp* genes involved in maturation of [NiFe] hydrogenases in *Alcaligenes eutrophus* H16. *Arch. Microbiol.*, 170:451–459, 1998.

[277] M. M. Wuebbens and K. V. Rajagopalan. Structural characterization of a molybdopterin precursor. *J. Biol. Chem.*, 268:13493–13498, 1993.

[278] M. M. Wuebbens and K. V. Rajagopalan. Mechanistic and mutational studies of *Escherichia coli* molybdopterin synthase clarify the final step of molybdopterin biosynthesis. *J. Biol. Chem.*, 278:14523–14532, 2003.

[279] Y. Xiao, M.-L. Tan, T. Ichiye, H. Wang, Y. Guo, M. Smith, J. Meyer, W. Sturhahn, E. Alp, J. Zhao, Y. Yoda, and S. P. Cramer. Dynamics of *Rhodobacter capsulatus* 2Fe-2S ferredoxin VI and *Aquifex aeolicus* ferredoxin 5 via nuclear resonance vibrational spectroscopy (NRVS) and resonance Raman spectroscopy. *Biochemistry*, 47: 6612–6627, 2008.

[280] J. I. Yeh, A. Claiborne, and W. G. J. Hol. Structure of the Native Cysteine-Sulfenic Acid Redox Center of Enterococcal NADH Peroxidase Refined at 2.8 Å Resolution. *Biochemistry*, 35:9951–9957, 1996.

[281] C. Zaborosch, M. Köstert, E. Bill, K. Schneider, H. Schlegel, and A. Trautweint. EPR and Mössbauer spectroscopic studies on the tetrameric, NAD-linked hydrogenase of *Nocardia opaca* 1b and its two dimers: 1. The $\beta\delta$-dimer - a prototype of a simple hydrogenase. *Biometals*, 8, 1995.

[282] P. R. Zheng, Y.and Carey and B. A. Palfey. Raman spectrum of fully reduced flavin. *J. Raman Spectrosc.*, 35:521–524, 2004.

List of Abbreviations

ATP Adenosine triphosphate

ATR Attenuated total reflection

CCD charge-coupled device

cPMP Cyclic pyranopterin monophosphate

Cys Cysteine

DFT Density functional theory

DMSO Dimethyl sulfoxide

DTT Dithiothreitol

dmdt 4,5-dimethyl-1,3-dithiol-2-one

EPR Electron paramagnetic resonance

E. coli *Escherichia coli*

FMN Flavin mononucleotide

FGN Fructose glycerol ammonium

FTIR Fourier transform infrared (spectroscopy)

FDH Formiat Dehydrogenase

GTP Guanosine triphosphate

HOMO Highest occupied molecular orbital

Ht *Hydrogenophilus thermoluteolus* TH-1^T

IR Infrared

LUMO Lowest unoccupied molecular orbital

MGD bis-molybdopterin guanine dinucleotide

MS Mass spectrometry

MBO Mayer bond order

MCT Mercury cadmium telluride

MV Methyl viologen

MPT Molybdopterin

NPA Natural population analysis

NiFe Nickel-Iron active site

NAD(P)$^+$ Nicotinamide adenine dinucleotide (phosphate), oxidized

NAD(P)H Nicotinamide adenine dinucleotide (phosphate), reduced

Ni(bmmp-daco) *N,N'*-bis(dimethyl)mercaptopropyldiazacyclooctan nickel(II)

Ni(bmmp-dacoSO) *N*-dimethylmercaptopropyl-*N'*-dimethylsulfenato-propyldiazacyclooctan nickel(II)

NMR Nuclear magnetic resonance

NRVS Nuclear resonance vibrational spectroscopy

OTTLE Optically Transparent Thin Layer Electrochemical (cell)

pdb protein data base

QM/MM Quantum mechanics / Molecular mechanics

Re *Ralstonia eutropha*

RR Resonance Raman

Rc *Rhodobacter capsulatus*

SUMO Singly occupied molecular orbital

SH Soluble hydrogenase

SHE Standard hydrogen electrode

SQUID Superconducting quantum interference device

TCEP Tris(2-carboxyethyl)phosphine

SeCys Selenocysteine

UV/vis Ultraviolet-visible spectroscopy

WT Wild type

XAS X-ray absorption spectroscopy

Acknowledgement

Ich möchte mich bei folgenden Personen bedanken, ohne deren Unterstüzung diese Arbeit über die letzten Jahre nicht so entstanden wäre:

- An erster Stelle gilt mein herzlicher Dank meinem Doktorvater Prof. Dr. Peter Hildebrand, der mir die Möglichkeit gab, ein höchst interessantes Forschungsgebiet selbstständig bearbeiten zu können.
- Als Zweites bedanke ich mich bei Frau Prof. Dr. Ulla Wollenberger für die Übernahme des Zweitgutachtens.
- Bei Prof. Dr. Roderich Süssmuth bedanke ich mich für die Übernahme des Prüfungsvorsitzes.
- Mein herzlicher Dank gilt meinen beiden Betreuern Dr. Marius Horch und Dr. Ingo Zebger, die ihren "Junior" in allen Lebenslagen immer tatkräftig unterstützten.
- Bei Dr. Janina Preissler, Dr. Lars Lauterbach und Dr. Oliver Lenz bedanke ich mich für die erfolgreiche Zusammenarbeit zu der thermophilen löslichen Hydrogenase.
- Ich danke Christian Lorent für die EPR Messungen der *Ht*SH Proben sowie Christian Teutloff für dessen Unterstützung bei den EPR Auswertungen.
- Ich danke Dr. Nils Lindenmaier für die tolle Zusammenarbeit und seine Freundschaft, die sich trotz unzähliche Nachfragen zur Koordinationschemie gehalten hat. Desweiteren danke ich Prof. Dr. Matthias Drieß, Christopher Eberle und Dr. Shenglai Yao für ihre Hilfe mit den [NiFe] Komplexen. Die DFT Rechnungen wären ohne die Mitarbeit von Dr. Tibor Szilvási nicht zustande gekommen. Die Mößbauer und SQUID Experimente wurden von Dr. Eckhard Bill durchgeführt. Bei beiden bedanke ich mir für die angenehme Kooperation.
- Mein Dank gilt Dr. Tobias Hartmann, PhD. Benjamin Duffus und Prof. Dr. Slike Leimkühler für die nette Kooperation und die Bereitstellung der FDH Proben. Desweiteren bedanke ich mich bei Benjamin Duffus für die weiterführenden EPR Messungen.
- Bei Prof. Dr. Maria Andrea Mroginski und Dennis Belger möchte ich mich für die umfassende Kooperation, die Ausführung der DFT Rechnungen für die FDH, für die nette und herzliche Zusammenarbeit sowie die wertvollen, wissenschaftlichen Besprechungen bedanken.

- Ich danke allen jetzigen und ehemaligen Mitarbeiter*innen des Max-Volmer-Instituts, die zu der entspannten und produktiven Arbeitsatmospähre beigetragen haben.
- Ohne die Unterstützung meiner Eltern über die letzten Jahren wäre ich nicht in der Lage gewesen diese Arbeit zu Ende zu bringen.
- Als letztes gilt mein aufrichtigster Dank meiner Partnerin Violetta Rudolf und unseren Kindern Johann und Mathilda, die mir immer wieder vor Augen führen, das Leben mit allen seinen Facetten zu genießen.

List of publications

Parts of this work are published in peer-reviewed journals in the following articles

- J. Preissler*, S. Wahlefeld*, C. Lorent, C. Teutloff, M. Horch, L. Lauterbach, S. P. Cramer, I. Zebger, and O. Lenz. Enzymatic and spectroscopic properties of a thermostable [NiFe]-hydrogenase performing H_2-driven NAD^+-reduction in the presence of O_2. *Biochim. Biophys. Acta*, **1859**: 8-18, 2018.

- N. J. Lindenmaier*, S. Wahlefeld*, E. Bill, T. Szilvási, C. Eberle, S. Yao, P. Hildebrandt, M. Horch, I. Zebger, and M. Driess. An S-Oxygenated NiFe Complex Modelling Sulfenate Intermediates of an O_2-Tolerant Hydrogenase. *Angew. Chem.*, **56**: 2208-2211, 2017.

- N. J. Lindenmaier*, S. Wahlefeld*, E. Bill, T. Szilvási, C. Eberle, S. Yao, P. Hildebrandt, M. Horch, I. Zebger, and M. Driess. Ein S-oxygenierter [NiFe]-Komplex als Modell für Sulfenatintermediate einer O_2-toleranten Hydrogenase. *Angew. Chem.*, **56**: 2208-2211, 2017.

*Authors contributed equally to the work.

Other publications in peer-reviewed journals

- T. A. Werther, S. Wahlefeld, J. Salewski, U. Kuhlmann, I. Zebger, P. Hildebrandt, and H. W. Dobbek. Redox-dependent substrate-cofactor interactions in the Michaelis-complex of a flavin-dependent oxidoreductase. *Nat. Commun.*, **8**: 16084, 2017.

- K. Karstens, S. Wahlefeld, M. Horch, M. Grunzel, L. Lauterbach, F. Lendzian, I. Zebger, and O. Lenz. Impact of the iron-sulfur cluster proximal to the active site on the catalytic function of an O_2-tolerant NAD^+-reducing NiFe-hydrogenase. *Biochemistry*, **54**: 389-403, 2015.